

Phenomenology of the Higgs and Flavour Physics In the Standard Model and Beyond

DISSERTATION

zur Erlangung des akademischen Grades

doctor rerum naturalium
(Dr. rer. nat.)
im Fach Physik

eingereicht an der
Mathematisch-Wissenschaftlichen Fakultät
Humboldt-Universität zu Berlin

von

M.Sc. Lina Alasfar
geboren am 27.09. 1994 in Riad

Präsidentin der Humboldt-Universität zu Berlin:
Prof. Dr.-Ing. Dr. Sabine Kunst

Dekan der Mathematisch-Wissenschaftlichen Fakultät:
Prof. Dr. Elmar Kulke

Gutachter:

1. Prof. Dr. R. Gröber, Humboldt-Universität zu Berlin
2. Prof. Dr. Dr. M. Musterman, Potsdam-Institut für Klimafolgenforschung
3. Prof. Dr. M. Mustermann², Heidelberg

Tag der mündlichen Prüfung: 06. November 2013

Contents

I	Higgs Physics	1
1	The Standard Model Higgs boson	3
1.1	Spontaneous symmetry breaking	3
1.1.1	Nambu-Goldstone theorem	6
1.2	The Higgs mechanism	7
1.3	Yukawa interaction	10
1.4	The Higgs and EW precision observables	10
1.4.1	Custodial symmetry	12
2	Constraints on the Higgs properties	17
2.1	Theoretical constraints	17
2.1.1	Partial-wave unitarity	17
2.2	Experimental	20
3	Higgs and effective field theories	23
II	Single Higgs Processes at the LHC	25
4	Overview of Higgs production at colliders	27
5	Four top operator in Higgs production and decay	29
5.1	Introduction	29
5.2	Notation	31
5.3	Contribution of four-fermion operators to Higgs production and decay . .	32
5.3.1	Higgs coupling to gluons and photons	32
5.3.2	Higgs decay to bottom quarks	37
5.3.3	Associated production of a Higgs boson with top quarks	38
5.3.4	Results	40
5.4	Fit to Higgs observables	43
5.4.1	Fit methodology	43
5.4.2	Fit to LHC Run-II data	45
5.4.3	Prospects for HL-LHC	50
5.5	Summary and discussion	51

5.6	Two parameter fits	54
6	Virtual two-loop calculation of Zh production via gluon fusion	57
6.1	General notation	59
6.1.1	The transverse momentum expansion	61
6.2	Born cross-section in the p_T -expansion	62
6.3	NLO calculation	64
6.3.1	Renormalisation	65
6.3.2	Calculation of the exact virtual corrections	68
6.3.3	Calculation of the p_T -expanded virtual corrections	70
6.4	Results and conclusions	70
III	Higgs Pair at Hadron Colliders	75
7	Overview of Higgs pair production at colliders	77
8	Higgs pair as a probe for light Yukawas	81
9	Optimised search for Higgs pair via Interpretable machine learning	83
9.1	Overview of Light Yukawa searches	83
A	Details of Zh calculation	87
A.1	Orthogonal Projectors in $gg \rightarrow ZH$	87
A.2	Two-loop Results	88

Part I

Higgs Physics

1 The Standard Model Higgs boson

It's very nice to be right sometimes...
it has certainly been a long wait.

Peter Higgs

1.1 Spontaneous symmetry breaking

Before talking about symmetry breaking, we need to discuss the concept of symmetry in physics. Symmetry has an essential role in studying physical systems. It manifests not only as a geometric feature of physical objects but also in the dynamics of physical systems. For example, one can find symmetries in the equation of motion, Lagrangians/Hamiltonians and actions. The magnetisation of materials is a good example of the role that symmetry plays in describing physical behaviour. For instance, **paramagnetic** materials have a positive magnetic susceptibility χ_B due to the random arrangement of their electrons' spins. The paramagnetic material spins arrangement will therefore possess rotational symmetry. The material has no *preferred direction* in space [1]. On the contrary, **ferromagnetic** materials with the electrons' spins aligned in a certain direction, will not have such symmetry as there will be a preferred direction, see Figure 1.1.

In particle physics and quantum field theory, symmetry plays an essential role in the taxonomy and dynamics of elementary particles and their bound states, i.e. hadrons, cf. [2, 3]. There are two types of symmetries considered when studying elementary particles and their quantum fields: external and internal symmetries. The first is the symmetry of the spacetime background. Typically, this is a four-dimensional Poincaré symmetry. However, in some models, higher spacetime dimensions or non-flat geometries are considered. Though there is no current evidence of higher dimensions or indications of non-flat spacetime from colliders and cosmological observations [4]. The second class of symmetries is internal symmetries stemming from the quantum nature of these particles/fields. Because their state is described by a **ray** in complex Hilbert/Fock spaces, internal symmetries are simply symmetries of rotations in these spaces that keep the action variation unchanged. Internal symmetries are usually described in terms of simple or product of simple **Lie groups**, e.g. $SU(N)$ ¹, and particles/fields will be arranged

¹Gauge theories based on finite groups have been investigated in the literature, but their phenomeno-

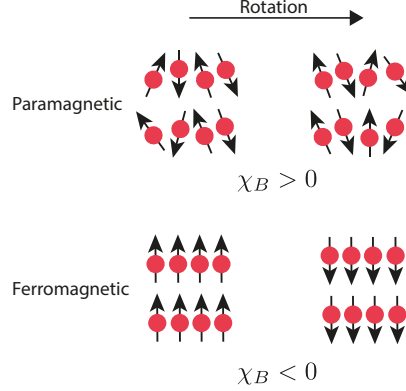


Figure 1.1. In paramagnetic materials, the spins are randomly distributed such that a rotation performed on the system will keep the spin distribution invariant. However, for ferromagnetic materials, where the spins are aligned in a single direction, the symmetry is broken, and the system has a preferred direction.

as multiplets in some representation of the groups. The rotations of the states could be parametrised by constants. In this case, the symmetry is called **global**, or fields of spacetime, where the symmetry is then called **local** or **gauged**.

Gauge symmetries describe rotations in the state space that depend on spacetime, the generator of the gauge transformations could propagate between two spacetime points. This is the way particle/field interactions are described in quantum field theory. The generators of these gauge transformations are called gauge bosons, and they mediate the interactions between the particles/fields and transform under the adjoint representation of the gauge group. Hence, we observe that gauge symmetries are the basis of describing the fundamental interactions of nature, which we call **gauge theories**.

An example of a gauge theory that is realised in nature is the **Standard Model** (SM). Which is a gauge theory based on the group $G_{\text{SM}} := SU(3)_C \otimes SU(2)_L \otimes U(1)_Y$. The first simple group is for the *strong* interaction described by quantum chromodynamics (QCD). The product of the two remaining groups $SU(2)_L \otimes U(1)_Y$ forms the Weinberg-Salam *electroweak* (EW) model [7–9], where $SU(2)_L$ describes the weak interaction which only couples to *left handed* fermions and $U(1)_Y$ is the weak hypercharge Y gauge group, defined by the formula

$$Y = 2(Q - T_3). \quad (1.1)$$

Where Q is the electric charge and T_3 is the third component of the weak isospin. A description of the matter content of the SM and their multiplicities with respect to G_{SM} is shown in Table 1.1

The SM has been very successful at describing particle interactions even when chal-

logical significance is yet to be further investigated [5, 6]

Particle/Field	G_{SM} multiplicity	mass [GeV]
Quarks		
$Q = \begin{pmatrix} u_L \\ d_L \end{pmatrix}, \begin{pmatrix} c_L \\ s_L \end{pmatrix}, \begin{pmatrix} t_L \\ b_L \end{pmatrix}$	$(\mathbf{3}, \mathbf{2}, 1/6)$	$m_u = 2.16 \cdot 10^{-3}, m_d = 2.67 \cdot 10^{-3}$
$U = u_R, s_R, t_R$	$(\mathbf{3}, \mathbf{1}, 2/3)$	$m_c = 0.93 \cdot 10^{-2}, m_s = 1.27$
$D = d_R, s_R, b_R$	$(\mathbf{3}, \mathbf{1}, -1/3)$	$m_t = 172.4, m_b = 4.18$
Leptons		
$L = \begin{pmatrix} \nu_{e,L} \\ e_L \end{pmatrix}, \begin{pmatrix} \nu_{\mu,L} \\ \mu_L \end{pmatrix}, \begin{pmatrix} \nu_{\tau,L} \\ \tau_L \end{pmatrix}$	$(\mathbf{1}, \mathbf{2}, -1/2)$	$m_e = 0.511 \cdot 10^{-3}, m_\mu = 1.05 \cdot 10^{-2}$
$E = e_R, \mu_R, \tau_R$	$(\mathbf{1}, \mathbf{1}, -1)$	$m_\tau = 1.77, m_\nu = ??$
Gauge bosons		
$g/G_\mu^A, A = 1 \dots 8$	$(\mathbf{8}, \mathbf{1}, 0)$	0.0
γ/A_μ	$(\mathbf{1}, \mathbf{1}, 0)$	0.0
W_μ^\pm	$(\mathbf{1}, \mathbf{3}, 0)$	80.379
Z_μ	$(\mathbf{1}, \mathbf{3}, 0)$	91.1876
The Higgs boson		
h	$(\mathbf{1}, \mathbf{2}, 1/2)$	125.10

Table 1.1. The SM constituents, their multiplicities with respect to the SM gauge group $G_{\text{SM}} := SU(3)_C \otimes SU(2)_L \otimes U(1)_Y$ and masses. The mass of the neutrinos ν is zero according to the SM prediction, but observations suggest that they are massive, and only the difference between the three masses is known [10]. The values of the masses are taken from the Particle Data Group (PDG) [4], and used throughout this thesis.

lenged by numerous precision tests at LEP and SLD [11–14] and later at DØ [15] and the LHC [16, 17]. Nevertheless, it fails to describe the ground state if only the fermion and gauge sectors are considered. The reason for this shortcoming is that the W^\pm and Z bosons have a mass, this violates the EW gauge symmetry. This can be easily seen by looking at the mass term of a spin 1 field B_μ^A

$$\mathcal{L} = m_B B^{A,\mu} B_\mu^A, \quad (1.2)$$

and performing an $SU(N)$ gauge transformation

$$B_\mu^A \rightarrow B_\mu^A + \partial_\mu \Lambda^A + g \varepsilon_{BC}^A B_\mu^B \Lambda^C. \quad (1.3)$$

We see that the mass term is invariant under these transformations. Secondly, because the SM is a chiral theory, as only left-handed fermions would be doublets under $SU(2)_L$, the Dirac mass term

$$\mathcal{L}_D = m_D \bar{\psi}_L \psi_R + \text{h.c.}, \quad (1.4)$$

cannot be a singlet under $SU(2)_L$, hence also violating the EW symmetry. Despite quark and lepton masses being forbidden by the EW symmetry, we indeed observe that they do have a mass, and since they also carry charges this mass has to be a Dirac mass.

In order for the EW model to be consistent at the ground state like it is in the interaction states. A mechanism for spontaneous symmetry breaking going from an interaction state to the vacuum ought to be introduced.

1.1.1 Nambu-Goldstone theorem

Coming back to the example of the paramagnetic-ferromagnetic materials, when heated above a certain temperature, known as the **Curie Temperature** T_C will undergo a phase transition and become paramagnetic (losing their permanent magnet property), in the mean-field theory approximation the magnetic susceptibility is related to the temperature of the metal via the relation

$$\chi_B \sim (T - T_C)^{-\gamma}, \quad (1.5)$$

where γ is a critical exponent. We see that if the metal temperature $T > T_C$ the metal is in an *disordered phase* and when $T < T_C$ it is in the *ordered phase*, i.e. χ_B is the **order parameter** of this system. At the Curie temperature, the system will be at the *critical point* where the susceptibility is divergent. The exponent γ is not used to describe the system at the critical point. There is a “pictorial” description of the metal at the critical point which is helpful in picturing the Goldstone theorem. Starting at $T > T_C$, the metal would be in a paramagnetic phase, where the spins are randomly arranged. As the temperature becomes lower and lower, thermal fluctuations start to lessen. One or

more regions of the metal, some of the spins will start to get aligned. With continued cooling, nearing T_C , these turned spins will affect their neighbours turning them into their directions. At the critical point $T = T_C$, the system behaves in a peculiar manner, when one would see regions of spins in “up” and others in “down” directions. The system will resemble a fractal of these regions, becoming scale-invariant. Additionally, waves of oscillating local magnetisation will propagate. These waves, or spinless quasiparticles (called **Magnons**) are Goldstone bosons emerging from spontaneous symmetry breaking. Which will manifest at $T < T_C$ as the spins will be arranged in a certain single direction and the metal becomes ferromagnetic.

Theorem 1 (Nambu-Goldstone). When a continuous symmetry has a conserved currents but broken in the ground state (vacuum) is called to be spontaneously broken. There is a scalar boson associated with each broken generator of this spontaneously broken symmetry. The modes of these bosons are fluctuations of the order parameter.

This theorem first emerged from condensed matter physics, particularly superconductors [18, 19]. However, it soon got applied to relativistic quantum field theories [20].

1.2 The Higgs mechanism

In order to solve the aforementioned shortcomings of the Weinberg-Salam model, Nambu-Goldstone theorem has been first proposed by P. W. Anderson [21]. However, the way that Anderson formulated his theory was unfamiliar to particle physicists and used a non-relativistic picture to illustrate how photons could gain mass in an electron plasma with a plasma frequency ω_p

$$m_\gamma^{\text{plasma}} = \frac{\hbar\omega_p}{c^2} \quad (1.6)$$

Later on, a theory that explains the mass generation of the EW gauge bosons has been published in an almost simultaneous manner by R. Braut and F. Englert [22], P. Higgs [23] and G. Guralnik, C. R. Hagen, and T. Kibble [24, 25]². The Higgs mechanism starts by considering the spontaneous symmetry breaking (SSB) of the EW sector of the SM via the pattern

$$SU(2)_L \otimes U(1)_Y \longrightarrow U(1)_Q \quad (1.7)$$

This is achieved by the vacuum expectation value (vev) of a complex scalar field $\phi \sim (\mathbf{1}, \mathbf{2}, +1/2)$, with the Lagrangian

$$\mathcal{L} = D_\mu \phi^* D^\mu \phi - V, \quad V := \mu^2 \phi^* \phi + \lambda(\phi^* \phi)^2, \quad (1.8)$$

²All of these authors have contributed to the theory of SM spontaneous symmetry breaking (SSB). By calling it the “Higgs” mechanism or boson. I, by no means, have intended to ignore the role played by the rest, rather, I wanted to stick the most widely-used terminology in the field.

where ϕ is given explicitly by

$$\phi = \begin{pmatrix} \phi^1 + i\phi^2 \\ \frac{1}{\sqrt{2}}(h + v) - i\phi^3 \end{pmatrix} \quad (1.9)$$

The covariant derivative

$$D_\mu = \partial_\mu - ig_2 \frac{\sigma_a}{2} W_\mu^a - ig_1 \frac{1}{2} B_\mu, \quad (1.10)$$

dictates the coupling between the Higgs field and the EW gauge bosons and g_3 , g_2 and g_1 are, respectively, the coupling constants of $SU(3)_C$, $SU(2)_L$ and $U(1)_Y$. The minimum of the scalar potential is then obtained by

$$\frac{\partial V}{\partial \phi} \big|_{\phi \rightarrow v} = 0, \quad (1.11)$$

which for a tachyonic mass $\mu^2 < 0$ will have a real non-vanishing values v corresponding to the vev of this field $\langle \phi \rangle = (\frac{v}{\sqrt{2}})$.

According to Nambu-Goldstone theorem, the three broken generators of $SU(2)_L \otimes U(1)_Y$ will become massive, and they are the W^\pm and Z bosons, while the photon will remain massless. We will have three massless Goldstone bosons $G^\pm = \frac{1}{2}(\phi^1 \pm i\phi^2)$ and $G^0 = \phi^3$ that are “eaten” by the aforementioned massive photons. Where they become the longitudinal polarisations of W^\pm and Z boson. In order to see this more concretely, we start by looking at the terms of the EW Lagrangian where the field ϕ couples to the gauge bosons, in the unbroken phase

$$D_\mu \phi^* D^\mu \phi = \frac{1}{2} |\partial_\mu \phi|^2 + \frac{1}{8} g_2^2 |\phi|^2 |W_\mu^1 + iW_\mu^2|^2 + \frac{1}{8} |\phi|^2 |g_2 W_\mu^3 - g_1 B_\mu|^2 \quad (1.12)$$

After SSB, we write the gauge bosons in the mass basis

$$\begin{aligned} W_\mu^\pm &= \frac{1}{\sqrt{2}} (W_\mu^1 \pm iW_\mu^2), \\ Z_\mu &= \frac{1}{\sqrt{g_1^2 + g_2^2}} (g_2 W_\mu^3 - g_1 B_\mu), \\ A_\mu &= \frac{1}{\sqrt{g_1^2 + g_2^2}} (g_2 W_\mu^3 + g_1 B_\mu). \end{aligned} \quad (1.13)$$

From this, the electric charge is identified as the coupling constant to the photon A_μ

$$e = \frac{g_1}{\sqrt{g_1^2 + g_2^2}}. \quad (1.14)$$

It is useful to define **Weinberg angle** θ_W , an important EW parameter relating the electric charge to the weak coupling g_2

$$\sin \theta_W = \frac{e}{g_2} \approx 0.231214, \quad (1.15)$$

typically the sin and cos of the Weinberg angle are denoted by s_W and c_W , respectively. We use the unitary gauge, to absorb the Goldstone bosons into the W^\pm and Z longitudinal polarisations. In this gauge the Higgs doublet can be written as

$$\phi \rightarrow \begin{pmatrix} 0 \\ \frac{1}{\sqrt{2}}(h + v) \end{pmatrix}, \quad v = 246 \text{ GeV}. \quad (1.16)$$

With these substitutions, one can read off the masses of the gauge bosons their bilinear terms in (1.12)

$$m_W = \frac{vg_2}{2} \quad m_Z = \frac{v}{2}\sqrt{g_1^2 + g_2^2} \quad m_A = 0. \quad (1.17)$$

Since ϕ is a complex doublet. We have seen that it has four components, and three of them correspond to the Goldstone bosons, thus one remains physical h which is what we now identify with the ‘‘Higgs boson’’ discovered in the Summer of 2012 [26, 27]. The couplings between the Higgs and the electroweak bosons is related to their mass via the vev

$$g_{hVV} = \frac{2m_V^2}{v}, \quad g_{hhVV} = \frac{2m_V^2}{v^2}. \quad (1.18)$$

By substituting (1.16), into the Higgs potential (1.8) one can write the mass of the physical Higgs boson in terms of the vev

$$m_h = \sqrt{2\lambda}v. \quad (1.19)$$

The physical Higgs mass is related to the μ parameter via the relation

$$m_h^2 = -2\mu^2, \quad (1.20)$$

One can see that the mass term after SSB changes its sign, characterising the order-parameter for this system, analogous to the magnetic susceptibility for the magnetisation of materials example. One could also identify the self-couplings of h , the trilinear and quartic couplings

$$g_{hhh} = 3\lambda v = 3\frac{m_h^2}{v}, \quad g_{hhhh} = 3\lambda = 3\frac{m_h^2}{v^2}. \quad (1.21)$$

1.3 Yukawa interaction

It is possible to also use the Higgs vev to give fermions their masses by introducing a Yukawa-interaction terms, first introduced by S. Weinberg [9]

$$\mathcal{L}_{\text{Yuk}} = -y_e \bar{L} \phi E - y_d \bar{Q} \phi D - y_u \bar{Q} \tilde{\phi} U + \text{h.c.}, \quad (1.22)$$

with $\tilde{\phi} = i\sigma_2 \phi$ and y_e, y_d, y_u are 3×3 matrices. These matrices are free parameters in the SM. As the Higgs boson acquires a the vev, the fermions will acquire a mass $m_f = v y'_f$ and the Higgs boson coupling to the fermions is given by

$$g_{h\bar{f}f} = \frac{m_f}{v}, \quad (1.23)$$

and the Yukawa matrices will be fixed in the mass basis y'_f by measurements of the fermion masses.

Leptonic Yukawa matrix is diagonal, with a degeneracy between the flavour and masses basis, this manifests as lepton family number conservation (the lepton family operator commutes with the Hamiltonian.). However, for the quarks, the situation is more complicated. One can rotate these matrices to the mass basis via a bi-unitary transformation via the unitary matrices $\mathcal{V}_Q, \mathcal{U}_Q$ for $q = u, d$

$$y_q \longrightarrow y'_f = \mathcal{V}_q^\dagger y_q \mathcal{U}_q = \text{diag}(m_{q_1}, m_{q_2}, m_{q_3}). \quad (1.24)$$

However, there is no degeneracy here as the Hamiltonian does not commute with the quark flavour operator. This is because the transformation matrices for the up and down-type quarks are not the same. The charged EW quark currents contains flavour mixing described by the Cabibbo-Kobayashi-Maskawa (CKM) matrix [28, 29]. More details on the flavour sector of the SM is discussed in [Update the section](#)

[Figure 1.2](#) shows all the SM couplings' strengths, with the thickness of the chord is proportional to the strength of the coupling, one can see the Higgs couplings in orange.

1.4 The Higgs and EW precision observables

Higgs physics is intertwined with the EW sector for example, the Higgs vev is determined from Fermi's constant $v = (\sqrt{2}G_F)^{-1/2}$, and is fixed by muon lifetime measurements, and comparing it with the theoretical predictions [30–33]

$$\tau_\mu^{-1} = \frac{G_F^2 m_\mu^5}{192\pi^3} \left(1 - \frac{8m_e^2}{m_\mu^2}\right) \left[1 - 1.810 \frac{\alpha}{\pi} + (6.701 \pm 0.002) \left(\frac{\alpha}{\pi}\right)^2\right], \quad (1.25)$$

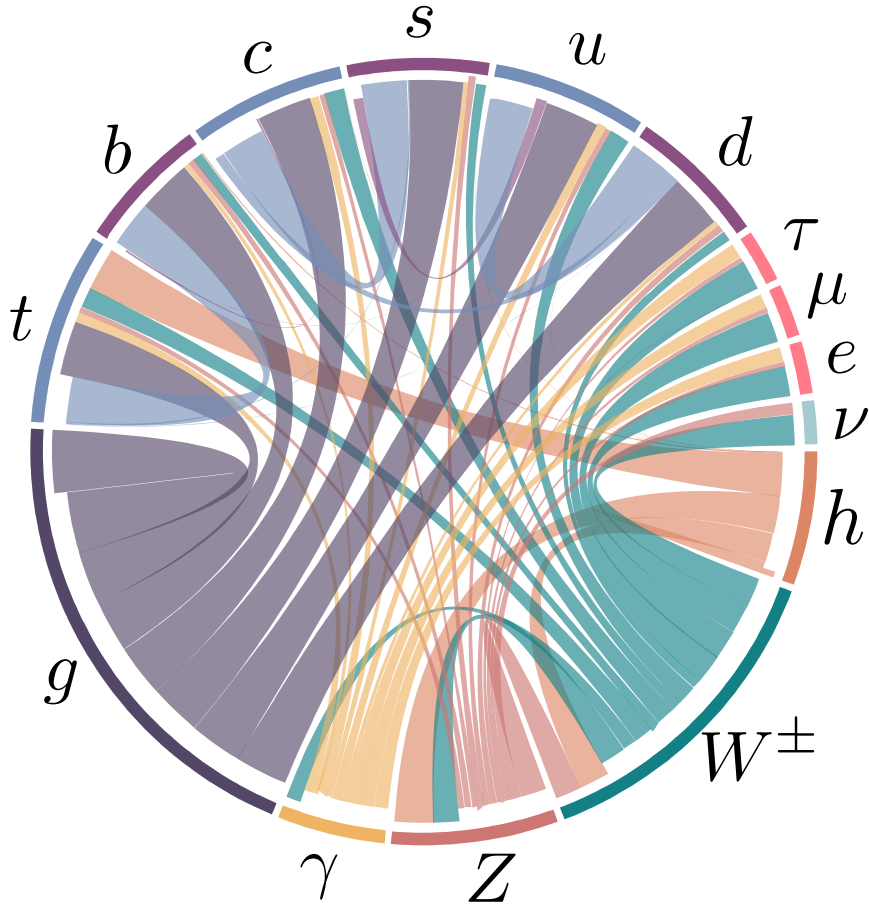


Figure 1.2. A chord diagram showing the SM couplings, with the coupling strength illustrated by the chord thickness. Higgs couplings are coloured in orange.

which leads to the numerical value of G_F [4]

$$G_F = 1.1663787(6) \cdot 10^{-5} \text{GeV}^{-2}, \quad (1.26)$$

given the value of the fine structure constant $\alpha^{-1} = 137.03599976(50)$.

Another important EW precision observable (EWPO) is the ratio between the W and Z masses

$$\rho = \frac{m_W^2}{c_W^2 m_Z^2}. \quad (1.27)$$

At leading order, this parameter is equal to unity in the SM. The ρ parameter depends on the representation of the scalar sector of the EW model having ϕ_i scalars with T_i weak isospin and $T_{3,i}$ being its third component, and a vev v_i , via the relation [34, 35]

$$\rho = \frac{\sum_i [T_i(T_i + 1) - T_{3,i}^2] v_i^2}{2 \sum_i T_{3,i}^2 v_i^2}. \quad (1.28)$$

From (1.28) one can see that a real triplet scalar, for instance, would not fit the experimental EW measurement of ρ . Hence, a complex doublet is the simplest scalar possible for the EW symmetry breaking, and the Higgs boson was expected to be seen almost four decades before its discovery. However, radiative corrections to the EW gauge bosons mass from vacuum polarisation diagrams could potentially cause ρ to deviate significantly from unity. This is not the case, as the experimentally measured value of ρ [4]

$$\rho_{\text{exp}} = 1.00038 \pm 0.00020 \quad (1.29)$$

Additionally, it is possible to think of an extended Higgs sector, where there are multiple scalars with different $SU(2)_L$ multiplicities. Or, a composite Higgs sector, where the Higgs boson is a pseudo Nambu-Goldstone boson, cf. [36, 37]. How can such models be built assuring the ρ parameter is protected from change? The answer to this question lies in a symmetry of the Higgs Lagrangian known as custodial symmetry.

1.4.1 Custodial symmetry

After SSB, a residual global symmetry known as the custodial symmetry protects the ρ parameter from obtaining large radiative corrections at higher orders in perturbation theory. This symmetry must be kept in extended or composite Higgs models. This symmetry can be seen by rewriting the Higgs potential as

$$V = \frac{\lambda}{4} \left(\phi_1^2 + \phi_2^2 + \phi_3^2 + \phi_4^2 - 2\mu^2 \right)^2. \quad (1.30)$$

This potential is invariant under $SO(4) \simeq SU(2)_L \otimes SU(2)_R$ rotations. However, when the Higgs field squires a non-vanishing vev, $\phi_4 \rightarrow h + v$, the potential becomes

$$V = \frac{\lambda}{4} \left(\phi_1^2 + \phi_2^2 + \phi_3^2 + h^2 + 2vh + v^2 - 2\mu^2 \right)^2, \quad (1.31)$$

which is only invariant under $SO(3) \simeq SU(2)_V$ transformations, the diagonal part of the original group. This global SSB pattern comes alongside the EW SSB of the gauge group $SU(2)_L \otimes U(1)_Y$ as global $SU(2)_L$ is itself the gauged $SU(2)_L$ group. Additionally the T^3 component of the $SU(2)_R$ global group is the gauged $U(1)_Y$ and the T^3 component of the custodial group $SU(2)_V$ is gauged as well and identified to be the electric charge operator, i.e. the generator of $U(1)_Q$.

$$\underbrace{SU(2)_R}_{\supset U(1)_Y} \otimes \overbrace{SU(2)_L}^{\text{gauged}} \longrightarrow \underbrace{SU(2)_V}_{\supset U(1)_Q}. \quad (1.32)$$

This pattern indicates that the symmetry is already broken by the gauging of the diagonal part of $SU(2)_R$ (the hypercharge). The custodial symmetry is only *approximate* in the limit of $g_1 \rightarrow 0$, and $\rho = 1$ is a consequence of $g_1 \neq 0$. The symmetry breaking pattern $\mathbf{2} \otimes \mathbf{2} = \mathbf{3} \oplus \mathbf{1}$ also allows us to identify the Goldstone bosons as the custodial triplet and the physical Higgs h as the custodial singlet, explaining the electric charge pattern they have.

We could use the isomorphism between the special orthogonal and special unitary groups to parametrise the Higgs doublet as an $SU(2)_L \otimes SU(2)_R$ bidoublet

$$\mathcal{H} = \begin{pmatrix} \tilde{\phi} & \phi \end{pmatrix} = \frac{1}{\sqrt{2}} \begin{pmatrix} \phi_4 - i\phi_3 & \phi_1 + i\phi_2 \\ \phi_1 - i\phi_2 & \phi_4 + i\phi_3 \end{pmatrix}, \quad (1.33)$$

with the bi-unitary transformations

$$\mathcal{H} \longrightarrow \mathcal{U}_L \mathcal{H} \mathcal{U}_R^\dagger \quad (1.34)$$

which leaves any traces of the form $\text{Tr}(\mathcal{H}^\dagger \mathcal{H})$, invariant. The Higgs potential could be rewritten in terms of the bidoublet

$$V = -\frac{\mu^2}{2} \text{Tr}(\mathcal{H}^\dagger \mathcal{H}) + \frac{\lambda}{4} \left(\text{Tr}(\mathcal{H}^\dagger \mathcal{H}) \right)^2 \quad (1.35)$$

The vev is hence written in this representation as

$$\langle \mathcal{H} \rangle = \frac{v}{\sqrt{2}} \mathbb{1}_{2 \times 2}. \quad (1.36)$$

We can also look at the Yukawa sector, and observe that in the case where $y_u = y_d = y$, we can also write the left-handed and right-handed quarks as $SU(2)_L \otimes SU(2)_R$ bidoublets and $SU(2)_R$ doublets, respectively. Hence, the quark part of the Yukawa Lagrangian in (1.22) becomes

$$\mathcal{L}_{yuk} \supset \frac{y}{\sqrt{2}} (\bar{u}_L \ \bar{d}_L) \begin{pmatrix} \phi_4 - i\phi_3 & \phi_1 + i\phi_2 \\ \phi_1 - i\phi_2 & \phi_4 + i\phi_3 \end{pmatrix} \begin{pmatrix} u_R \\ d_R \end{pmatrix}, \quad (1.37)$$

which is invariant under custodial transformations, but when $y_u \neq y_d$, this Lagrangian term breaks custodial symmetry. Thus, the differences between the up-type and down-type quark masses $m_u - m_d$ are considered **spurions** of the custodial symmetry and one expects to see radiative corrections to ρ being proportional to these spurions.

In order to see this more concretely, we start by examining the radiative corrections that could contribute to the deviation of ρ from unity, i.e. $\Delta\rho$ these corrections are known as the **oblique correction**. These oblique corrections come from electroweak vacuum polarisations $\Pi_{VV}(p^2)$, as shown in Figure 1.3, for more details on these corrections and their calculation see Refs.. [38, 39]

The 1-loop correction to the ρ parameter is given in terms of the Π_{VV} by

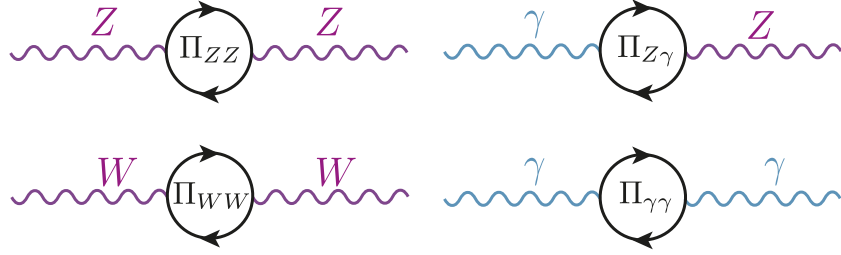


Figure 1.3. The oblique corrections, are radiative correction with electroweak gauge bosons propagators. Namely vacuum polarisations of the Z , W^\pm and γ bosons.

$$\Delta\rho = \frac{\Pi_{WW}(0)}{m_W^2} - \frac{\Pi_{ZZ}(0)}{m_Z^2} \quad (1.38)$$

Where the dominant contributions are given by [40]

$$\Delta\rho = \frac{3G_F}{8\sqrt{2}\pi^2} \left((m_t^2 + m_b^2) - \frac{2m_t^2 m_b^2}{m_t^2 - m_b^2} \ln \frac{m_t^2}{m_b^2} \right) + \dots \quad (1.39)$$

Since $m_b \ll m_t$, the correction is non-vanishing, and (1.39) shows clearly how the radiative corrections are proportional to the spurions of the custodial symmetry. However, this radiative correction is absorbed into the SM definition of ρ , i.e. the $\overline{\text{MS}}$ definition of the ρ -parameter $\rho^{\overline{\text{MS}}}$.

One can study new physics (NP) effects that violates custodial symmetry, by looking at deviations from $\rho = 1$ from it. Given the experimentally measured value of ρ (1.29) many NP models violating custodial symmetry can already be excluded. Nevertheless, ρ alone does not capture the full story of EWPO's. For instance, adding a new quark doublet would not necessarily violate the custodial symmetry though it still can be excluded by EWPO. It is hence useful to introduce new parameters known as **Peskin-Takeuchi parameters** [39, 41, 42]

$$\begin{aligned} S &:= \frac{4c_W^2 s_W^2}{\alpha} \left[\frac{\Pi_{ZZ}^{\text{NP}}(m_Z^2) - \Pi_{ZZ}^{\text{NP}}(0)}{m_Z^2} - \frac{c_W^2 - s_W^2}{c_W s_W} \frac{\Pi_{Z\gamma}^{\text{NP}}(m_Z^2)}{m_Z^2} - \frac{\Pi_{\gamma\gamma}^{\text{NP}}(m_Z^2)}{m_Z^2} \right], \\ T &:= \frac{\rho^{\overline{\text{MS}}} - 1}{\alpha} = \frac{1}{\alpha} \left[\frac{\Pi_{WW}^{\text{NP}}(0)}{m_W^2} - \frac{\Pi_{ZZ}^{\text{NP}}(0)}{m_Z^2} \right], \\ U &:= \frac{4s_W^2}{\alpha} \left[\frac{\Pi_{WW}^{\text{NP}}(m_W^2) - \Pi_{WW}^{\text{NP}}(0)}{m_W^2} - \frac{c_W}{s_W} \frac{\Pi_{Z\gamma}^{\text{NP}}(m_Z^2)}{m_Z^2} - \frac{\Pi_{\gamma\gamma}^{\text{NP}}(m_Z^2)}{m_Z^2} \right] - S. \end{aligned} \quad (1.40)$$

The NP contributions to the EW vacuum polarisations $\Pi_{VV}^{\text{NP}}(p^2)$ could either come from loop or tree-level effects. Typically both T and U are related to custodial symmetry violation. However, U has an extra suppression factor of m_{NP}^2/m_Z^2 compared to T and S . The most recent fit result for these parameters is [4]

$$\begin{aligned} S &= -0.01 \pm 0.10, \\ T &= 0.03 \pm 0.13, \\ U &:= 0.02 \pm 0.11. \end{aligned} \quad (1.41)$$

But since T and S tend to give stronger constraint on NP, due to the suppression factor of U . One can preform a two-parameter fit of S and T setting $U = 0$, thas shown in Figure 1.4, with the numerical values [4],

$$\begin{aligned} S &= 0.00 \pm 0.07, \\ T &= 0.05 \pm 0.06. \end{aligned} \quad (1.42)$$

The Peskin-Takeuchi parameters are important in constraining effective operators in the Higgs sector , namely

$$\begin{aligned} \hat{O}_S &= \phi^\dagger \sigma_i \phi W_{\mu\nu}^i B^{\mu\nu}, \\ \hat{O}_T &= |\phi^\dagger D_\mu \phi|^2. \end{aligned} \quad (1.43)$$

For example, \hat{O}_S appears in Technicolour models causing large deviations of S compared

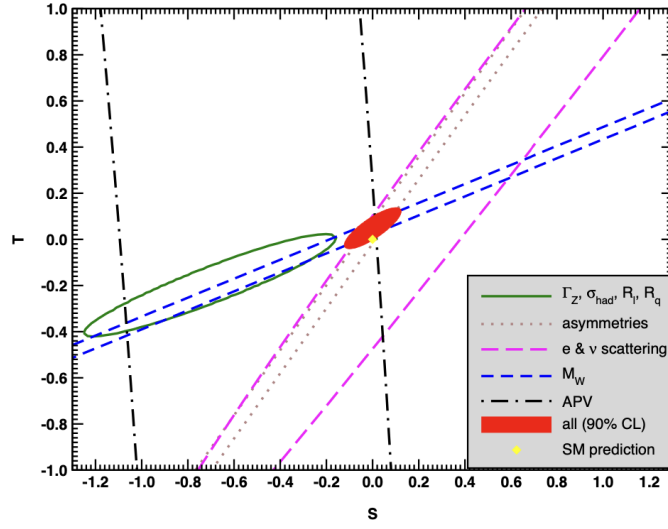


Figure 1.4. Fit results from various EWPO's for T and S setting $U =$. The contours show 1σ contours (39.35% for closed contours and 68% for the rest). This plot is obtained from the PDG [4]

to its measured value [41, 43–45]. Moreover, The constraints on T parameter is important for top mass generation as well as modifications to $Zb\bar{b}$ coupling in such models [46, 47]. We will revisit the \hat{O}_T when we discuss the Higgs and effective field theories in section [update here](#).

2 Constraints on the Higgs properties

In this chapter, the bounds on the Higgs sector will be discussed. Starting from an overview of the theoretical constraints on the Higgs potential, like the quantum triviality and unitarity. Then, the state-of-the-art experimental results on Higgs properties and couplings measurements will be discussed. However, despite many of the Higgs boson properties have been measured with good accuracy, there are still difficult observables in the Higgs sector and some open problems. These will be addressed at the end of this chapter.

2.1 Theoretical constraints

2.1.1 Partial-wave unitarity

Recall that in particle scattering process, the \mathbf{S} matrix is defined via the relation

$$|out\rangle = \mathbf{S} |in\rangle \quad (2.1)$$

Since the S-matrix S describes the transition probability, it must satisfy the unitarity condition

$$\mathbf{S}^\dagger \mathbf{S} = \mathbf{S} \mathbf{S}^\dagger = \mathbb{1}, \quad (2.2)$$

in order to have probability / quantum numbers conservation.

Moreover, we can remove the identity operator $\mathbf{1}$ by defining the operator T such as

$$\mathbf{S} = \mathbb{1} + i\mathbf{T}. \quad (2.3)$$

For small coupling, \mathbf{T} is small, enabling the use of perturbation theory. Now, we apply the unitarity condition to find a new relation for \mathbf{T}

$$\begin{aligned} \mathbf{S}^\dagger \mathbf{S} = \mathbb{1} &= (\mathbf{1} - i\mathbf{T}^\dagger)(\mathbf{1} + i\mathbf{T}) \\ &\Rightarrow -i\mathbf{T}^\dagger + i\mathbf{T} + \mathbf{T}^\dagger \mathbf{T} = 0 \\ &\Rightarrow \mathbf{T}^\dagger \mathbf{T} = \underbrace{-i(\mathbf{T} - \mathbf{T}^\dagger)}_{=2\Im(\mathbf{T})}. \end{aligned} \quad (2.4)$$

With the matrix element given by

$$\langle a | \mathbf{T} | b \rangle = \mathcal{M}_{ab}(2\pi)^4 \delta^4(p_a - p_b), \quad (2.5)$$

and using the completeness relations, we define the unity operator in terms of some states $|f\rangle$

$$\mathbb{1} = \sum_f \prod_i \int \frac{d^3 p'}{(8\pi^3) 2E_i^f} (2\pi)^4 |f\rangle \langle f|. \quad (2.6)$$

Thus, the matrix element should satisfy

$$\sum_f \prod_i \int \frac{d^3 p'}{(2\pi)^3 2E_i^f} (2\pi)^4 \delta^4(p_i - \sum_i p_i^f) \mathcal{M}_{bf} \mathcal{M}_{af}^* = -i(\mathcal{M}_{ba} - \mathcal{M}_{ab}^*). \quad (2.7)$$

. Here, f denotes any set of intermediate states between $|a\rangle$ and $|b\rangle$. For the elastic scattering case, where $a = b$, we arrive at the **Optical Theorem**¹

$$\sum_f \int d\Phi_n(p_a, p_i^f) |\mathcal{M}_{af}|^2 = 2\Im(\mathcal{M}_{aa}). \quad (2.8)$$

Where $d\Phi_n(p_a, p_i^f)$ is the n -particle phase space, for the $2 \rightarrow 2$ case, the equality is substituted by \leq .

From now on, we shall only consider the $2 \rightarrow 2$ case ($|p_1, p_2\rangle \rightarrow |k_1, k_2\rangle$) in which we could simplify the phase space further, rewriting the LHS of (2.8) as

$$\begin{aligned} & \int \frac{d^3 k_1}{(2\pi)^3 2E_1} \int \frac{d^3 k_2}{(2\pi)^3 2E_2} (2\pi)^4 \delta^4(p_1 + p_2 - k_1 - k_2) |\mathcal{M}(s, t)|^2, \\ &= \frac{1}{16\pi} \int_{-1}^1 d(\cos \theta) |\mathcal{M}(s, t)|^2. \end{aligned} \quad (2.9)$$

Recall that the relation between the Mandelstam variable t , and the scattering angle for the elastic scattering is given by

$$t = \frac{1}{2}(s - 4m^2)(\cos \theta - 1) \quad (2.10)$$

We could expand the matrix element $\mathcal{M}(s, t)$ in terms of *partial waves*, isolating s from scattering angle dependence

$$\mathcal{M}(s, t) = 16\pi \sum_j (2j+1) a_j P_j(\cos \theta). \quad (2.11)$$

Where a_j are called the j th partial wave amplitude, and $P_j(\cos \theta)$ are the Legendre

¹Note that \mathcal{M}_{af} is diagonalisable since T is normal as a result from the S-matrix unitarity.

polynomials

$$P_j(z) = \frac{1}{j!} \frac{1}{2j} \frac{d^j}{dz^j} (z^2 - 1)^j \quad (2.12)$$

Which satisfies the orthonormality condition

$$\int_{-1}^1 dz P_j(z) P_k(z) = \frac{1}{2j+1} \delta_{jk} \quad (2.13a)$$

$$P_j(1) = 1 \quad \forall j. \quad (2.13b)$$

We hence get for the LHS of (2.8) scattering

$$\begin{aligned} & \int \frac{d^3 k_1}{(2\pi)^3 2E_1} \int \frac{d^3 k_2}{(2\pi)^3 2E_2} (2\pi)^4 \delta^4(p_1 + p_2 - k_1 - k_2) |\mathcal{M}(s, t)|^2, \\ &= \frac{1}{16\pi} \int_{-1}^1 d(\cos \theta) \left[16\pi \sum_j (2j+1) a_j(s) P_j(\cos \theta) \right] \times \\ & \quad \left[16\pi \sum_k (2k+1) a_k^*(s) P_k(\cos \theta) \right], \\ & \Rightarrow = 32\pi \sum_j (2j+1) |a_j(s)|^2. \end{aligned} \quad (2.14)$$

And the RHS of (2.8)

$$2\mathfrak{I}(\mathcal{M}_{aa}) = \underbrace{2\mathfrak{I}(\mathcal{M}(s, 0))}_{t \text{ is integrated out.}} = 32\pi \sum_j (2j+1) \mathfrak{I}(a_j(s)). \quad (2.15)$$

Otherwise large cancellations needed, $a_j(s)$'s are hierarchal. Thus, we could compare the partial wave amplitudes term-by-term

$$|a_j(s)|^2 \leq \mathfrak{I}(a_j(s)) \quad \Rightarrow \quad \Re(a_j(s))^2 + \mathfrak{I}(a_j(s))^2 \leq \mathfrak{I}(a_j(s)) \quad (2.16)$$

Rearrainging terms, we get

$$\Re(a_j(s)) + \left(\mathfrak{I}(a_j(s)) - \frac{1}{2} \right)^2 \leq \frac{1}{4} \quad (2.17)$$

The partial wave amplitude has to lie within the unitarity circle, see figure ?? . We use though perturbation theory if the the partial wave amplitude respects the inequality

$$\Re(a_j(s)) \leq \frac{1}{2} \quad (2.18)$$

2.2 Experimental

We also provide in this appendix the experimental measurements of the signal strengths at the LHC Run II and the CMS projections for the HL-LHC (scenario S2, see [48]) that we used in the fits in this paper. These inputs are summarised in table 2.1.

Production	Decay	$\mu_{\text{Exp}} \pm \delta\mu_{\text{Exp}}$ (symmetrised)		Ref.
		LHC Run-II	HL-LHC	
		CMS 137 fb ⁻¹ ATLAS 139 fb ⁻¹	CMS 3 ab ⁻¹	
ggF	$h \rightarrow \gamma\gamma$	0.99 ± 0.12 1.030 ± 0.110	1.000 ± 0.042	[49–51]
	$h \rightarrow ZZ^*$	0.985 ± 0.115 0.945 ± 0.105	1.000 ± 0.040	
	$h \rightarrow WW^*$	1.285 ± 0.195 1.085 ± 0.185	1.000 ± 0.037	[49, 51, 52]
	$h \rightarrow \tau^+\tau^-$	0.385 ± 0.385 1.045 ± 0.575	1.000 ± 0.055	
	$h \rightarrow b\bar{b}$	2.54 ± 2.44 –	1.000 ± 0.247	[51, 52]
	$h \rightarrow \mu^+\mu^-$	0.315 ± 1.815 –	1.000 ± 0.138	[51, 52]
VBF	$h \rightarrow \gamma\gamma$	1.175 ± 0.335 1.325 ± 0.245	1.000 ± 0.128	[49–51]
	$h \rightarrow ZZ^*$	0.62 ± 0.41 1.295 ± 0.455	1.000 ± 0.134	
	$h \rightarrow WW^*$	0.65 ± 0.63 0.61 ± 0.35	1.000 ± 0.073	[49, 51, 52]
	$h \rightarrow \tau^+\tau^-$	1.055 ± 0.295 1.17 ± 0.55	1.000 ± 0.044	
	$h \rightarrow b\bar{b}$	– 3.055 ± 1.645	–	[49]
	$h \rightarrow \mu^+\mu^-$	3.325 ± 8.075 –	1.000 ± 0.540	[51]
$t\bar{t}h$	$h \rightarrow \gamma\gamma$	1.43 ± 0.30 0.915 ± 0.255	1.000 ± 0.094	[49–51]
	$h \rightarrow VV^*$	$0.64 \pm 0.64 (ZZ^*)$ $0.945 \pm 0.465 (WW^*)$ 1.735 ± 0.545	$1.000 \pm 0.246 (ZZ^*)$ $1.000 \pm 0.097 (WW^*)$ –	
	$h \rightarrow \tau^+\tau^-$	0.845 ± 0.705 1.27 ± 1.0	1.000 ± 0.149	[49, 51, 52]
	$h \rightarrow b\bar{b}$	1.145 ± 0.315 0.795 ± 0.595	1.000 ± 0.116	
Vh	$h \rightarrow \gamma\gamma$	0.725 ± 0.295 1.335 ± 0.315	$1.000 \pm 0.233 (Zh)$ $1.000 \pm 0.139 (W^\pm h)$	[49–51]
	$h \rightarrow ZZ^*$	1.21 ± 0.85 1.635 ± 1.025	$1.000 \pm 0.786 (Zh)$ $1.000 \pm 0.478 (W^\pm h)$	[49, 51, 52]
	$h \rightarrow WW^*$	1.850 ± 0.438 –	$1.000 \pm 0.184 (Zh)$ $1.000 \pm 0.138 (W^\pm h)$	[51, 53]
	$h \rightarrow b\bar{b}$	– 1.025 ± 0.175	$1.000 \pm 0.065 (Zh)$ $1.000 \pm 0.094 (W^\pm h)$	[49, 51]
Zh CMS	$h \rightarrow \tau^+\tau^-$	1.645 ± 1.485		
	$h \rightarrow b\bar{b}$	0.94 ± 0.32		
$W^\pm h$ CMS	$h \rightarrow \tau^+\tau^-$	3.08 ± 1.58	–	[52]
	$h \rightarrow b\bar{b}$	1.28 ± 0.41		

Table 2.1. The experimental single Higgs observables measurements from the LHC Run II and projections for the HL-LHC. In all cases we have symmetrised the experimental uncertainties that we use in the fits.

3 Higgs and effective field theories

Part II

Single Higgs Processes at the LHC

4 Overview of Higgs production at colliders

5 Four top operator in Higgs production and decay

5.1 Introduction

The precise determination of the Higgs boson properties is one of the main focus of the Large Hadron Collider (LHC) physics programme. Within the current experimental precision, the measurement of the Higgs couplings so far appear to be in agreement with the Standard Model (SM) prediction within an accuracy of, typically, ten percent [54, 55]. In many beyond the SM (BSM) scenarios, however, it is expected that new physics will introduce modifications in the Higgs properties. If the new BSM degrees of freedom are much heavier than the electroweak scale, a general description of potential new physics effects can be formulated in the language of an effective field theory (EFT). One possibility of such a parameterization is the so-called Standard Model EFT (SMEFT), in which new physics effects are given in terms of higher-dimensional operators involving only SM fields and that also respect the SM gauge symmetries. The dominant effects on Higgs physics, electroweak physics and top quark physics stem from dimension-six operators, suppressed by the new physics scale Λ . This approach is justified in the limit in which energy scales $E \ll \Lambda$ are probed.

In this paper we will consider a small subset of these operators, namely four-fermion operators of the third generation quarks. A direct measurement of the four-top quark operators requires the production of four top quarks. At the LHC, for $\sqrt{s} = 13$ TeV, and within the SM, this is a rather rare process, with a cross section of about 12 fb including NLO QCD and NLO electroweak (EW) corrections [56]. This is due to the large phase space required for the production of four on-shell top quarks. First experimental measurements [57] indicate a slightly higher cross section than the SM prediction.¹ Though four-top production gives direct access to four-top operators, the main effect comes from $\mathcal{O}(1/\Lambda^4)$ terms when computing the matrix element squared [59], questioning whether one should neglect, in general, the effects of dimension-eight operators in the calculation of the amplitudes. At any rate, current experimental bounds on the four-top operators are rather weak. A significant improvement in constraining power would be expected, however, at a future 100 TeV pp collider, due to the growth with the energy of the diagrams involving four-top operators [60]. The situation is rather similar for the operators

¹We note that a CMS combination from different LHC runs [58], though having lower signal significance, shows agreement with the SM prediction.

leading to $t\bar{t}b\bar{b}$ contact interactions. They can be measured directly in $t\bar{t}b\bar{b}$ production, see [61, 62] for experimental analyses at $\sqrt{s} = 13$ TeV, but also leading to rather weak limits in SMEFT fits [59, 63].

Given the rather weak “direct” bounds on the $t\bar{t}t\bar{t}$ and $t\bar{t}b\bar{b}$ contact interactions, here we will discuss alternative probes, showing how these interactions can be constrained indirectly via their contributions to single Higgs observables.² These operators generate contributions to the effective couplings of the Higgs to gluons and photons via two-loop diagrams. At the one-loop level, they also modify associated production of a Higgs boson with top quarks and, in the case of a $t\bar{t}b\bar{b}$ operator, also the Higgs decay to bottom quarks. While the leading log results can be easily included by renormalisation group operator mixing effects [66–68], in this paper we will compute also the finite terms and show that they can be numerically important.

In addition, we will study the interplay between the extraction of the Higgs self-coupling measurement from single Higgs production and decay and the four-fermion operators. It was previously proposed that competitive limits to the ones from Higgs pair production on the trilinear Higgs self-coupling can be set using single Higgs data [69–76]. A global fit including all operators entering in Higgs production and decay at tree-level plus the loop-modifications via the trilinear Higgs self-coupling has been performed in [77]. Searches for modifications of the trilinear Higgs self-coupling via single Higgs production have been presented by the ATLAS [78] and CMS [52] collaboration. Using the example of the four-quark operators, we will show that there are other weakly constrained dimension-six operators, that enter at the loop level, that should be included in such analyses as they have a non-trivial interplay with the trilinear Higgs self-coupling extraction from single Higgs measurements. We will hence perform a combined fit of these operators together with the operator modifying the trilinear Higgs self-coupling. While our study does not consider a global fit to all operators entering Higgs data, the results of our computations can be easily used in global analyses. Our main point, namely that in a global fit all operators entering via loop contributions, if so far constrained only weakly (as it is the case for, e.g., four-top operators), should be included, is clearly demonstrated by our few parameters fit.

The paper is structured as follows: in section 5.2 we clarify the notation used for the effective Lagrangian in our analysis. In section 5.3 we give the results of our computation of the loop contributions of the four-fermion operators. The results of a fit to data including the computed loop contributions are presented in section 5.4, where we show results for both current data and projections at the High-Luminosity LHC (HL-LHC). We conclude in section ???. Further details of our analysis and additional material derived from our results are presented in two appendices.

²Alternatively, other indirect probes of four-top quark interactions that have been proposed include top quark pair production [64] and electroweak precision data [65]. The latter mostly leads to bounds on operators that can be constrained only weakly from Higgs data.

5.2 Notation

In the presence of a gap between the electroweak scale and the scale of new physics, Λ , the effect of new particles below the new physics scale can be described by an EFT. In the case of the SMEFT, the SM Lagrangian is extended by a tower of higher-dimensional operators, \mathcal{O}_i , built using the SM symmetries and fields (with the Higgs field belonging to an $SU(2)_L$ doublet), and whose interaction strength is controlled by Wilson coefficients, C_i , suppressed by the corresponding inverse power of Λ . In a theory where baryon and lepton number are preserved, the leading order (LO) new physics effects are described by the dimension-six SMEFT Lagrangian,

$$\mathcal{L}_{\text{SMEFT}}^{d=6} = \mathcal{L}_{\text{SM}} + \frac{1}{\Lambda^2} \sum_i C_i \mathcal{O}_i. \quad (5.1)$$

A complete basis of independent dimension-six operators was presented for the first time in [79], the so-called *Warsaw basis*. In this work, we are interested in particular in the effect of four-fermion operators of the third generation. These are, in the basis of [79],

$$\begin{aligned} \Delta \mathcal{L}_{\text{SMEFT}}^{d=6} = & \frac{C_{tt}}{\Lambda^2} (\bar{t}_R \gamma_\mu t_R) (\bar{t}_R \gamma^\mu t_R) + \frac{C_{Qt}^{(1)}}{\Lambda^2} (\bar{Q}_L \gamma_\mu Q_L) (\bar{t}_R \gamma^\mu t_R) + \frac{C_{Qt}^{(8)}}{\Lambda^2} (\bar{Q}_L T^A \gamma_\mu Q_L) (\bar{t}_R T^A \gamma^\mu t_R) \\ & + \frac{C_{QQ}^{(1)}}{\Lambda^2} (\bar{Q}_L \gamma_\mu Q_L) (\bar{Q}_L \gamma^\mu Q_L) + \frac{C_{QQ}^{(3)}}{\Lambda^2} (\bar{Q}_L \sigma_a \gamma_\mu Q_L) (\bar{Q}_L \sigma_a \gamma^\mu Q_L) \\ & + \left[\frac{C_{QtQb}^{(1)}}{\Lambda^2} (\bar{Q}_L t_R) i \sigma_2 (\bar{Q}_L^T b_R) + \frac{C_{QtQb}^{(8)}}{\Lambda^2} (\bar{Q}_L T^A t_R) i \sigma_2 (\bar{Q}_L^T T^A b_R) + \text{h.c.} \right] \\ & + \frac{C_{bb}}{\Lambda^2} (\bar{b}_R \gamma_\mu b_R) (\bar{b}_R \gamma^\mu b_R) + \frac{C_{tb}^{(1)}}{\Lambda^2} (\bar{t}_R \gamma_\mu t_R) (\bar{b}_R \gamma^\mu b_R) + \frac{C_{tb}^{(8)}}{\Lambda^2} (\bar{t}_R T^A \gamma_\mu t_R) (\bar{b}_R T^A \gamma^\mu b_R) \\ & + \frac{C_{Qb}^{(1)}}{\Lambda^2} (\bar{Q}_L \gamma_\mu Q_L) (\bar{b}_R \gamma^\mu b_R) + \frac{C_{Qb}^{(8)}}{\Lambda^2} (\bar{Q}_L T^A \gamma_\mu Q_L) (\bar{b}_R T^A \gamma^\mu b_R), \end{aligned} \quad (5.2)$$

where we assume all Wilson coefficients to be real. In (5.2), Q_L , t_R and b_R refer to the third family quark left-handed doublet and right-handed singlets, respectively; σ_a are the Pauli matrices; T^A are the $SU(3)_c$ generators and T denotes transposition of the $SU(2)_L$ indices.

The largest effects in Higgs physics are typically expected to come from operators with the adequate chiral structure entering in top quark loops, as they will be proportional to the top quark mass/Yukawa coupling. Conversely, we expect a suppression of operators including bottom quarks with the bottom Yukawa coupling. As we will argue below, either because of their chirality or because they only enter in bottom loops, the operators with right-handed bottom quarks in the last two lines in (5.2) are expected to give only very small effects, and will be neglected. This is not the case for the operators

$\mathcal{O}_{QtQb}^{(1),(8)}$, which can have sizeable contributions to, e.g. Higgs to $b\bar{b}$ or gluon fusion rates, proportional to the top quark mass.

We will later on also compare with possible effects of a trilinear Higgs self-coupling modification with respect to the SM. In the dimension-six SMEFT, the only operator that modifies the Higgs self-interactions without affecting the single-Higgs couplings at tree level is

$$\Delta\mathcal{L}_{\text{SMEFT}}^{d=6} = \frac{C_\phi}{\Lambda^2}(\phi^\dagger\phi)^3, \quad (5.3)$$

where ϕ stands for the usual $SU(2)_L$ scalar doublet, with $\phi = 1/\sqrt{2}(0, v+h)^T$ in the unitary gauge. Furthermore, for later use we write down also the operators that modify the Higgs coupling to top and bottom quarks

$$\Delta\mathcal{L}_{\text{SMEFT}}^{d=6} = \left(\frac{C_{t\phi}}{\Lambda^2} \phi^\dagger \phi \bar{Q}_L \tilde{\phi} t_R + \frac{C_{b\phi}}{\Lambda^2} \phi^\dagger \phi \bar{Q}_L \phi b_R + \text{h.c.} \right), \quad (5.4)$$

with $\tilde{\phi} = i\sigma_2\phi^*$.

5.3 Contribution of four-fermion operators to Higgs production and decay

In this section, we discuss the contribution of the third generation four-fermion operators to various Higgs production mechanisms and Higgs decay channels.

5.3.1 Higgs coupling to gluons and photons

We start by discussing the calculation of the Higgs couplings to gluons and photons. The four-top-quark operators enter these couplings at the two-loop level. The diagrams are shown in Figure 5.1. There are three classes of diagrams: (a) corrections to the top-quark propagator, (b) corrections to the Higgs Yukawa coupling and (c) corrections to the $t\bar{t}g$ and $t\bar{t}\gamma$ vertices. The latter turns out to be zero when the gluons or photons are on-shell. The first and second type of corrections are left-right (LR) transitions hence the only contributions stem from the operators with Wilson coefficients $C_{Qt}^{(1),(8)}$ and $C_{QtQb}^{(1),(8)}$. As can be inferred from the diagrams in Figure 5.1 the result can be expressed as a product of one-loop integrals. We computed the diagrams in two independent calculations making use of different computer algebra tools such as **PackageX** [80], **KIRA** [81], **Fire** [82], **FeynRules** [83] and **FeynArts** [84].³ We cross-checked the Feynman rules with ref. [85].

³Note that the latter tool needed some manual adjustments to deal with four-fermion operators.

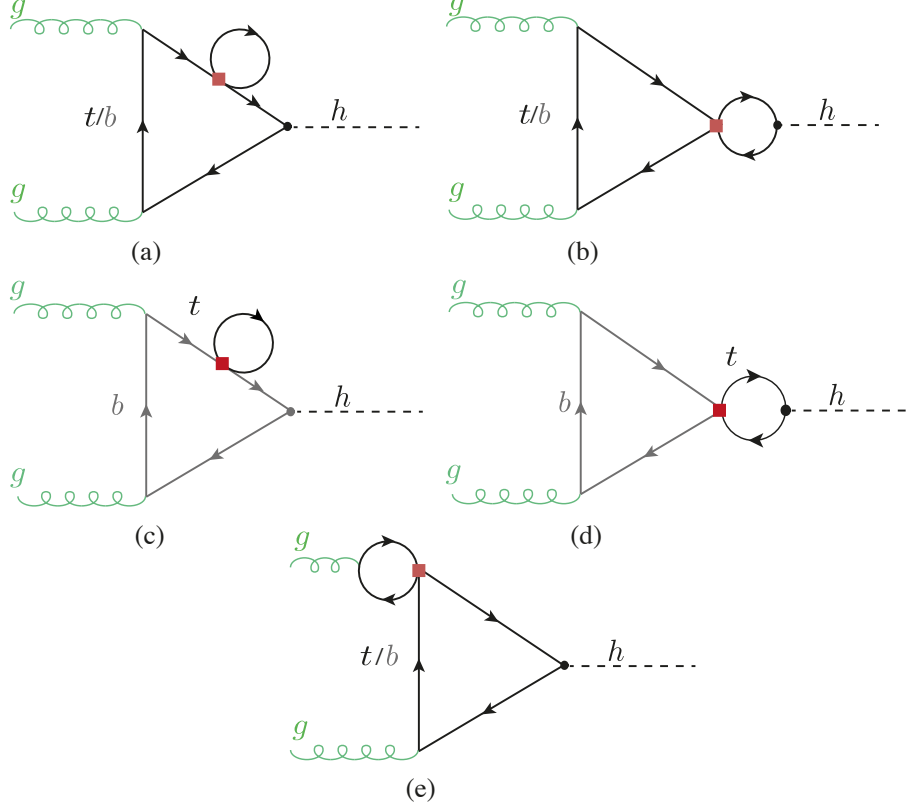


Figure 5.1. Example Feynman diagrams for four-fermion-operator contributions to the Higgs production via gluon fusion. The red box indicates the four-fermion operator.

For the renormalisation procedure we adopt a mixed on-shell (OS)-

$\overline{\text{MS}}$

– scheme as proposed in [86], in which we renormalise the quark masses OS and the Wilson coefficients of the dimension-six operators using the $\overline{\text{MS}}$ scheme. We hence renormalise the top/bottom mass as

$$m_{t/b}^{\text{OS}} = m_{t/b}^{(0)} - \delta m_{t/b}, \quad (5.5)$$

where the counterterms are given by

$$\delta m_t = \frac{1}{16\pi^2} \frac{C_{Qt}^{(1)} + c_F C_{Qt}^{(8)}}{\Lambda^2} m_t^3 \left[\frac{2}{\bar{\epsilon}} + 2 \log \left(\frac{\mu_R^2}{m_t^2} \right) + 1 \right] \quad (5.6)$$

$$+ \frac{1}{16\pi^2} \frac{(2N_c + 1)C_{QtQb}^{(1)} + c_F C_{QtQb}^{(8)}}{\Lambda^2} \left[\frac{1}{\bar{\epsilon}} + \log \left(\frac{\mu_R^2}{m_b^2} \right) + 1 \right] m_b^3, \quad (5.7)$$

$$\delta m_b = \frac{1}{16\pi^2} \frac{(2N_c + 1)C_{QtQb}^{(1)} + c_F C_{QtQb}^{(8)}}{\Lambda^2} \left[\frac{1}{\bar{\epsilon}} + \log \left(\frac{\mu_R^2}{m_t^2} \right) + 1 \right] m_t^3,$$

with $\bar{\epsilon}^{-1} = \epsilon^{-1} - \gamma_E + \log(4\pi)$, in dimensional regularization with $d = 4 - 2\epsilon$, $N_c = 3$ the number of colors, and $c_F = (N_c^2 - 1)/(2N_c) = 4/3$ the $SU(3)$ quadratic Casimir in the fundamental representation. We note that, for the calculations of the physical processes in this paper, the difference between using the OS or the $\overline{\text{MS}}$ definitions of the top and bottom masses in SMEFT results in changes that are formally of $\mathcal{O}(1/\Lambda^4)$.⁴ We note though that using a SM running $\overline{\text{MS}}$ bottom mass instead of an OS one makes a relevant difference in the numerical results. In the results presented below we will use the OS bottom mass as an input.

The coefficients of the dimension-six operators are renormalised in the $\overline{\text{MS}}$ scheme. At one-loop level the only operators entering the Higgs to gluon or photon rates that mix with the four-quark operators are the ones that modify the top or bottom Yukawa couplings: $\mathcal{O}_{t\phi}$ and $\mathcal{O}_{b\phi}$, respectively. The coefficients of these operators are renormalized according to

$$C_{t\phi/b\phi}^{\overline{\text{MS}}} = C_{t\phi/b\phi}^{(0)} + \delta C_{t\phi/b\phi} \quad \text{with} \quad \delta C_{t\phi/b\phi} = -\frac{1}{2\bar{\epsilon}} \frac{1}{16\pi^2} \gamma_{t\phi/b\phi}^j C_j. \quad (5.10)$$

The only four-quark Wilson coefficients contributing to $\gamma_{t\phi/b\phi}$ are the ones from $\mathcal{O}_{Qt}^{(1),(8)}$ and $\mathcal{O}_{QtQb}^{(1),(8)}$. The explicit expressions for the relevant one-loop anomalous dimension can be obtained from ref. [66, 67]. The Wilson coefficients $C_{t\phi/b\phi}$ modify the Higgs couplings to top quarks/bottom quarks as follows

$$g_{ht\bar{t}/hb\bar{b}} = \frac{m_{t/b}}{v} - \frac{v^2}{\Lambda^2} \frac{C_{t\phi/b\phi}}{\sqrt{2}}. \quad (5.11)$$

⁴In the $\overline{\text{MS}}$ scheme the mass counterterms become

$$\delta m_t^{\overline{\text{MS}}} = \frac{1}{8\pi^2} \frac{C_{Qt}^{(1)} + c_F C_{Qt}^{(8)}}{\Lambda^2} m_t^3 \frac{1}{\bar{\epsilon}} + \frac{1}{16\pi^2} \frac{(2N_c + 1)C_{QtQb}^{(1)} + c_F C_{QtQb}^{(8)}}{\Lambda^2} \frac{1}{\bar{\epsilon}} m_b^3, \quad (5.8)$$

$$\delta m_b^{\overline{\text{MS}}} = \frac{1}{16\pi^2} \frac{(2N_c + 1)C_{QtQb}^{(1)} + c_F C_{QtQb}^{(8)}}{\Lambda^2} \frac{1}{\bar{\epsilon}} m_t^3. \quad (5.9)$$

Hence, a modification of the Higgs couplings to bottom and top quarks is generated by operator mixing, even if $C_{t\phi/b\phi}$ are zero at Λ .

The modification of the Higgs production rate in gluon fusion (ggF) can be written as

$$\frac{\sigma_{ggF}}{\sigma_{ggF}^{\text{SM}}} = 1 + \frac{\sum_{i=t,b} 2\text{Re}(F_{\text{LO}}^i F_{\text{NLO}}^*)}{|F_{\text{LO}}^t + F_{\text{LO}}^b|^2} \quad (5.12)$$

with

$$F_{\text{LO}}^i = -\frac{8m_i^2}{m_h^2} \left[1 - \frac{1}{4} \log^2(x_i) \left(1 - \frac{4m_i^2}{m_h^2} \right) \right] \quad (5.13)$$

where m_h is the Higgs mass, and

$$\begin{aligned} F_{\text{NLO}} = & \frac{1}{4\pi^2\Lambda^2} (C_{Qt}^{(1)} + c_F C_{Qt}^{(8)}) F_{\text{LO}}^t \left[2m_t^2 + \frac{1}{4}(m_h^2 - 4m_t^2) \left(3 + 2\sqrt{1 - \frac{4m_t^2}{m_h^2}} \log(x_t) \right) \right. \\ & \left. + \frac{1}{2}(m_h^2 - 4m_t^2) \log\left(\frac{\mu_R^2}{m_t^2}\right) \right] \\ & + \frac{1}{32\pi^2\Lambda^2} ((2N_c + 1)C_{QtQb}^{(1)} + c_F C_{QtQb}^{(8)}) \left[F_{\text{LO}}^b \frac{m_t}{m_b} (4m_t^2 - 2m_h^2 \right. \\ & \left. - (m_h^2 - 4m_t^2) \sqrt{1 - \frac{4m_t^2}{m_h^2}} \log(x_t) - (m_h^2 - 4m_t^2) \log\left(\frac{\mu_R^2}{m_t^2}\right) \right) + (t \leftrightarrow b) \right]. \end{aligned} \quad (5.14)$$

Only top quark loops contribute to the parts proportional to $C_{Qt}^{(1),(8)}$. We have neglected the contributions of the operators with Wilson coefficient $C_{Qb}^{(1),(8)}$ as they would lead only to subleading contributions proportional to m_b^3 . The variable x_i for a loop particle with mass m_i is given by

$$x_i = \frac{-1 + \sqrt{1 - \frac{4m_i^2}{m_h^2}}}{1 + \sqrt{1 - \frac{4m_i^2}{m_h^2}}}. \quad (5.15)$$

In analogy to (5.12), we can write the modified decay rates of the Higgs boson to gluons as

$$\frac{\Gamma_{h \rightarrow gg}}{\Gamma_{h \rightarrow gg}^{\text{SM}}} = 1 + \frac{\sum_{i=t,b} 2\text{Re}(F_{\text{LO}}^i F_{\text{NLO}}^*)}{|F_{\text{LO}}^t + F_{\text{LO}}^b|^2} \quad (5.16)$$

and

$$\frac{\Gamma_{h \rightarrow \gamma\gamma}}{\Gamma_{h \rightarrow \gamma\gamma}^{\text{SM}}} = 1 + \frac{2\text{Re}(F_{\text{LO},\gamma} F_{\text{NLO},\gamma}^*)}{|F_{\text{LO},\gamma}|^2}. \quad (5.17)$$

In the latter

$$F_{\text{LO},\gamma} = N_C Q_t^2 F_{\text{LO}}^t + N_C Q_b^2 F_{\text{LO}}^b + F_{\text{LO}}^W + F_{\text{LO}}^G, \quad (5.18)$$

and $F_{\text{NLO},\gamma}$ is obtained from F_{NLO} by replacing the LO form factor that appears inside of it by $F_{\text{LO}}^i \rightarrow N_c Q_i^2 F_{\text{LO}}^i$, with the charges $Q_t = 2/3$ and $Q_b = -1/3$. The W boson contribution

$$F_{\text{LO}}^W = 2 \left(1 + 6 \frac{m_W^2}{m_h^2} \right) - 6 \frac{m_W^2}{m_h^2} \left(1 - 2 \frac{m_W^2}{m_h^2} \right) \log^2(x_W), \quad (5.19)$$

with m_W the W mass, and the Goldstone contribution

$$F_{\text{LO}}^G = 4 \frac{m_W^2}{m_h^2} \left(1 + \frac{m_W^2}{m_h^2} \log^2(x_W) \right). \quad (5.20)$$

The formulae presented above are valid under the assumption that, at the electroweak scale, the four-quark operators are the only new physics contributions in the dimension-six effective Lagrangian. If, on the other hand, one assumes that the four-quark operators are defined at some high scale Λ , e.g. after matching with an specific ultraviolet (UV) model, further (logarithmic) contributions appear during the running to low energies, as a result of the mixing between these four-fermion interactions and those operators that would modify the processes at LO. Those effects can be included via the renormalisation group equation (RGE) for the operators with Wilson coefficient $C_{t\phi}$ and $C_{b\phi}$ [66, 67], that lead approximatively to

$$\begin{aligned} C_{t\phi}(\mu_R) - C_{t\phi}(\Lambda) = & \frac{1}{16\pi^2 v^2} \left[-2y_t(m_h^2 - 4m_t^2)(C_{Qt}^{(1)} + c_F C_{Qt}^{(8)}) \log\left(\frac{\mu_R^2}{\Lambda^2}\right) \right. \\ & \left. + \frac{y_b}{2}(m_h^2 - 4m_b^2) \left((2N_c + 1)C_{QtQb}^{(1)} + c_F C_{QtQb}^{(8)} \right) \log\left(\frac{\mu_R^2}{\Lambda^2}\right) \right] \end{aligned} \quad (5.21)$$

and

$$C_{b\phi}(\mu_R) - C_{b\phi}(\Lambda) = \frac{y_t}{32\pi^2 v^2} \left[(m_h^2 - 4m_t^2) \left((2N_c + 1)C_{QtQb}^{(1)} + c_F C_{QtQb}^{(8)} \right) \log\left(\frac{\mu_R^2}{\Lambda^2}\right) \right], \quad (5.22)$$

where $y_{t/b} = \sqrt{2}m_{t/b}/v$. Note that the combinations of Wilson coefficients appearing in (5.21)(5.22) are the same as in F_{NLO} in (5.14). Effectively, we can then obtain the result under the assumption that the four-fermion operators are the only non-zero ones at the high scale by replacing in (5.14) $\mu_R \rightarrow \Lambda$, noting that we have renormalised the top and bottom quark mass in the OS scheme.

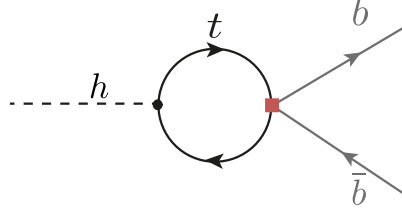


Figure 5.2. Feynman diagram contributing to the NLO $h \rightarrow b\bar{b}$ process.

5.3.2 Higgs decay to bottom quarks

The dominant four-fermion contributions to decay channel $h \rightarrow b\bar{b}$ come from the operators with Wilson coefficients $C_{QtQb}^{(1),(8)}$. The corresponding diagram at NLO is shown in fig 5.2. Adopting the same renormalisation procedure as outlined in the previous subsection, we obtain the following expression for the correction to the $h \rightarrow b\bar{b}$ decay rate in the presence of $\mathcal{O}_{QtQb}^{(1),(8)}$,

$$\begin{aligned} \frac{\Gamma_{h \rightarrow b\bar{b}}}{\Gamma_{h \rightarrow b\bar{b}}^{\text{SM}}} = & 1 + \frac{1}{16\pi^2} \frac{m_t}{m_b} (m_h^2 - 4m_t^2) \frac{(2N_c + 1)C_{QtQb}^{(1)} + c_F C_{QtQb}^{(8)}}{\Lambda^2} \\ & \times \left[2 + \sqrt{1 - \frac{4m_t^2}{m_h^2}} \log(x_t) - \log\left(\frac{m_t^2}{\mu_R^2}\right) \right], \end{aligned} \quad (5.23)$$

which carries an enhancement factor of m_t/m_b and is hence expected to be rather large. Again, we have neglected subdominant contributions suppressed by the bottom mass from the operators $\mathcal{O}_{Qb}^{(1),(8)}$. Including the leading logarithmic running of $C_{b\phi}$ of (5.22) from the high scale Λ to the electroweak scale is achieved by setting in (5.23) $\mu_R \rightarrow \Lambda$. The expression in (5.23) agrees with results obtained from the full calculation of the NLO effects in the dimension-six SMEFT, first computed in [87].

This closes the discussion of the main effects that the third-generation four-quark operators can have in the different Higgs decay widths.⁵ Note also that these modifications of the Higgs decay rate to photons, gluons and, especially, bottom quarks, affect all the branching ratios (BRs) due to the modification of the Higgs total width, and therefore have an observable effect in all Higgs processes measured at the LHC.

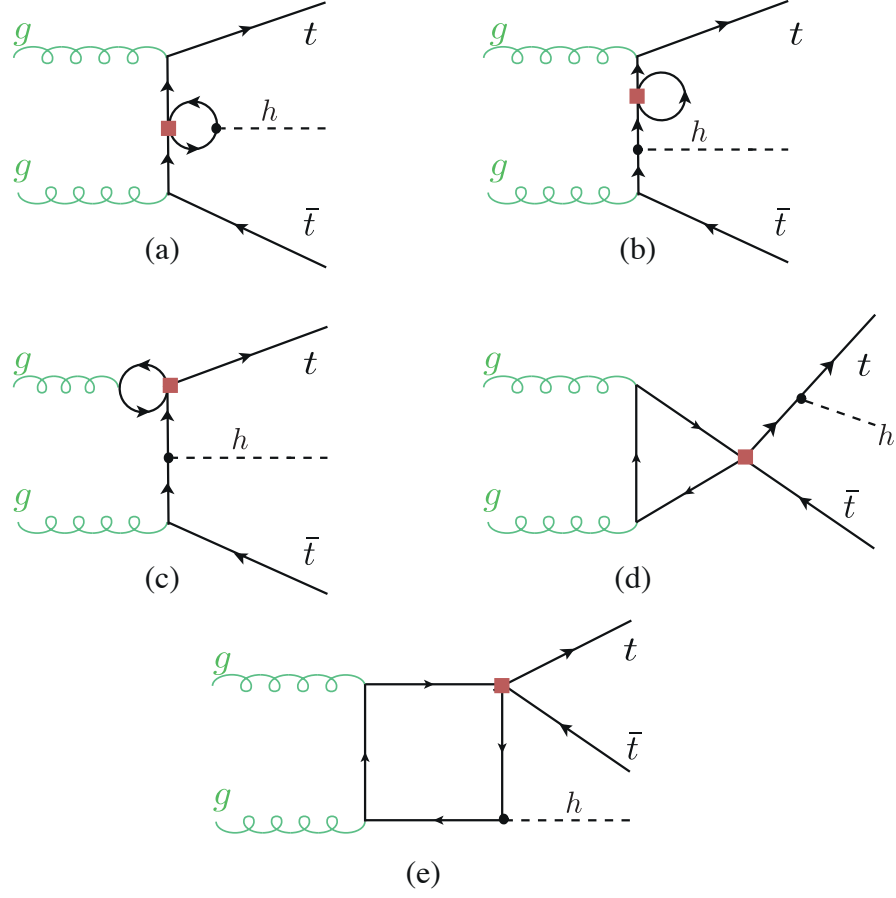


Figure 5.3. Feynman diagrams including the four-fermion loop contributions to the $gg \rightarrow t\bar{t}h$ subprocess.

5.3.3 Associated production of a Higgs boson with top quarks

The associated Higgs production with top quarks, $t\bar{t}h$, receives significant NLO corrections from the singlet and octet operators $\mathcal{O}_{Qt}^{(1),(8)}$, while the contributions from $\mathcal{O}_{QtQb}^{(1),(8)}$ remain small. In addition, there are some small contributions from the singlet and triplet left-handed operators, $\mathcal{O}_{QQ}^{(1),(3)}$, and the right-handed four-top operator, \mathcal{O}_{tt} , as well. The $t\bar{t}h$ process can be either initiated by gluons, see Figure 5.3, or by a quark anti-quark pair, see Figure 5.4. The triangle and box topologies (shown as (d) and (e) in Figure 5.3

⁵Four-fermion operators also affect the $h \rightarrow Z\gamma$ partial width. However, as in the diphoton case, the effect is expected to be small due to the dominance of the W boson loop. Because of this, and given the smallness of the $h \rightarrow Z\gamma$ branching ratio and the relatively low precision expected in this channel at the LHC, we neglect the effects of four-fermion interactions in this decay.

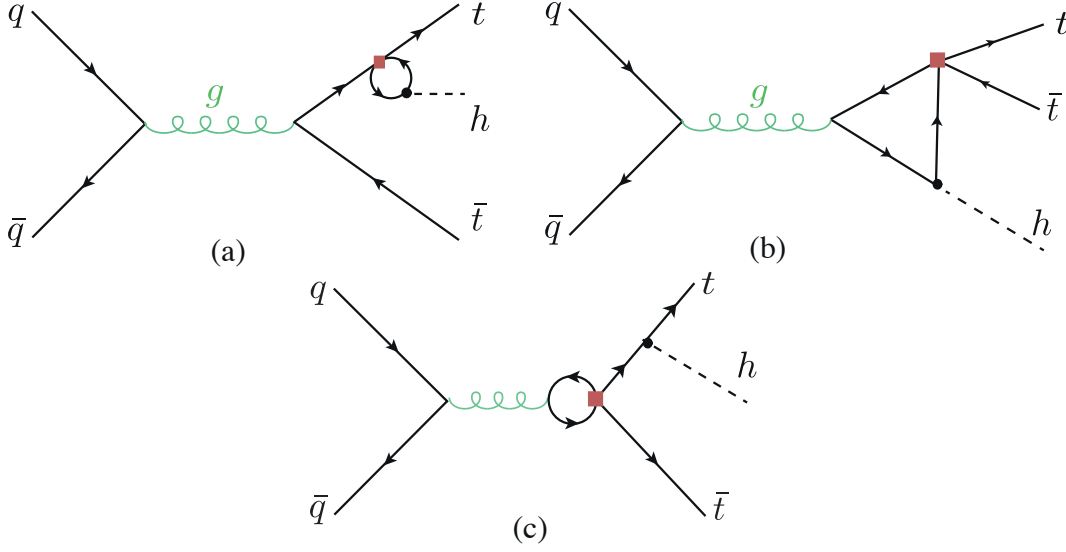


Figure 5.4. Feynman diagrams including the four-fermion loop contributions to the $q\bar{q} \rightarrow t\bar{t}h$ subprocess.

and as (b) in Figure 5.4) are finite. While for Higgs production/decay in/to gluons only certain combinations of singlet/octet operators entered, leading to a degeneracy, this is not the case for $t\bar{t}h$ production, where the gluons no longer need to combine to a colour singlet state. The degeneracy between the singlet and octet operators is mainly broken by the contributions from the triangle diagrams, where, for instance, the difference between the contributions of $\mathcal{O}_{Qt}^{(1)}$ and $\mathcal{O}_{Qt}^{(8)}$ does not follow the same color structure as other diagrams.

We adopt a four-flavour scheme for the computation of the quark-initiated contributions. We note that within a five-flavour scheme operators containing both bottom and top quarks lead to a LO contribution from a direct contact diagram. Nevertheless, this gives an overall negligible correction as the $b\bar{b}$ initiated $t\bar{t}h$ process is suppressed by the small bottom parton distribution functions. The effect of changing the flavour scheme results in an uncertainty of 1 – 2%.

We have computed the NLO corrections using `Madgraph_aMCNLO` [88] (version 3.1.0) with the `SMEFTatNLO v1.0.2` model [64]. The results were cross-checked by an analytic computation⁶, based on the reduction of one-loop amplitudes via the method developed by G. Ossola, C.G. Papadopoulos and R. Pittau (OPP reduction) [89]. The OPP reduction was done using the `CutTools` programme [90]. It reduces the one-loop amplitude into 1,2,3 and 4-point loop functions in four dimensions, keeping spurious terms from

⁶The `FORTAN` code containing this analytical calculation can be provided on request.

the ϵ part of the amplitude. To correct for such terms, one needs to compute the divergent UV counterterm as well as a finite rational terms, denoted R_2 as in Ref. [91].⁷ The amplitudes were generated in the same way as for gluon fusion. The UV and R_2 counterterms, that need to be supplemented to **CutTools**, were computed manually following the method detailed in [91]. The UV counterterms are the same as for gluon fusion, in addition to a new one that is needed to be introduced to renormalise diagrams of type (c) in Figure 5.3 and Figure 5.4. This is due to the operator mixing of light – heavy four-quark operators with heavy four-quark operators. Effectively, this leads to a counterterm

$$\text{Diagram (c)} = \frac{ig_s}{12\pi^2\Lambda^2} T_{ij}^A p_g^2 \gamma^\mu \left(C_{tt} P_R + (C_{QQ}^{(1)} + C_{QQ}^{(3)}) P_L + \frac{C_{Qt}^{(8)}}{4} \right) \left(\frac{1}{\epsilon} - 1 \right). \quad (5.24)$$

Since the singlet and octet operators $\mathcal{O}_{QtQb}^{(1),(8)}$ are not implemented in the current version of **SMEFTatNLO**, or in any other loop-capable **UFO** model available, we have modified the **SMEFTatNLO** model to include these operators, by including their Feynman rules and computing the UV and R_2 counterterms needed for the $t\bar{t}h$ calculation. These $\mathcal{O}_{QtQb}^{(1),(8)}$ contributions are included for consistency, as they were relevant and thus included in the calculation of, e.g. $h \rightarrow b\bar{b}$. However, as we will argue below, their contribution to $t\bar{t}h$ is rather small. Similarly, other “mixed” bottom-top operators are expected to give also suppressed contributions, compared to those from four-top operators. Therefore we neglect their effects in our calculation.⁸

Again, to connect with specific models that may generate the four-quark operators at the new physics scale Λ , one needs to consider the contributions that come from the running from Λ to low energies, and that mix these operators with those entering in $t\bar{t}h$ at the LO level. For the gluon-initiated subprocess the relevant contributions are from the running of $C_{t\phi}$ in (5.21), while for the quark-initiated subprocess we need to account for the mixing of the third generation four-fermion operators with the ones connecting the third generation with the first two generations. The corresponding corrections can be obtained from the RGEs in refs. [66–68].

5.3.4 Results

Here we provide semi-analytical expressions for the results of our NLO calculations including the effects of the third generation four-quark operators. These NLO contribu-

⁷Another rational term R_1 appears due to the mismatch between the four and d dimensional amplitudes, but this is computed automatically in **CutTools**.

⁸Furthermore, we note that such operators are also currently not included in **SMEFTatNLO**. A computation of their contributions, while being beyond the scope of this paper, would require a similar strategy as for the $\mathcal{O}_{QtQb}^{(1),(8)}$ operator.

tions to the single Higgs rates, as a function of the four-heavy-quark Wilson coefficients, are denoted by

$$\delta R(C_i) = R/R^{\text{SM}} - 1, \quad (5.25)$$

where R stands generically for partial width Γ or cross section σ . They are summarised in Table 5.1. The numbers consider only the linear contributions in Λ^{-2} . The respective $\delta R(C_i)$ get a contribution from the computation of the finite corrections to the process and an additional contribution from operator mixing due to RGE running and can hence be split into two parts

$$\delta R(C_i) = \frac{C_i}{\Lambda^2} \left(\delta R_{C_i}^{\text{fin}} + \delta R_{C_i}^{\text{log}} \log \left(\frac{\mu_R^2}{\Lambda^2} \right) \right). \quad (5.26)$$

We note that the way we write our results corresponds to the finite part of the NLO correction taken at a typical process scale μ_R and a contribution obtained by solving the RGE of the dimension-six Wilson coefficients via the leading log approximation from the high scale Λ to the low scale μ_R . Both the finite part dependence $\delta R_{C_i}^{\text{fin}}$ of these corrections on the Wilson coefficient as well as the part proportional to the logarithm $\delta R_{C_i}^{\text{log}}$ are reported in table 5.1. Our results can be improved by replacing the part proportional to the coefficients $\delta R_{C_i}^{\text{log}}$ by solving the coupled system of RGEs. For $\Lambda = 1$ TeV, and depending on the renormalisation scale of the process, the value of the logarithm in (5.26) ranges between $\sim [-5.5, -2.9]$. With these numerical values in mind and by looking at $\delta R_{C_i}^{\text{log}}$ in table 5.1, we see that the finite part of the NLO calculation, i.e. $\delta R_{C_i}^{\text{fin}}$, is usually of the same order of magnitude or larger than the leading-log part, with the exception of the $C_{QtQb}^{(1),(8)}$ contributions to the $h \rightarrow b\bar{b}$. This underlines the importance of considering the full NLO computation in the determination of the Wilson coefficients for $C_{Qt}^{(1),(8)}$, whereas for $C_{QtQb}^{(1),(8)}$, where the limits are mainly driven by $h \rightarrow b\bar{b}$, they turn out to play less important role.

The numerical values were obtained using as input parameters

$$\begin{aligned} G_F &= 1.166378 \cdot 10^{-5} \text{ GeV}^{-2}, \quad m_W = 80.379 \text{ GeV}, \quad m_Z = 91.1876 \text{ GeV}, \\ m_t^{\text{OS}} &= 172.5 \text{ GeV}, \quad m_b^{\text{OS}} = 4.7 \text{ GeV}, \quad m_h = 125.1 \text{ GeV}, \end{aligned} \quad (5.27)$$

and the NNPDF23 set at NLO [92].

Looking at the results, first we note that the operators $\mathcal{O}_{QQ}^{(1),(3)}$ and \mathcal{O}_{tt} only contribute to $t\bar{t}h$ production. In this regard, however, it must be noted that the uncertainties of the renormalisation schemes, the scale uncertainty, the PDF+ α_s uncertainty and the one of the flavour schemes of the $t\bar{t}h$ process are $\sim 5\%$. This is larger than the typical effects of $C_{QQ}^{(1),(3)}$ and C_{tt} for $\mathcal{O}(1)$ coefficients. Therefore, all Higgs rates are expected to be relatively insensitive to these interactions unless rather large values of these Wilson

Operator	Process	μ_R	$\delta R_{C_i}^{fin} [\text{TeV}^2]$	$\delta R_{C_i}^{log} [\text{TeV}^2]$
$\mathcal{O}_{Qt}^{(1)}$	ggF	$\frac{m_h}{2}$	$9.91 \cdot 10^{-3}$	$2.76 \cdot 10^{-3}$
	$h \rightarrow gg$	m_h	$6.08 \cdot 10^{-3}$	$2.76 \cdot 10^{-3}$
	$h \rightarrow \gamma\gamma$	m_h	$-1.76 \cdot 10^{-3}$	$-0.80 \cdot 10^{-3}$
	$t\bar{t}h$ 13 TeV	$m_t + \frac{m_h}{2}$	$-4.20 \cdot 10^{-1}$	$-2.78 \cdot 10^{-3}$
	$t\bar{t}h$ 14 TeV	$m_t + \frac{m_h}{2}$	$-4.30 \cdot 10^{-1}$	$-2.78 \cdot 10^{-3}$
$\mathcal{O}_{Qt}^{(8)}$	ggF	$\frac{m_h}{2}$	$1.32 \cdot 10^{-2}$	$3.68 \cdot 10^{-3}$
	$h \rightarrow gg$	m_h	$8.11 \cdot 10^{-3}$	$3.68 \cdot 10^{-3}$
	$h \rightarrow \gamma\gamma$	m_h	$-2.09 \cdot 10^{-3}$	$-1.07 \cdot 10^{-3}$
	$t\bar{t}h$ 13 TeV	$m_t + \frac{m_h}{2}$	$6.53 \cdot 10^{-2}$	$-2.24 \cdot 10^{-3}$
	$t\bar{t}h$ 14 TeV	$m_t + \frac{m_h}{2}$	$7.29 \cdot 10^{-2}$	$-2.24 \cdot 10^{-3}$
$\mathcal{O}_{QtQb}^{(1)}$	ggF	$\frac{m_h}{2}$	$2.84 \cdot 10^{-2}$	$9.21 \cdot 10^{-3}$
	$h \rightarrow gg$	m_h	$1.57 \cdot 10^{-2}$	$9.21 \cdot 10^{-3}$
	$h \rightarrow \gamma\gamma$	m_h	$-1.30 \cdot 10^{-3}$	$-0.78 \cdot 10^{-3}$
	$h \rightarrow b\bar{b}$	m_h	$9.25 \cdot 10^{-2}$	$1.68 \cdot 10^{-1}$
	$t\bar{t}h$ 13 TeV	$m_t + \frac{m_h}{2}$	$-3.23 \cdot 10^{-6}$	$-9.16 \cdot 10^{-6}$
$\mathcal{O}_{QtQb}^{(8)}$	$t\bar{t}h$ 14 TeV	$m_t + \frac{m_h}{2}$	$-3.51 \cdot 10^{-6}$	$-9.16 \cdot 10^{-6}$
	ggF	$\frac{m_h}{2}$	$5.41 \cdot 10^{-3}$	$1.76 \cdot 10^{-3}$
	$h \rightarrow gg$	m_h	$2.98 \cdot 10^{-3}$	$1.76 \cdot 10^{-3}$
	$h \rightarrow \gamma\gamma$	m_h	$-0.25 \cdot 10^{-3}$	$-0.15 \cdot 10^{-3}$
	$h \rightarrow b\bar{b}$	m_h	$1.76 \cdot 10^{-2}$	$3.20 \cdot 10^{-2}$
$\mathcal{O}_{QQ}^{(1)}$	$t\bar{t}h$ 13 TeV	$m_t + \frac{m_h}{2}$	$1.75 \cdot 10^{-3}$	$1.90 \cdot 10^{-3}$
	$t\bar{t}h$ 14 TeV	$m_t + \frac{m_h}{2}$	$2.35 \cdot 10^{-3}$	$1.90 \cdot 10^{-3}$
$\mathcal{O}_{QQ}^{(3)}$	$t\bar{t}h$ 13 TeV	$m_t + \frac{m_h}{2}$	$0.66 \cdot 10^{-3}$	$5.50 \cdot 10^{-3}$
	$t\bar{t}h$ 14 TeV	$m_t + \frac{m_h}{2}$	$0.44 \cdot 10^{-3}$	$5.50 \cdot 10^{-3}$
\mathcal{O}_{tt}	$t\bar{t}h$ 13 TeV	$m_t + \frac{m_h}{2}$	$7.50 \cdot 10^{-3}$	$2.01 \cdot 10^{-3}$
	$t\bar{t}h$ 14 TeV	$m_t + \frac{m_h}{2}$	$6.45 \cdot 10^{-3}$	$2.01 \cdot 10^{-3}$

Table 5.1. The NLO corrections from the four heavy-quark SMEFT operators of this study to single Higgs rates. We have separated the contributions into the finite piece $\delta R_{C_i}^{fin}$ and the leading log running of the Wilson coefficients $\delta R_{C_i}^{log}$, see (5.26).

coefficients are allowed. Secondly, from the analytic results, we observe that in the NLO corrections to Higgs rates, the Wilson coefficients $C_{QtQb}^{(1)}$, $C_{QtQb}^{(8)}$ always appear in a linear combination identical to the one seen in the RGE of the Wilson coefficients $C_{t\phi}$ and $C_{b\phi}$, i.e.

$$C_{QtQb}^+ = (2N_c + 1)C_{QtQb}^{(1)} + c_F C_{QtQb}^{(8)}. \quad (5.28)$$

The exception is the $t\bar{t}h$ process, which has a small finite part contribution that breaks

this relation. However, this finite part is suppressed by the bottom quark mass and therefore it is very small. Thus, all single Higgs rates are mostly sensitive to the linear combination in (5.28). We finally note that apart from $\mathcal{O}_{Qt}^{(1),(8)}$ all the other operators produce only small contributions to the $t\bar{t}h$ process. In particular, the top-bottom operators $\mathcal{O}_{QtQb}^{(1),(8)}$ show a suppression with m_b , which also typically results in contributions below the theoretical uncertainties. (We explicitly checked this in our calculation and by setting $m_b = 0$ in the `Madgraph_aMCNLO` simulations.) This is also expected for other “mixed” top-bottom operators, which would contribute via bottom-quark loops and hence would be strongly suppressed, justifying that we did not consider them here.

5.4 Fit to Higgs observables

In this section we will show the results of a combined fit of the four-quark operators of the third generation and the operator that modifies the Higgs potential and hence the Higgs self-coupling. In ref. [70–73, 75] it was proposed to extract the trilinear Higgs self-coupling via its loop effects in single Higgs measurements. Within the assumptions of the SMEFT, a model-independent determination of the triple Higgs self-interaction, λ_3 , should be considered within a global analysis considering all effective interactions that enter up to the same order in perturbation theory as λ_3 . In particular, apart from the trilinear Higgs self-coupling modification, such a study must include those operators that enter at LO in Higgs production and decay [77]. Furthermore, the sensitivity to the Higgs self-coupling modifications can also be diminished by other operators entering as the trilinear Higgs self-coupling via loop effects, if those operators are not yet strongly constrained experimentally by other processes. Such is the case for some of the four-quark operators considered in this paper. In order to show this, we have performed a combined fit to the operator with Wilson coefficient C_ϕ and the four-fermion operators considered in this study. A full global fit including all new physics effects would require the combination of Higgs data with that from other processes and is beyond the scope of this paper.

5.4.1 Fit methodology

For each experimentally observed channel with a signal strength $\mu_{\text{Exp}} \equiv \sigma_{\text{Obs}}/\sigma_{\text{SM}}$, one can build a theoretical prediction for this signal strength, $\mu_{\text{Th}} \equiv \sigma_{\text{Th}}/\sigma_{\text{SM}}$, where $\sigma_{\text{Th}} = \sigma_{\text{Prod}} \times \text{BR}$ includes the effects generated by the dimension-six operators. The theory predictions for the signal strengths are then used to build a test statistic in the form of a log-likelihood of a Gaussian distribution

$$\log(L) = -\frac{1}{2} \left[(\vec{\mu}_{\text{Exp}} - \vec{\mu})^T \cdot \mathbf{V}^{-1} \cdot (\vec{\mu}_{\text{Exp}} - \vec{\mu}) \right]. \quad (5.29)$$

The covariance matrix \mathbf{V} is constructed from the experimental uncertainties $\delta\mu_{\text{Exp}}$ and correlations⁹, as well as the theoretical uncertainties (scale, PDF, α_s , ...).

The log-likelihood of (5.29) was used together with flat priors $\pi(C_i) = \text{const.}$ in a Bayesian fit of the Wilson coefficients of interest. A Markov chain Monte Carlo (MCMC) using `pymc3` [93] was used to construct the posterior distribution. We use the `Arviz` Bayesian analysis package [94] to extract the credible intervals (CIs) from the highest density posterior intervals (HDPI) of the posterior distributions, where the intervals covering 95% (68%) of the posterior distribution are considered the 95% (68%) CIs. In the Gaussian limit, these 95% (68%) CIs should be interpreted as equivalent to the 95% (68%) Frequentist Confidence Level (CL) two-sided bounds. To cross-check the MCMC Bayesian fit, a frequentist Pearson's χ^2 fit was performed using `iminuit` [95, 96], where the χ^2 was taken to be

$$\chi^2 = -2\log(L). \quad (5.30)$$

Both fit results agreed on the 95% and 68% CI (or CL) bounds.¹⁰ The code for the fit, experimental input and the analysis can be found in the repository [100].

In the theoretical predictions for the signal strengths, we will assume that the new physics corrections to the cross sections and the decay widths are linearised, i.e.

$$\mu(C_\phi, C_i) = \frac{\sigma_{\text{Prod}}(C_\phi, C_i) \times \text{BR}(C_\phi, C_i)}{\sigma_{\text{Prod,SM}} \times \text{BR}_{\text{SM}}} \approx 1 + \delta\sigma(C_\phi, C_i) + \delta\Gamma(C_\phi, C_i) - \delta\Gamma_h(C_\phi, C_i), \quad (5.31)$$

with $\delta\sigma$, $\delta\Gamma$, $\delta\Gamma_h$ (Γ_h denotes the Higgs total width) being the NLO corrections, relative to the SM prediction as in (5.25), from the dimension-six operators with Wilson coefficients C_ϕ and C_i . Here, C_i stands schematically for $C_{Qt}^{(1)}$, $C_{Qt}^{(8)}$, $C_{QtQb}^{(1)}$, $C_{QtQb}^{(8)}$, $C_{QQ}^{(1)}$, $C_{QQ}^{(3)}$ and C_{tt} . As mentioned in the previous section, however, the sensitivity to $C_{QQ}^{(1),(3)}$ and C_{tt} is rather small, typically below the theory uncertainty of the calculation, and we will ignore these Wilson coefficients in the fits presented in this section.

In particular, in (5.31) all the corrections from the four-quark operators to the cross sections and decay widths are fully linearised in $1/\Lambda^2$. Given that current bounds on these operators are rather weak, one may wonder about the uncertainty in our fits associated to the truncation of the EFT. Note that, since the four-quark operators only enter into the virtual corrections at NLO, Higgs production and decay contain only linear terms in $1/\Lambda^2$ in the corresponding Wilson coefficients, i.e. the quadratic terms coming from squaring the amplitudes are technically of next-to-NLO. Hence, the quadratic effects in the signal strengths come from not linearising the corrections to the product $\sigma_{\text{Prod}} \times \text{BR}$. We explicitly checked that, for the fits we presented in the next section, the difference between including the full expression of the signal strength or

⁹Correlations amongst channels of $< 10\%$ were ignored.

¹⁰In order to plot the multidimensional posterior distributions and the forest plots we have used a code based on `corner.py` [97], `pygtc` [98] and `zEpid` [99].

the linearised version in (5.31) results in differences in the bounds at the $\lesssim 10\%$ level. The results we present for the four-quark operator are, therefore, relatively stable with respect to the truncation of the EFT expansion. For the \mathcal{O}_ϕ operator, however, there is an additional contribution to the virtual corrections stemming from the wave function renormalisation of the Higgs field. The correction to a given production cross section or decay width, again denoted generically by R , is given by

$$\delta R_{\lambda_3} \equiv \frac{R_{\text{NLO}}(\lambda_3) - R_{\text{NLO}}(\lambda_3^{\text{SM}})}{R_{\text{LO}}} = -2 \frac{C_\phi v^4}{\Lambda^2 m_h^2} C_1 + \left(-4 \frac{C_\phi v^4}{\Lambda^2 m_h^2} + 4 \frac{C_\phi^2 v^8}{m_h^4 \Lambda^4} \right) C_2. \quad (5.32)$$

In (5.32), the coefficient C_1 corresponds to the contribution of the trilinear coupling to the single Higgs processes at one loop, adopting the same notation as [71]. The values of C_1 for the different processes of interest for this paper are given in Appendix ???. The coefficient C_2 describes universal corrections and is given by

$$C_2 = \frac{\delta Z_h}{1 - \left(1 - \frac{2C_\phi v^4}{\Lambda^2 m_h^2} \right)^2 \delta Z_h}, \quad (5.33)$$

where the constant δZ_h is the SM contribution from the Higgs loops to the wave function renormalisation of the Higgs boson,

$$\delta Z_h = -\frac{9}{16} \frac{G_F m_h^2}{\sqrt{2} \pi^2} \left(\frac{2\pi}{3\sqrt{3}} - 1 \right). \quad (5.34)$$

The coefficient C_2 thus introduces additional $\mathcal{O}(1/\Lambda^4)$ (and higher order) terms in δR_{λ_3} . In ref. [71] considering the κ formalism the full expression of (5.33) is kept, while we define two different descriptions: one in which we expand δR_{λ_3} up to linear order and an alternative scheme in which we keep also terms up to $\mathcal{O}(1/\Lambda^4)$ in the EFT expansion. We explicitly checked that keeping the full expression in (5.33) and including terms up to $\mathcal{O}(1/\Lambda^4)$ in C_2 lead to nearly the same results in our fits.

5.4.2 Fit to LHC Run-II data

For the fit we have used inclusive Higgs data from the LHC Run II for centre-of-mass energy of $\sqrt{s} = 13$ TeV and integrated luminosity of 139 fb^{-1} for ATLAS and 137 fb^{-1} for CMS. The experimental input is summarised in Table 2.1 in Appendix ??.

In Figure 5.5 we show the limits of a two-parameter fit for various heavy quark Wilson coefficients C_i , marginalising over C_ϕ . We confront them also with the limits obtained from fits to top data [59, 63, 101–104]. Note that, although our bounds do not come from a global fit, they can be compared with similar results from the fits to top

5 Four top operator in Higgs production and decay

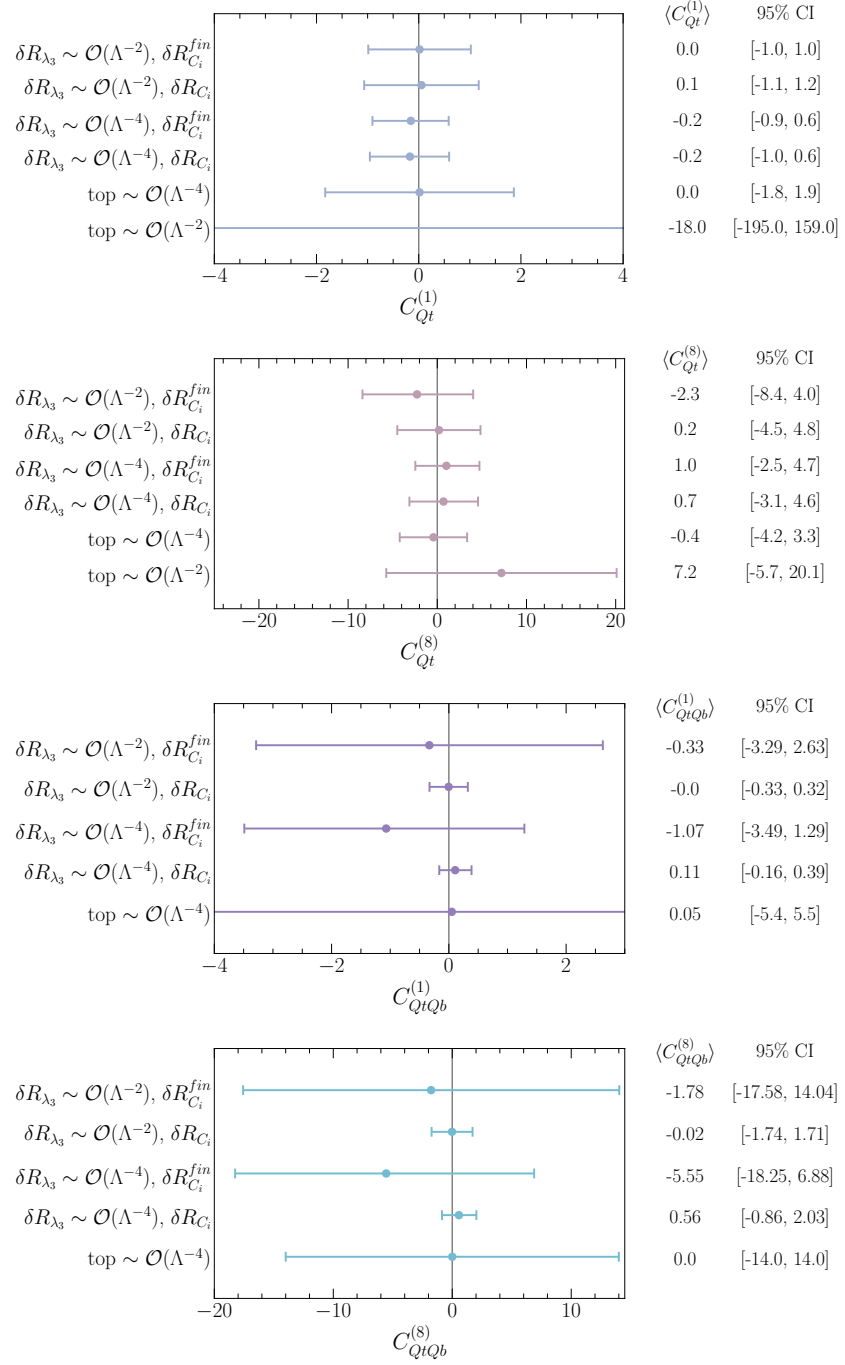


Figure 5.5. Forest plots illustrating the means and 95% CIs of the posteriors built from the four-fermion Wilson coefficients with C_ϕ marginalised. The plots confront also the truncation of the EFT at $\mathcal{O}(1/\Lambda^2)$ and $\mathcal{O}(1/\Lambda^4)$ of δR_{λ_3} as defined in (5.32). The 95% CI bounds stem from Higgs data. The last two rows for each operator show instead the limits obtained by a single parameter fit to top data, linear and quadratic. The top data results are taken from [101] for $C_{Qt}^{(1),(8)}$ and [59] for $C_{QtQb}^{(1),(8)}$.

data that assume that only one operator is “switched on” at a time. In these cases, we find that our new bounds are more stringent or at least comparable to the 95% CI bounds on the C_i operators fit results from top data. We also note that, while the limits from top data show a large uncertainty from the EFT truncation¹¹, even when only one operator is considered at a time, our NLO results for the four-quark operators are quite stable if one considers quadratic effects, as mentioned above. On the other hand, fig. 5.5 also shows that there is a rather large uncertainty associated to the EFT truncation of the effects of the \mathcal{O}_ϕ operator in the wave function renormalization of the Higgs boson. Furthermore, the plot displays the bounds for two different assumptions for the scale at which the operators are defined. The lines showing δR^{fin} assume that there are only the corresponding four-quark operator and \mathcal{O}_ϕ at the electroweak scale¹², while the line corresponding to δR shows the limits assuming that the four-fermion operators (and \mathcal{O}_ϕ) are the only ones at a scale $\Lambda = 1$ TeV. We can again infer from the fact that the bounds remain the same order of magnitude between δR^{fin} and δR that the inclusion of the finite terms for the operators $\mathcal{O}_{Qt}^{(1),(8)}$ is important if the new physics scale is not extremely high. Instead, for the operators $\mathcal{O}_{QtQb}^{(1),(8)}$ the bounds become much stronger when including the logarithmic piece, so we can conclude that in that case the finite piece is less relevant. In all the fit results that we will present in what follows, we will assume that the Wilson coefficients are always evaluated at the scale $\Lambda = 1$ TeV.

In Figure 5.6 we show the limits on C_ϕ for various two-parameter fits including the two different EFT truncations of δR_{λ_3} . We also show the results from a single parameter fit on C_ϕ . For comparison, we show the ATLAS limits from full LHC run-II Higgs pair production in the final state $b\bar{b}\gamma\gamma$ [105] where we have translated the bounds from $\kappa_\lambda \equiv \lambda_3/\lambda_3^{\text{SM}}$ to the SMEFT, keeping both linear and quadratic terms. While the limits on C_ϕ from single and double Higgs production are of similar size when keeping terms up to $\mathcal{O}(1/\Lambda^4)$ in the single Higgs fit, the limits from single Higgs become weaker if one keeps only terms up to $\mathcal{O}(1/\Lambda^2)$. In this case, the fit remains questionable leading to limits beyond the perturbative unitarity bound of ref. [106]. Instead, for Higgs pair production is makes only a negligible effect if linear or up to quadratic terms in the EFT expansion are kept for the $C_\phi > 0$ bound, while the bound weakens at linear order in $1/\Lambda^2$ for $C_\phi < 0$ [107]. We also see that the limits on C_ϕ become significantly weaker in a two-parameter fit with the four-quark operators, indicating that in a proper global SMEFT fit also the loop effects of other weakly constrained operators, such as these, need to be accounted for.

One of the important aspects of multivariate studies is the correlation among vari-

¹¹In particular, for the $C_{QtQb}^{(1),(8)}$ operator the references only calculate contributions of order $\mathcal{O}(1/\Lambda^4)$. (The fit considering only linear terms would result in bounds of order $\mathcal{O}(10^4)$.) Hence, in this case, we only quote the quadratic bounds.

¹²We neglect in this case the small running between the scales involved in the different processes included in the fit.

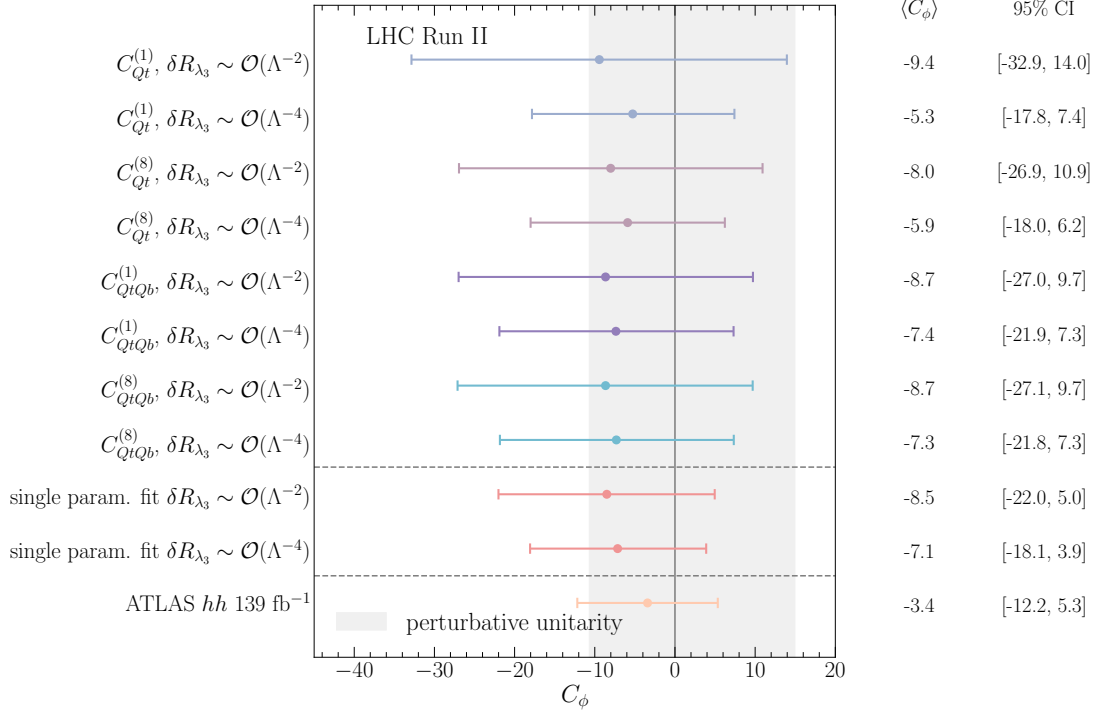


Figure 5.6. A forest plot illustrating the means and 95% CIs of the posteriors built from the C_ϕ in a two-parameter fit with the four-fermion operators marginalised. We compare the fit results for C_ϕ from full run-II Higgs data keeping terms up to $\mathcal{O}(1/\Lambda^2)$ or $\mathcal{O}(1/\Lambda^4)$ in δR_{λ_3} . For comparison, also the 95% CI and means for the single parameter fit for C_ϕ with the same single Higgs data is shown as well as the bounds on C_ϕ from the 139 fb^{-1} search for Higgs pair production [105]. The horizontal grey band illustrates the perturbative unitarity bound [106].

ables. Apart from the two-parameter fits discussed above, here we also consider a four-parameter fit to C_ϕ plus the three directions in the four heavy-quark operator parameter space that the Higgs rates are mostly sensitive too, i.e. neglecting $C_{QQ}^{(1),(3)}$ and C_{tt} , and trading $C_{QtQb}^{(1)}$ and $C_{QtQb}^{(8)}$ by C_{QtQb}^+ . When considering two- or four-parameter fits of C_ϕ and the four-heavy-quark Wilson coefficients, we observe a non-trivial correlation patterns amongst these coefficients. Figure 5.7 illustrates these correlation patterns clearly for the four-parameter fit. We observe that the Wilson coefficients $C_{Qt}^{(1),(8)}$ are strongly correlated because, in analogy to $C_{QtQb}^{(1),(8)}$, they only appear in certain linear combination whenever correcting the Yukawa coupling. However, unlike $C_{QtQb}^{(1),(8)}$ they are not completely degenerate because the main part of the NLO correction to $t\bar{t}h$ does not

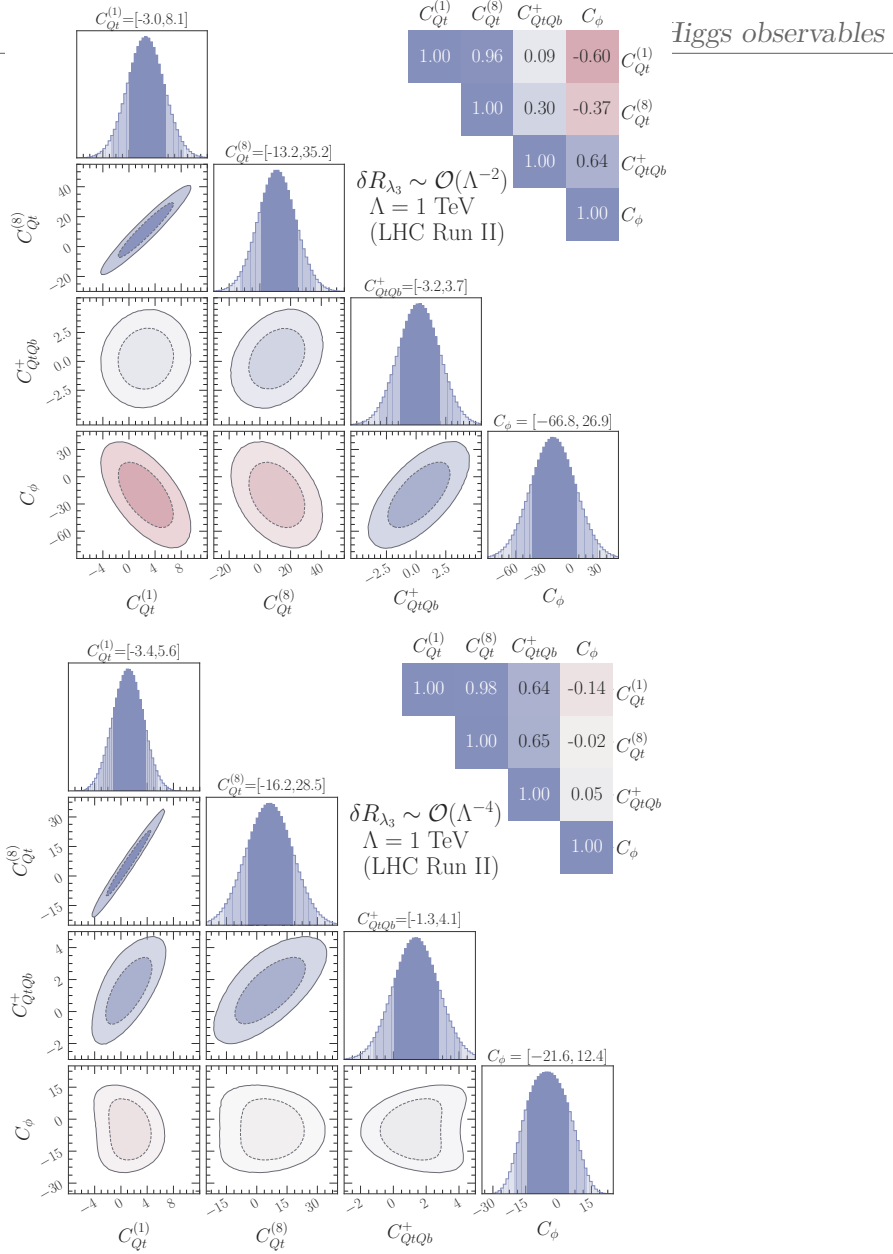


Figure 5.7. The marginalised 68% and 95% HDPI's for the four-parameter fits including the different four-quark Wilson coefficients and C_ϕ . The numbers above the plots show the 95% CI bounds while the correlations are given on the top-right side. These limits correspond to values of the Wilson coefficients evaluated at the scale $\Lambda = 1 \text{ TeV}$. The upper panel shows the fit including up to $\mathcal{O}(1/\Lambda^2)$ in δR_{λ_3} while the lower one shows the fit with including also $\mathcal{O}(1/\Lambda^4)$.

contain the aforementioned linear combination. The four-parameter fit also reveals that the Wilson coefficients $C_{Qt}^{(1),(8)}$ have a large correlation with C_{QtQb}^+ because all of the

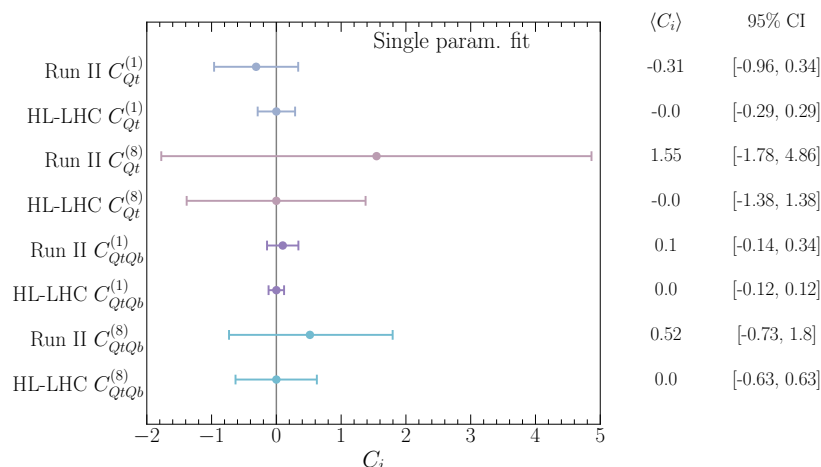


Figure 5.8. Results of a single parameter fit showing the improvement in constraining power of the HL-LHC over the current bounds from Run-2 data. The limits correspond to values of the Wilson coefficients evaluated at the scale $\Lambda = 1$ TeV.

four Wilson coefficients appear in a linear combination in the NLO corrections except for $h \rightarrow b\bar{b}$ and $t\bar{t}h$. However, this correlation is not as strong due to the large NLO correction of the Higgs decay $h \rightarrow b\bar{b}$ from $C_{QtQb}^{(1),(8)}$. Moreover, the correlation between the four-heavy-quark Wilson coefficients and C_ϕ depends on the δR_{λ_3} truncation. In Appendix 5.6 we present similar correlation plots for various two-parameter fits, where the same behaviour of the change in the correlation with the inclusion of quadratic terms δR_{λ_3} is found. The correlation in those cases are though generally stronger.

5.4.3 Prospects for HL-LHC

We now turn to examine the potential of the HL-LHC. For this, we use the CMS projections for the single Higgs signal strengths provided in refs. [51, 108] for a centre-of-mass energy of $\sqrt{s} = 14$ TeV and integrated luminosity of 3 ab^{-1} . We use the projections for the S2 scenario explained in [48]. These assume the improvement on the systematics that is expected to be attained by the end of the HL-LHC physics programme, and that theory uncertainties are improved by a factor of two with respect to current values. These projections are assumed to have their central values in the SM prediction with the total uncertainties summarised in table 2.1 in Appendix ??.¹³

In Figure 5.8 we confront the results of the fits to Run-2 data with the projections for the HL-LHC for single parameter fits. For the operators $\mathcal{O}_{Qt}^{(1),(8)}$ the constraining

¹³The correlation matrix for the S2 scenario can be found on the webpage [108].

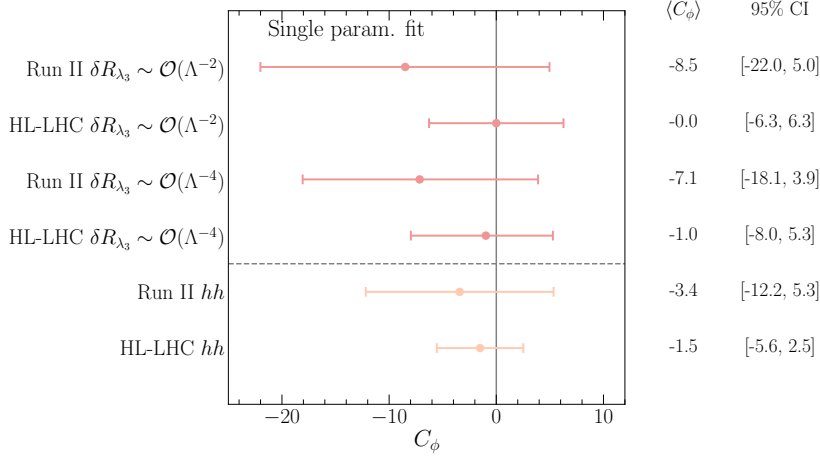


Figure 5.9. A forest plot illustrating the means and 95% CIs of the posteriors built from the C_ϕ in a single-parameter fit, showing also the differences in including terms of $\mathcal{O}(1/\Lambda^2)$ or up to $\mathcal{O}(1/\Lambda^4)$ in the definition of δR_{λ_3} . For comparison, also the limits and projections from searches for Higgs pair production are shown.

power of the HL-LHC is roughly a factor two better as the current bounds we could set from single Higgs data, while for the operators $\mathcal{O}_{QtQb}^{(1),(8)}$ the improvement is a little less. In Figure 5.9 we show the limits on C_ϕ in a single parameter fit for Run-2 and the projections for the HL-LHC including in δR_{λ_3} up to order $\mathcal{O}(1/\Lambda^2)$ or $\mathcal{O}(1/\Lambda^4)$. While for Run-2 data the inclusion of $\mathcal{O}(1/\Lambda^4)$ made a huge difference, this is less pronounced for the HL-LHC projections. Our results are very similar to the projections presented in a κ_λ fit in [109]. We confront this also with data from searches for Higgs pair production 139 fb^{-1} [105] and HL-LHC projections [110] on Higgs pair production, showing that Higgs pair production will still allow to set stronger limits on C_ϕ .

5.5 Summary and discussion

In this paper, we have computed the NLO corrections induced by third generation four-quark operators in Higgs observables that are relevant for its production and decay at the LHC. Our results show that such processes are sensitive to the all possible chiral structures for the third generation four-quark operators in the dimension-six SMEFT, but in different degrees. Operators with different chiralities are, for instance, the only ones that can contribute to Higgs production via gluon fusion, and the decay of the Higgs boson to gluons, photons and bottom quarks pairs. The latter are particularly sensitive to the top-bottom operators $\mathcal{O}_{QtQb}^{(1),(8)}$, which then also significantly affect the

total decay width. In the associate production of a Higgs boson with a top quark pair, on the other hand, all the third generation four-fermion operators enter. Sensitivity to four-quark operators where all fields have the same chirality, however, is only possible for large values of the Wilson coefficients, in a way that they can generate contributions beyond the size of current theory uncertainties. The $t\bar{t}h$ process is also rather important in setting limits on the four-quark operators $\mathcal{O}_{Qt}^{(1)}$ and $\mathcal{O}_{Qt}^{(8)}$, due to the comparatively large NLO corrections they induce in this process with respect to others. It also breaks a degeneracy among the Wilson coefficients of those two operators, which always appear in a single combination for all other processes.

To illustrate the constraining power of single Higgs processes in bounding these four-quark operators, we performed several simplified fits to these interactions and find that the resulting limits from our fits are, in some cases, comparable or better than similar results obtained from top data [59, 101].

We have also performed a combined fit including the above-mentioned four-quark operators and the operator $(\phi^\dagger\phi)^3$, that modifies the Higgs potential and the trilinear Higgs self-coupling. Due to the lack of powerful constraints from top data, the inclusion of the four-fermion operators diminishes the power of setting limits on the trilinear Higgs self-coupling from single Higgs observables. From our analysis we conclude that, in the absence of strong direct bounds on the third-generation four-quark operators, these should be included into a global fit on Higgs data, when attempting to obtain model-independent bounds on the trilinear Higgs self-coupling. The results of our calculations are presented such that they can be easily used by the reader in truly global fits including all other interactions entering at the LO. We leave this, as well as the inclusion of differential Higgs data, to future work.

Finally, we also illustrated the increase in constraining power expected during the high-luminosity phase of the LHC by presenting the HL-LHC projections of the above-mentioned fits.

Moving beyond hadron colliders, it must be noted that the interplay between the Higgs trilinear and four heavy-quark operators in Higgs processes is expected to be less of an issue at future leptonic Higgs factories, such as the FCC-ee [111, 112], ILC [113, 114], CEPC [115, 116] or CLIC [117, 118]. At these machines, the effects of C_ϕ are still “entangled” with those of the four-fermion operators in the Higgs rates, but only through the decay process, i.e. via the contributions to the BRs. However, Higgs production is purely electroweak, namely via Higgs-strahlung (Zh : $e^+e^- \rightarrow Zh$) or W boson fusion, and receives no contributions from the four-quark operators at the same order in perturbation theory where C_ϕ modifies these processes, i.e. NLO. Moreover, at any of these future e^+e^- Higgs factories there is the possibility of obtaining a sub-percent determination of the total Zh cross section at e^+e^- colliders, by looking at events recoiling against the Z decay products with a recoil mass around m_h . This observable is therefore completely insensitive to the four-quark operators, while still receiving NLO

corrections from C_ϕ . Although, in practice, in a global fit one needs to use data from all the various Higgs rates at two different energies to constrain all possible couplings entering at LO in the Higgs processes and also obtain a precise determination of C_ϕ [119], the previous reasons should facilitate the interpretation of the single-Higgs bounds on the Higgs self-coupling at e^+e^- machines.

We conclude this paper with a few words on the relevance of the results presented here when interpreted from the point of view of specific models of new physics. In particular, one important question is *are there models where one expects large contributions to four-top operators while all other interactions entering in Higgs processes are kept small?* Indeed, large contributions to four-top operators can be expected in various BSM scenarios.¹⁴ For instance, in Composite Higgs Models, in which the top quark couples to the strong dynamics by partial compositeness, one expects on dimensional grounds that some of the four-top quark operators are of order $1/f^2$, where f indicates the scale of strong dynamics [60]. By its own nature, however, Composite Higgs models also predict sizeable contributions to the single Higgs couplings $\sim 1/f^2$. While, in general, sizeable modifications of the Higgs interactions are typically expected in scenarios motivated by “naturalness”, this is not necessarily the case in other scenarios. It is indeed possible to think of simple models where modifications of the Higgs self-interactions or contributions to four-quark operators are the only corrections induced by the dimension-six interactions at tree level, see [120]. Thinking, for instance, in terms of scalar extensions of the SM, there are several types of colored scalars whose tree-level effects at low energies can be represented by four-quark operators only, e.g. for complex scalars in the $(6, 1)_{\frac{1}{3}}$ and $(8, 2)_{\frac{1}{2}}$ SM representations (Ω_1 and Φ in the notation of [120]). If these colored states are the only moderately heavy new particles, our results can provide another handle to constrain such extensions. One must be careful, though, as a consistent interpretation of our results for any such models would require to include higher-order corrections in the matching to the SMEFT. At that level, as shown e.g. by the recent results in [121], multiple contributions that modify Higgs processes at LO are generated at the one-loop level, and are therefore equally important as the NLO effects of the (tree-level) generated four-quark operators.¹⁵ In any case, one must note that, even if similar size contributions to single Higgs processes are generated, the four-top or Higgs trilinear effects can provide extra information on the model. For instance, in some of the most common scalar extensions of the SM, with an extra Higgs doublet, $\varphi \sim (1, 2)_{\frac{1}{2}}$, tree-level contributions to some of the four-heavy-quark operators discussed in this paper are generated

¹⁴Generically, models where four-top interactions are much larger than four-fermion operators of the first and second generation can be easily conceived from some UV dynamics coupling mostly to the third generation of quarks hence respecting the Yukawa hierarchies.

¹⁵Furthermore, given that some SMEFT interactions induce tree-level contributions to Higgs processes that in the SM are generated at the loop level, e.g. $\mathcal{O}_{\phi G}$ in gluon fusion, a consistent interpretation in terms of new physics models may require to include up to two-loop effects in the matching for such operators, for which there are currently no results or tools available.

together with modifications on the Higgs trilinear self-coupling. These two effects are independent but they are both correlated with the, also tree level, modifications of the single Higgs couplings. Essentially, the LO effects on Higgs observables are proportional to $\lambda_\varphi y_\varphi^f$, where λ_φ is the scalar interaction strength of the $(\varphi^\dagger \phi)(\phi^\dagger \phi)$ operator and y_φ^f the new scalar Yukawa interaction strength, whereas the NLO effects are proportional to the square of each separate coupling. Hence, these effects might help to resolve (even if only weakly) the flat directions in the model parameter space that would appear in a LO global fit. At the end of the day, for a proper interpretation of the SMEFT results in terms of the widest possible class of BSM models, all the above simply remind us of the importance of being global in SMEFT analyses, to which our work contributes by including effects in Higgs physics that enter at the same order in perturbation theory as modifications of the Higgs self-coupling.

5.6 Two parameter fits

We present in figs. 5.10 and 5.11 the 68% and 95% highest posterior density contours of the two-parameter posterior distributions and their marginalisation for the two-parameter fits involving C_ϕ and one of the four-heavy quark Wilson coefficients, evaluated at the scale $\Lambda = 1$ TeV. Both linearised and quadratically truncated δR_{λ_3} fits are shown, and we observe that the 95% CI bounds (shown on top of the panels) and correlations depends on the truncation.

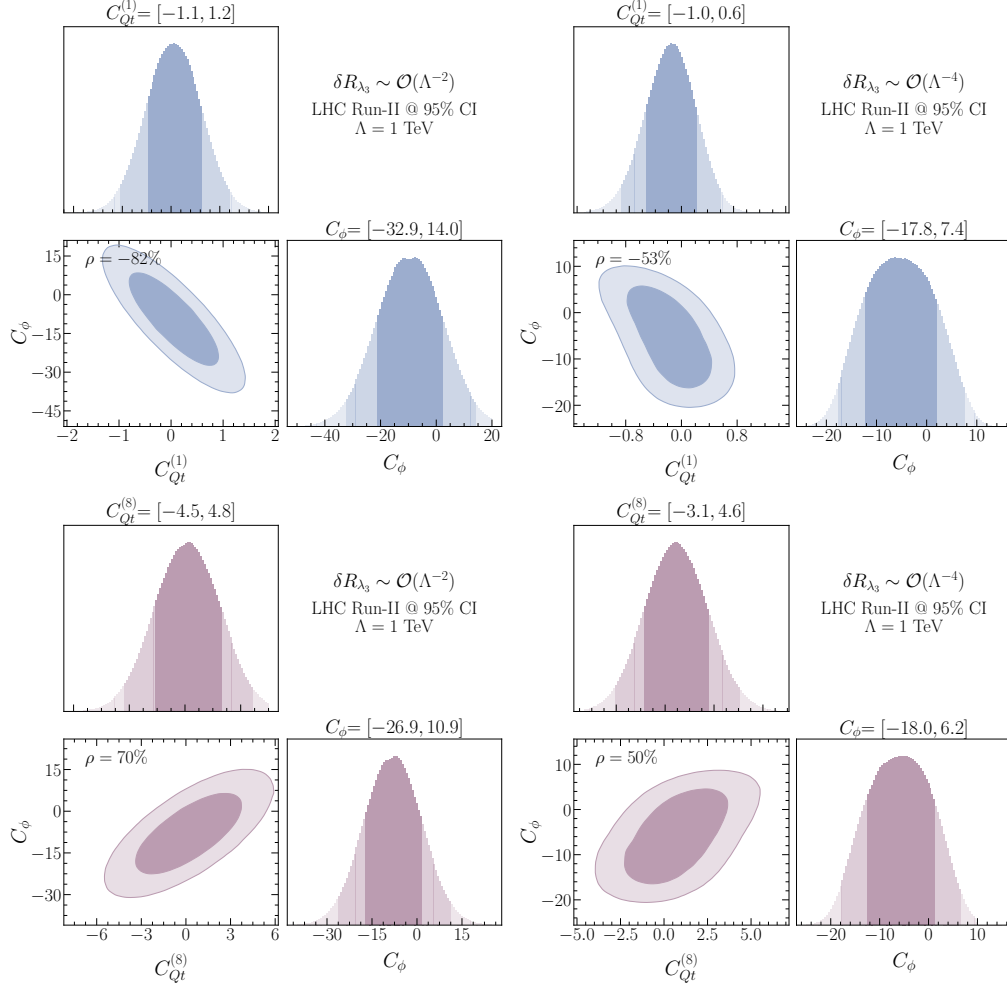
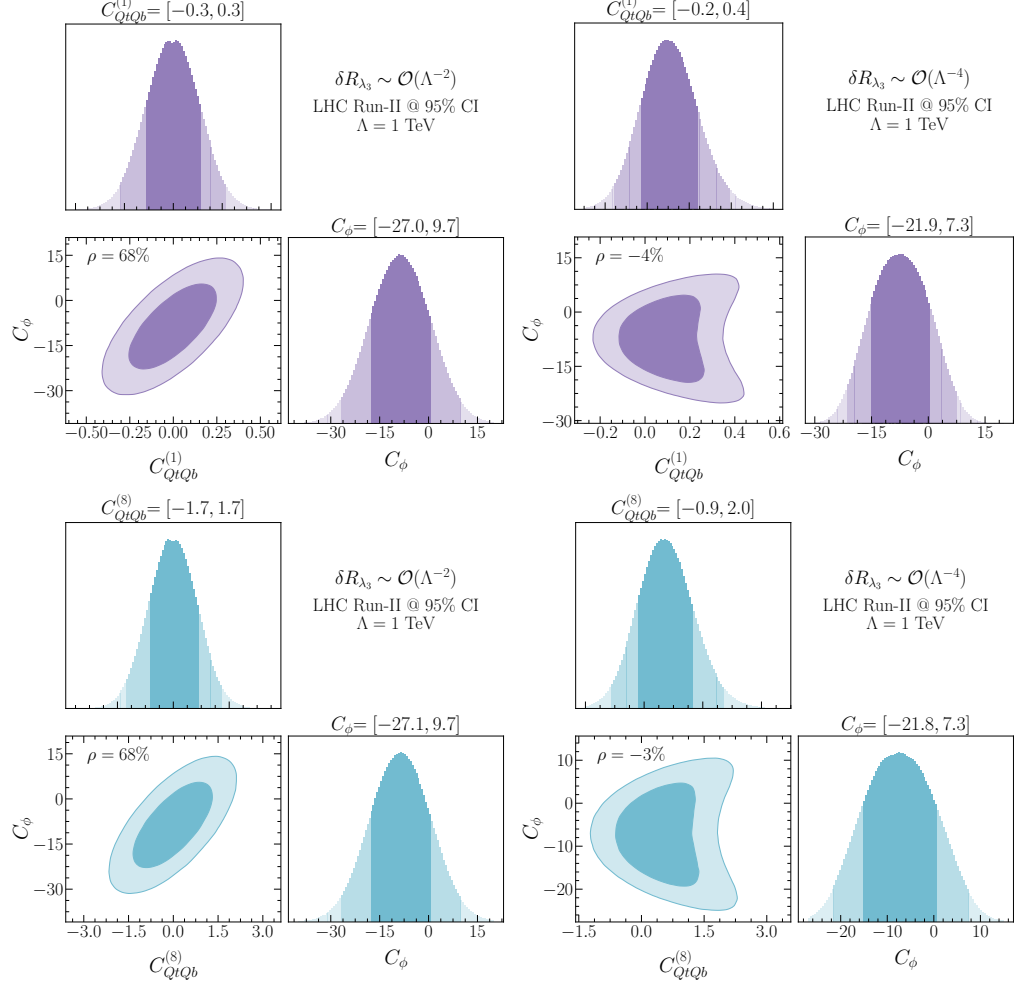


Figure 5.10. The 68% and 95% highest density posterior contours of the posterior distribution of C_ϕ with $C_{Q_t}^{(1)}$ (up) and C_ϕ with $C_{Q_t}^{(8)}$ (down) with the marginalised one-dimensional posteriors for each of the Wilson coefficients and their 68% and 95% HDPIs (shown above in numbers the 95% CI bounds). The limits correspond to values of the Wilson coefficients evaluated at the scale $\Lambda = 1$ TeV. On the left we used the linear scheme in δR_{λ_3} while on the right we keep up to quadratic terms in δR_{λ_3} .



6 Virtual two-loop calculation of Zh production via gluon fusion

As we have seen in the previous sections, Higgs couplings to the weak vector bosons, i.e. Z and W is approaching the precision level. Moreover, the associated Higgs production with these bosons is the first channel used to observe the Higgs decaying into beauty quarks $h \rightarrow b\bar{b}$ by both ATLAS and CMS [122, 123]. Hence, the Vh Higgs production channels are important channels to look for in the future runs of the LHC for better measurement of the VVh coupling as well as Higgs coupling to the beauty quark. As the statistical and systematic uncertainties coming from the experimental setup of the LHC will be eventually reduced in the future runs, due to higher integrated luminosity, upgraded detectors and improved analysis techniques. There is an exigency to reduce theoretical uncertainties emerging from the perturbative calculations of cross-sections. In order to accomplish that, one should include more terms in the perturbative expansion in the couplings, particularly the strong coupling α_s . In this chapter, we are interested in the channel $pp \rightarrow Zh$, which is quark-initiated tree-level process at LO interpreted as **Drell-Yan process** [124, 125]. This process has been computed up to next-to-next-to-leading-order (NNLO) in QCD ($\sim \alpha_s^2$), and at next-to-leading-order (NLO) in the EW interactions ($\sim \alpha^2$) [126].

Despite arising for the first time at NNLO in perturbation theory to the partonic cross-section, the gluon fusion channel $gg \rightarrow Zh$ has a non-negligible contribution to the hadronic cross-section $pp \rightarrow Zh$, which could reach $> 16\%$ of the total cross-section contribution at 14 TeV [48], see Figure 6.1. The contribution becomes more significant when looking at large invariant mass bins in the differential cross-section. This is due to the significant abundance of gluons at the LHC for large energy fraction Q as well as the extra enhancement coming from the top quark initiated contribution near the $t\bar{t}$ threshold [127]. The gluon fusion channel has a higher scale uncertainties than the quark induced one, as one can see from the uncertainty band of Figure 6.1 predominantly coming from the gluon fusion part σ_{gg} . With that in mind, and the absence of gluon fusion channel for Wh channel, the Zh channel has higher theoretical uncertainties. This further motivates NLO calculation of the $gg \rightarrow Zh$ channel to higher orders in perturbation theory, such that these uncertainties get reduced. Facilitating the precision measurement of the Zh channel at the future LHC runs, which in turn provides better constraints on several observables, such as sign and magnitude of the top Yukawa coupling, dipole operators [128]. Additionally, this channel can receive contributions from new particles

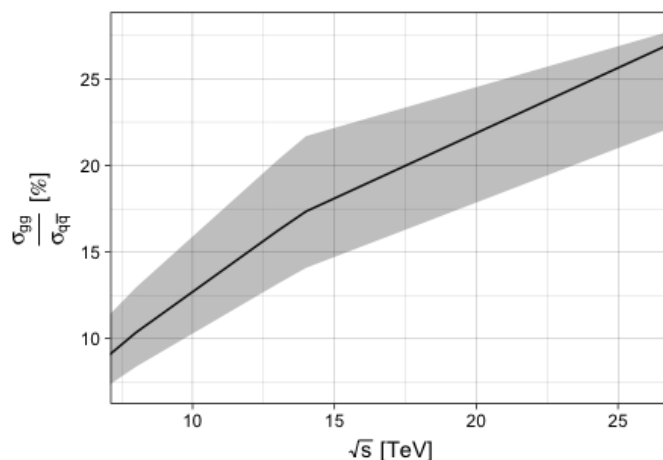


Figure 6.1. The ratio of the LO gluon fusion production cross-section $gg \rightarrow Zh$ (σ_{gg}) with respect to the NLO Drell-Yan process $q\bar{q} \rightarrow Zh$ cross-section ($\sigma_{q\bar{q}}$) at a pp collider with centre-of-mass energy \sqrt{s} . The error band captures the total theoretical uncertainties on both cross-sections dominated by σ_{gg} .

[129], particularly at the large invariant-mass region where the gluon fusion contribution becomes more important. Therefore, better understanding of the SM prediction of the Zh gluon fusion channel is crucial for both the SM precision measurements of Higgs production within the SM and for testing NP in this channel, e.g. new vector-like leptons.

The leading order (LO) contribution to the $gg \rightarrow Zh$ amplitude, given by one-loop diagrams, was computed exactly in refs.[130, 131]. However, for the NLO, the virtual corrections contain multi-scale two-loop integrals some of which are still not known analytically (for the box diagram). The first computation of the NLO terms has been done by [132] using an asymptotic expansion in the limit $m_t \rightarrow \infty$ and $m_b = 0$, and pointed to a K -factor of about ~ 2 . Later, the computation has been improved via soft gluon resummation, and including NLL terms found in ref.[133], the NLL terms has been matched to the fixed NLO computation of [132]. Top quark mass effects to the $gg \rightarrow Zh$ process were first implemented using a combination of large- m_t expansion (LME) and Padé approximants [134]. A data-driven approach to extract the gluon fusion dominated non-Drell-Yan part of Zh production using the known relation between Wh and Zh associated production when only the Drell-Yan component of the two processes is considered has been investigated in ref.[135]. The differential distributions of $gg \rightarrow Zh$ at NLO was studied in ref.[136] via LO matrix element matching.

More recent studies of the NLO virtual corrections to this process were based on the high-energy (HE) expansion improved by Padé approximants with the LME, which

extended the validity range of the HE expansion [137]. However, this expansion is only valid for in the invariant mass region $\sqrt{\hat{s}} \gtrsim 750 \text{ GeV}$ and $\sqrt{\hat{s}} \lesssim 350 \text{ GeV}$, which only covers $\sim 32\%$ of the hadronic cross section. Additionally, numerical computation of the two-loop virtual corrections, though implemented exactly in [138], are rather slow for practical use in MC simulations. This highlights the importance of an analytical method that can cover the remaining region of the cross-section and can be merged with the HE expansion via Padé approximants. Fortunately, the two-loop corrections to the triangle diagrams can be computed exactly. And the loop integrals appearing in the box correction having no analytic expression can be expanded in small Z (or Higgs) transverse momentum, p_T . This method was first used for Higgs pair production in [139], to compute the NLO virtual corrections to the box diagrams in the forward kinematics. In this chapter, I discuss the method and results of the two-loop calculation of the triangle and p_T expansion of Zh process published in [140].

This chapter is structured as follows : In [section 6.1](#) contains the general notation we have used for the gluon fusion Zh process calculation. Then, in [subsection 6.1.1](#) the transverse momentum expansion method is discussed. Calculation of the LO form-factors in the transverse momentum expansion is illustrated in [section 6.2](#) as a proof of concept for the p_T -expansion technique. Outline of the two-loop calculation is discussed in [section 6.3](#). Finally, in [section 6.4](#), the results of our calculation are shown with concluding remarks at the end.

6.1 General notation

The amplitude $g_a^\mu(p_1)g_b^\nu(p_2) \rightarrow Z^\rho(p_3)h(p_4)$ can be written as

$$\mathcal{A} = i\sqrt{2}\frac{m_Z G_F \frac{\alpha_s^0}{4\pi}(\mu_R)}{\pi} \delta_{ab} \epsilon_\mu^a(p_1) \epsilon_\nu^b(p_2) \epsilon_\rho(p_3) \hat{\mathcal{A}}^{\mu\nu\rho}(p_1, p_2, p_3), \quad (6.1)$$

$$\hat{\mathcal{A}}^{\mu\nu\rho}(p_1, p_2, p_3) = \sum_{i=1}^6 \mathcal{P}_i^{\mu\nu\rho}(p_1, p_2, p_3) \mathcal{A}_i(\hat{s}, \hat{t}, \hat{u}, m_t, m_h, m_Z), \quad (6.2)$$

where μ_R is the renormalisation scale and $\epsilon_\mu^a(p_1)\epsilon_\nu^b(p_2)\epsilon_\rho(p_3)$ are the polarization vectors of the gluons and the Z boson, respectively. It is possible to decompose the amplitude into a maximum of 6 Lorentz structures encapsulated by the tensors $\mathcal{P}_i^{\mu\nu\rho}$. Due to the presence of the γ_5 these projectors are proportional to the Levi-Civita total anti-symmetric tensor $\epsilon^{\alpha\beta\gamma\delta}$. One can choose to an orthogonal basis explicitly shown in [section A.1](#), such that

$$\mathcal{P}_i^{\mu\nu\rho} \mathcal{P}_j{}_{\mu\nu\rho} = 0, \quad \text{for } i \neq j \quad (6.3)$$

By this choice one obtains unique form factors corresponding to each projector

$$\mathcal{A}_i(\hat{s}, \hat{t}, \hat{u}, m_t, m_h, m_Z), \quad (6.4)$$

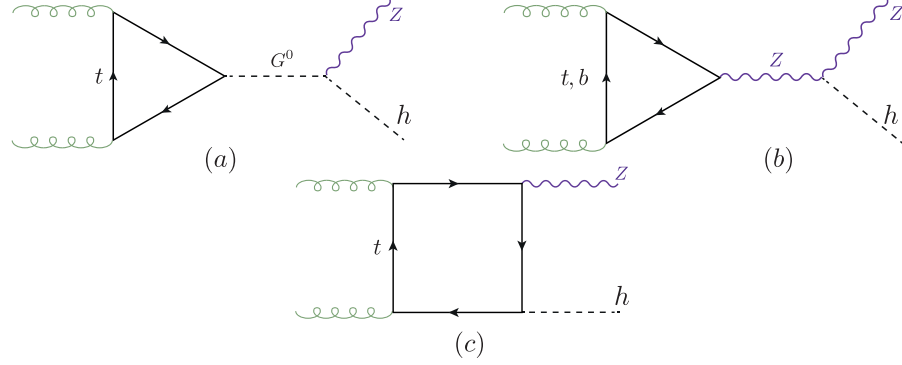


Figure 6.2. Feynman diagrams type for the LO $gg \rightarrow Zh$ process. The triangle diagrams in a general ξ gauge involve Z and the neutral Goldstone G^0 propagators.

that are multivariate complex functions of the top (m_t), Higgs (m_h) and Z (m_Z) bosons masses, and of the partonic Mandelstam variables

$$\hat{s} = (p_1 + p_2)^2, \quad \hat{t} = (p_1 + p_3)^2, \quad \hat{u} = (p_2 + p_3)^2, \quad (6.5)$$

where $\hat{s} + \hat{t} + \hat{u} = m_Z^2 + m_h^2$ and all the momenta are considered to be incoming. The form-factors \mathcal{A}_i can be perturbatively expanded in orders of α_s ,

$$\mathcal{A}_i = \sum_{k=0} \left(\frac{\alpha_s}{\pi} \right)^k \mathcal{A}_i^{(k)} \quad (6.6)$$

Where $\mathcal{A}_i^{(0)}$ and $\mathcal{A}_i^{(1)}$ are the LO and NLO terms, respectively. Using Fermi's Golden Rule, we can write the Born partonic cross-section as

$$\hat{\sigma}^{(0)}(\hat{s}) = \frac{m_Z^2 G_F^2 \alpha_s(\mu_R)^2}{64 \hat{s}^2 (2\pi)^3} \int_{\hat{t}^-}^{\hat{t}^+} d\hat{t} \sum_i |\mathcal{A}_i^{(0)}|^2, \quad (6.7)$$

where $\hat{t}^\pm = [-\hat{s} + m_h^2 + m_Z^2 \pm \sqrt{(\hat{s} - m_h^2 - m_Z^2)^2 - 4m_h^2 m_Z^2}]/2$.

The LO has two sets of diagrams, the triangle, and box diagrams shown in Figure 6.2. In (a), the triangle diagrams contains a neutral Goldstone boson G^0 , instead in (b) the Z boson is mediated. The interplay between these two diagram types depends on the ξ gauge. Moreover, the Z boson is strictly off-shell, due to Furry's theorem. In the Landau gauge the Z -mediated diagrams will also vanish, this can be seen by considering the subamplitude ggZ^* which in the Landau gauge can be related to the decay of a massive vector boson with mass $\sqrt{\hat{s}}$ into two massless ones, a process that is forbidden by the

Landau-Yang theorem [141, 142]. The triangle diagrams are also proportional to the mass difference between the up and down type quarks. In this calculation, the first and second generation quarks are assumed to be massless, as well as the b quark, hence light quarks loops do not contribute to this process. The same would apply to the box diagrams (c), as they are proportional to the quark Yukawa coupling, and vanish in the massless quarks case. Moreover, triangle diagrams with b -quark loops contribute to $\sim 1\%$ of the total amplitude, computed in the limit $m_b \rightarrow 0$.

6.1.1 The transverse momentum expansion

Choosing to expand in small p_T of the Z boson, the first step is expressing p_T in terms of the Mandelstam variables and masses

$$p_T^2 = \frac{\hat{t}\hat{u} - m_Z^2 m_h^2}{\hat{s}}. \quad (6.8)$$

From eq.(6.8), together with the relation between the Mandelstam variables, one finds

$$p_T^2 + \frac{m_h^2 + m_Z^2}{2} \leq \frac{\hat{s}}{4} + \frac{\Delta_m^2}{\hat{s}}, \quad (6.9)$$

where $\Delta_m = (m_h^2 - m_Z^2)/2$. Eq.(6.9) implies $p_T^2/\hat{s} < 1$ that, together with the kinematical constraints $m_h^2/\hat{s} < 1$ and $m_Z^2/\hat{s} < 1$. With these relations in mind, one can expand the amplitudes in terms of small p_T^2/\hat{s} , m_h^2/\hat{s} and m_Z^2/\hat{s} , which is technically valid throughout the whole phase space, contrary to the LME and HE limits. The caveat for this expansion is that, the amplitude does not depend on p_T explicitly. Instead, one would expand in the reduced Mandelstam variables $t'/s' \ll 1$ or $u'/s' \ll 1$, defined as

$$s' = p_1 \cdot p_2 = \frac{\hat{s}}{2}, \quad t' = p_1 \cdot p_3 = \frac{\hat{t} - m_Z^2}{2}, \quad u' = p_2 \cdot p_3 = \frac{\hat{u} - m_Z^2}{2} \quad (6.10)$$

and satisfy

$$s' + t' + u' = \Delta_m. \quad (6.11)$$

The choice of the expansion parameter t' or u' depends whether one expands in the forward or backwards kinematics. Because the process $gg \rightarrow Zh$, has two particles in the final states with different masses, the amplitude is not symmetric under the their exchange. One therefore cannot compute the cross-section by integrating only the forward-expanded amplitude [140], contrary what has been done for the Higgs pair [139]. In order to overcome this issue, one could further examine the projectors in section A.1 and observe that they can be split into symmetric and anti-symmetric parts with respect to the exchange $t' \leftrightarrow u'$. Then, expand the symmetric part in the forward kinematics, like the Higgs pair case. As for the anti-symmetric part, the antisymmetric factor is simply extracted by multiplying the form-factors by $1/(\hat{t} - \hat{u})$, written as $1/(2s' - 4t' - 2\Delta_m)$,

then perform the expansion in the forward kinematics and finally multiply back by $(\hat{t}-\hat{u})$.

In order to implement the p_T -expansion at the Feynman diagrams level we start by splitting the momenta into longitudinal and transverse with respect to the beam direction, by introducing the vector [139],

$$r^\mu = p_1^\mu + p_3^\mu, \quad (6.12)$$

which satisfies

$$r^2 = \hat{t}, \quad r \cdot p_1 = \frac{\hat{t} - m_Z^2}{2}, \quad r \cdot p_2 = -\frac{\hat{t} - m_h^2}{2}, \quad (6.13)$$

and hence can be also written as

$$r^\mu = -\frac{\hat{t} - m_h^2}{\hat{s}} p_1^\mu + \frac{\hat{t} - m_Z^2}{\hat{s}} p_2^\mu + r_\perp^\mu = \frac{t'}{s'} (p_2^\mu - p_1^\mu) - \frac{\Delta_m}{s'} p_1^\mu + r_\perp^\mu, \quad (6.14)$$

where

$$r_\perp^2 = -p_T^2. \quad (6.15)$$

substituting the definition of p_T from eq.(6.8) one obtains

$$t' = -\frac{s'}{2} \left\{ 1 - \frac{\Delta_m}{s'} \pm \sqrt{\left(1 - \frac{\Delta_m}{s'}\right)^2 - 2\frac{p_T^2 + m_Z^2}{s'}} \right\} \quad (6.16)$$

implying that the expansion in small p_T (the minus sign case in eq.(6.16)) can be realized at the level of Feynman diagrams, by expanding the propagators in terms of the vector r^μ around $r^\mu \sim 0$ or, equivalently, $p_3^\mu \sim -p_1^\mu$, see eq.(6.14).

6.2 Born cross-section in the p_T -expansion

As a baseline test for the validity and convergence behaviour of the p_T expansion we start by computing the LO amplitude, and consequently the Born partonic cross-section in the p_T expansion then compare it with the exact results found in [130, 131].

Starting by defining the one-loop functions appearing in the similar calculation of the Born cross-section for $gg \rightarrow hh$ in the same expansion carried out in ref. [139]

$$B_0[\hat{s}, m_t^2, m_t^2] \equiv B_0^+, \quad B_0[-\hat{s}, m_t^2, m_t^2] \equiv B_0^-, \quad (6.17)$$

$$C_0[0, 0, \hat{s}, m_t^2, m_t^2, m_t^2] \equiv C_0^+, \quad C_0[0, 0, -\hat{s}, m_t^2, m_t^2, m_t^2] \equiv C_0^- \quad (6.18)$$

$$B_0[q^2, m_1^2, m_2^2] = \frac{1}{i\pi^2} \int \frac{d^n k}{\mu^{n-4}} \frac{1}{(k^2 - m_1^2)((k+q)^2 - m_2^2)}, \quad (6.19)$$

$$C_0[q_a^2, q_b^2, (q_a + q_b)^2, m_1^2, m_2^2, m_3^2] = \frac{1}{i\pi^2} \int \frac{d^d k}{\mu^{d-4}} \frac{1}{[k^2 - m_1^2][(k + q_a)^2 - m_2^2][(k - q_b)^2 - m_3^2]} \quad (6.20)$$

are the Passarino-Veltman functions [143], with d the dimension of spacetime and μ the 't Hooft mass. There are only two non-vanishing form-factors at LO, one is symmetric \mathcal{A}_2 , and the other is antisymmetric \mathcal{A}_6 , in the p_T -expansion, these form-factors are give by, up to order $\mathcal{O}(p_T^2)$

$$\begin{aligned} \mathcal{A}_2^{(0,\Delta)} &= -\frac{p_T}{\sqrt{2}(m_Z^2 + p_T^2)}(\hat{s} - \Delta_m) m_t^2 C_0^+, \\ \mathcal{A}_2^{(0,\Box)} &= \frac{p_T}{\sqrt{2}(m_Z^2 + p_T^2)} \left\{ \begin{aligned} &\left(m_t^2 - m_Z^2 \frac{\hat{s} - 6m_t^2}{4\hat{s}} - p_T^2 \frac{12m_t^4 - 16m_t^2 \hat{s} + \hat{s}^2}{12\hat{s}^2} \right) B_0^+ \\ &- \left(m_t^2 - \Delta_m \frac{m_t^2}{(4m_t^2 + \hat{s})} + m_Z^2 \frac{24m_t^4 - 6m_t^2 \hat{s} - \hat{s}^2}{4\hat{s}(4m_t^2 + \hat{s})} - \right. \\ &\quad \left. p_T^2 \frac{48m_t^6 - 68m_t^4 \hat{s} - 4m_t^2 \hat{s}^2 + \hat{s}^3}{12\hat{s}^2(4m_t^2 + \hat{s})} \right) B_0^- \\ &+ \left(2m_t^2 - \Delta_m + m_Z^2 \frac{3m_t^2 - \hat{s}}{\hat{s}} + p_T^2 \frac{3m_t^2 \hat{s} - 2m_t^4}{\hat{s}^2} \right) m_t^2 C_0^- \\ &+ \left(\hat{s} - 2m_t^2 + m_Z^2 \frac{\hat{s} - 3m_t^2}{\hat{s}} + p_T^2 \frac{2m_t^4 - 3m_t^2 \hat{s} + \hat{s}^2}{\hat{s}^2} \right) m_t^2 C_0^+ \\ &+ \log \left(\frac{m_t^2}{\mu^2} \right) \frac{m_t^2}{(4m_t^2 + \hat{s})} \left(\Delta_m + 2m_Z^2 + p_T^2 \frac{2\hat{s} - 2m_t^2}{3\hat{s}} \right) \\ &- \Delta_m \frac{2m_t^2}{(4m_t^2 + \hat{s})} + m_Z^2 \frac{\hat{s} - 12m_t^2}{4(4m_t^2 + \hat{s})} + p_T^2 \frac{8m_t^4 - 2m_t^2 \hat{s} + \hat{s}^2}{4\hat{s}(4m_t^2 + \hat{s})} \end{aligned} \right\}, \end{aligned} \quad (6.22)$$

and

$$\mathcal{A}_6^{(0,\triangle)} = 0, \quad (6.23)$$

$$\begin{aligned} \mathcal{A}_6^{(0,\square)} &= \frac{\hat{t} - \hat{u}}{\hat{s}^2} p_T \left[\frac{m_t^2}{2} (B_0^- - B_0^+) - \frac{\hat{s}}{4} \right. \\ &\quad \left. - \frac{2m_t^2 + \hat{s}}{2} m_t^2 C_0^- + \frac{2m_t^2 - \hat{s}}{2} m_t^2 C_0^+ \right], \end{aligned} \quad (6.24)$$

where these form-factors were divided into triangle (\triangle) and box (\square) contributions, and B_0 functions are understood as the finite part of the integrals on the right hand side of eq.(6.19).

Using several truncations of the p_T -expansion, and comparing it to the exact LO result, one can see in Figure 6.3 the exact Born partonic LO cross section (red line) as a function of the invariant mass of the Zj system, M_{Zh} , in comparison to the p_T -expansions. For the numerical evaluation of the cross section here and in the following, we used as SM input parameters

$$\begin{aligned} m_Z &= 91.1876 \text{ GeV}, \quad m_h = 125.1 \text{ GeV}, \quad m_t = 173.21 \text{ GeV}, \\ m_b &= 0 \text{ GeV}, \quad G_F = 1.16637 \text{ GeV}^{-2}, \quad \alpha_s(m_Z) = 0.118. \end{aligned}$$

From the ratio plotted in the lower panel of Figure 6.3, we observe that the $\mathcal{O}(p_T^0)$ expansion is in good agreement with the exact result when $M_{Zh} \lesssim 2m_t$. Inclusion of higher order terms up to $\mathcal{O}(p_T^6)$ extended the validity of the expansion to reach $M_{Zh} \lesssim 750 \text{ GeV}$. This is the similar behaviour seen in [139] for Higgs pair. Therefore, one would expect the p_T -expanded two-loop virtual correction to be an accurate approximation with the exact (numerical) result for the region of the invariant mass of $M_{Zh} \sim 700 - 750 \text{ GeV}$. Similar conclusions can be seen more explicitly in Table 6.1, where it is shown that the partonic cross-section at $\mathcal{O}(p_T^4)$ agrees with the full result for $M_{ZH} \lesssim 600 \text{ GeV}$ on the permille level and the agreement further improves when $\mathcal{O}(p_T^6)$ terms are included.

6.3 NLO calculation

The virtual two-loop corrections to $gg \rightarrow Zh$ are shown in Figure 6.4, which involve corrections to the triangle topology in (a) and (b). The corrections to the box topology in (c) and a new topology, denoted by double triangle in (d). Both two-loop corrections to the triangles, and the double triangle diagrams can be computed exactly analytically. However, the two-loop box diagrams contain master-integrals (MI's) that have no analytic solutions, so far. The two-loop box diagrams will be computed in the p_T -expansion.

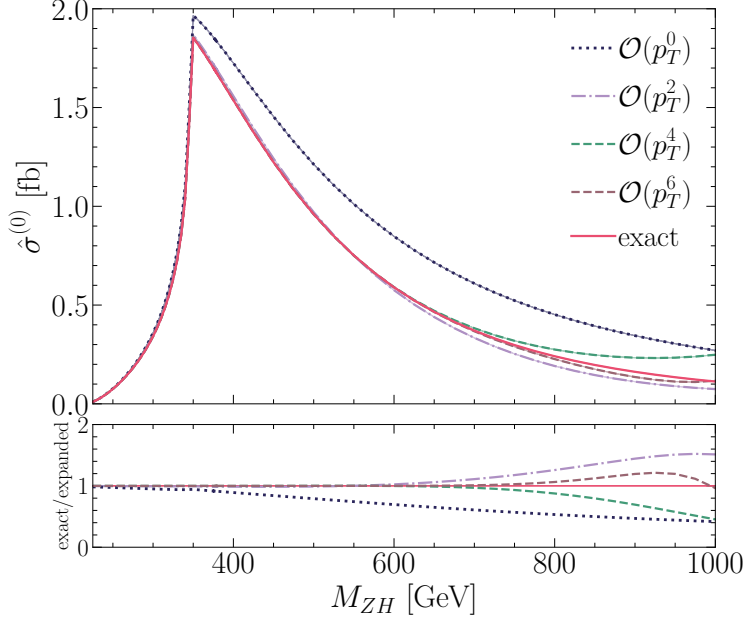


Figure 6.3. The Born partonic cross-section as a function of the invariant mass M_{Zh} . The exact (red line) is plotted together with results at different orders in the p_T -expansion (dashed lines). In the bottom part, the ratio of the full result over the p_T -expanded one at various orders is shown. This plot has been already published in [140]

6.3.1 Renormalisation

The two-loop corrections to the triangle and box diagrams contain both UV and IR divergences. The first emerges from UV divergent sub-diagrams, such as top mass renormalisation and QCD vertex correction. While the IR divergences come from massless loops. In order to remove these divergences, one introduces adequate counter-terms. On the other hand, the double triangle is both UV and IR finite.

We start by the gluon wavefunction renormalisation of the incoming gluons (external legs) such that the amplitude is renormalised by $Z_A^{1/2}$ for each gluon.

$$Z_A = 1 + \frac{\alpha_s^0}{4\pi} \frac{2}{3\epsilon} \left(\frac{\mu_R^2}{m_t^2} \right)^\epsilon. \quad (6.25)$$

The on-shell scheme for the top mass renormalisation has been used, in which the bare mass is replaced by the renormalised one $m_0 = Z_m m$ in the propagators this gives the

M_{Zh} [GeV]	$\mathcal{O}(p_T^0)$	$\mathcal{O}(p_T^2)$	$\mathcal{O}(p_T^4)$	$\mathcal{O}(p_T^6)$	full
300	0.3547	0.3393	0.3373	0.3371	0.3371
350	1.9385	1.8413	1.8292	1.8279	1.8278
400	1.6990	1.5347	1.5161	1.5143	1.5142
600	0.8328	0.5653	0.5804	0.5792	0.5794
750	0.5129	0.2482	0.3129	0.2841	0.2919

Table 6.1. The partonic cross section $\hat{\sigma}^{(0)}$ at various orders in p_T and the full computation for several values of M_{Zh} . This table has been already published in [140].

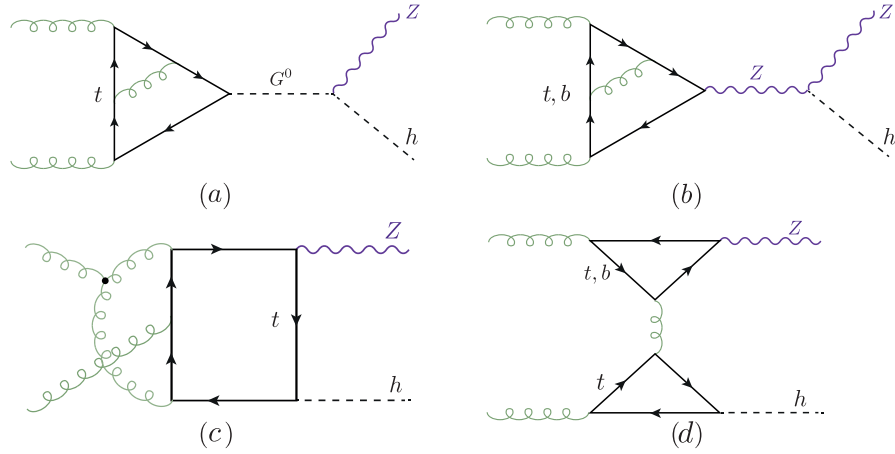


Figure 6.4. Feynman diagrams types for the virtual NLO corrections to the $gg \rightarrow Zh$ process.

$\overline{\text{MS}}$ renormalised mass.

$$Z_m = 1 + C_F \frac{3}{\epsilon}. \quad (6.26)$$

In order to convert the mass definition to the on-shell scheme we add the finite renormalisation term

$$Z_m^{OS} = 1 - 2C_F, \quad (6.27)$$

here $C_F = (N_c^2 - 1)/2N_c$ is one of the two Casimir invariants of QCD along with $C_A = N_c$. The $q\bar{q}g$ vertex correction involves a renormalisation of the strong couplings constant α_s which is done via replacing the bare constant α_s^0 with the renormalised one, hence it becomes $\alpha_s^0 = \frac{\mu_R^{2\epsilon}}{\hat{s}_\epsilon} Z_{\alpha_s} \alpha_s$, where

$$Z_{\alpha_s} = 1 - \frac{\alpha_s}{4\pi} \frac{1}{\epsilon} \left(\beta_0 - \frac{2}{3} \right) \left(\frac{\mu_R^2}{m_t^2} \right)^\epsilon, \quad (6.28)$$

and the constant $\beta_0 = \frac{11}{3}C_A - \frac{2}{3}N_f$, where N_f is the number of “active” flavours. The 5-flavour scheme $N_f = 5$ is adopted here.

The loop integrals were evaluated via dimensional regularisation in $d = 4 - 2\epsilon$ dimensions. Which requires some caution when γ_5 is present in the amplitude. We let γ_5 naively anti-commute with all d -dimensional γ_μ ’s and then correct that with the finite renormalisation constant known as **Larin counter-term** [144]

$$Z_5 = 1 - 2C_F. \quad (6.29)$$

The renormalised amplitude is written as

$$\mathcal{M}(\alpha_s, m, \mu_R) = Z_A \mathcal{M}(\alpha_s^0, m^0). \quad (6.30)$$

Putting all the above substitutions together, we get the renormalised two-loop form-factor:

$$(\mathcal{A}^{(1)})^R = \mathcal{A}^{(1)} - \mathcal{A}_{UV}^{(0)} - \mathcal{A}_{UV,m}^{(0)} + \mathcal{A}_{\text{Larin}}^{(0)} \quad (6.31)$$

$$\mathcal{A}_{UV}^{(0)} = \frac{\alpha_s}{4\pi} \frac{\beta_0}{\epsilon} \left(\frac{\mu_R^2}{\hat{s}} \right)^{-\epsilon} \mathcal{A}^{(0)}.$$

$$\mathcal{A}_{UV,m}^{(0)} = \frac{\alpha_s}{4\pi} \left(\frac{3}{\epsilon} - 2 \right) C_F \left(\frac{\mu_R^2}{\hat{s}} \right)^{-\epsilon} m^0 \partial_m \mathcal{A}^{(0)}. \quad (6.32)$$

$$\mathcal{A}_{\text{Larin}}^{(0)} = -\frac{\alpha_s}{4\pi} C_F \mathcal{A}^{(0)}.$$

The following IR-counter-term is used in order to cancel the IR divergences.

$$\mathcal{A}_{IR}^{(0)} = \frac{e^{\gamma_E \epsilon}}{\Gamma(1-\epsilon)} \frac{\alpha_s}{4\pi} \left(\frac{\beta_0}{\epsilon} + \frac{C_A}{\epsilon^2} \right) \left(\frac{\mu_R^2}{\hat{s}} \right)^{2\epsilon} \mathcal{A}^{(0)} \quad (6.33)$$

The one-loop form-factors, need to be expanded up to order $\mathcal{O}(\epsilon^2)$, for the UV and IR counter-terms.

6.3.2 Calculation of the exact virtual corrections

The two-loop calculations of the triangle digrams involves the diagrams of with virtual Z^* and G^0 , depending on the gauge of choice. Observations found in ref.[132] shows that due to Landau-Yang theorem in the Landau gauge the diagrams with the Z^* exchange vanishes. Therefore, the part of the top triangle diagrams can be obtained from the decay amplitude of a pseudoscalar boson into two gluons which is known in the literature in the full mass dependence up to NLO terms [145, 146]. On the contrary, in the unitary gauge, the NLO calculation needs to be done with the Z^* exchange diagrams only. The calculations result in apparently different Lorentz structures, that are linked via the Schouten identity

$$q^\alpha \epsilon^{\beta\gamma\delta\phi} + q^\beta \epsilon^{\gamma\delta\phi\alpha} + q^\gamma \epsilon^{\delta\phi\alpha\beta} + q^\delta \epsilon^{\phi\alpha\beta\gamma} + q^\phi \epsilon^{\alpha\beta\gamma\delta} = 0 \quad (6.34)$$

A cross-check has been preformed in order to ensure that the NLO calculation introduces no new Lorentz structures, and gives the same result in a general R_ξ gauge as the results in [145, 146]. The two-loop calculation has been carried out in R_ξ gauge. The amplitudes have been automatically generated by **FeynArts** [84] and contracted with the projectors as defined in section A.1 using **FeynCalc** [147, 148] and **Package X** [149] and in-house Mathematica routines. The two-loop integrals were reduced to a set of master integrals MI, illustrated graphically in Figure 6.5 using **Kira** [150]. These MI's are either products of one-loop functions (a)-(c), (e),(f),(h) and (l) or can be found in the literature [146, 151]. Their implementation in our calculation has been validated numerically using **SecDec** [152, 153]. The virtual correction for the triangle diagrams can be separated according to their colour factors into

$$\mathcal{A}^{(1)} = C_F \mathcal{A}_{CF}^{(1)} + C_A \mathcal{A}_{CA}^{(1)}, \quad (6.35)$$

The C_A part contains a double pole $\mathcal{O}(1/\epsilon^2)$ and a single pole $\mathcal{O}(1/\epsilon)$, both coming from the IR divergence. Whilst the C_F part contains a UV divergent pole that needs to be cured via mass renormalisation. The poles do not have a dependence on the renormalisation scale μ_R . However, there is a dependence on that scale in the finite part, as well. No new Lorentz structures appeared, and the final result in R_ξ matched the one found in [145, 146] for the Landau gauge. The explicit results are shown in section A.2

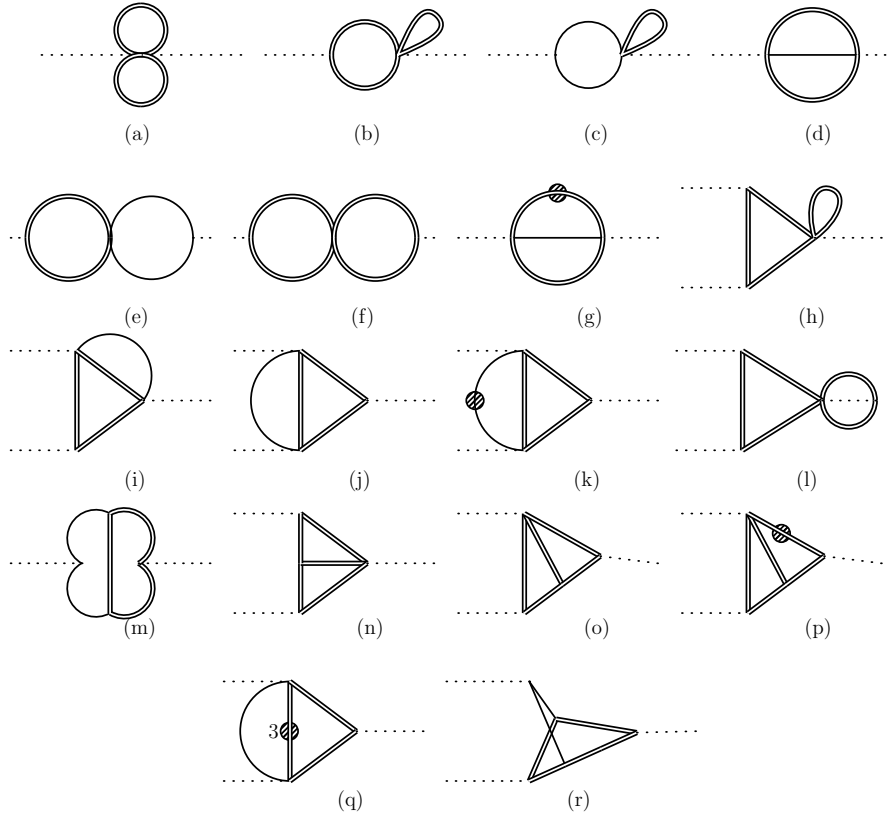


Figure 6.5. The list of two-loop master integrals (MI's) resulting from the reduction of the two-loop triangle corrections, and the product of one-loop MI's appearing in this list also appear in the calculation of the double-triangle diagrams. A single line denotes a massless propagator, while a double line denotes a massive one. The dot denotes a squared propagator, unless the number of the exponent is indicated, here only 3 appears in diagram (q).

The calculation of the double triangle diagrams (d) of Figure 6.4 is fairly straightforward, all of the integrals can be rewritten in terms of products of one-loop functions. All of the Lorentz structures appear in the double triangle except for \mathcal{P}_6 , analogous to the triangle case. The explicit forms of form-factors corresponding to these structures are presented in section A.2. Although we write the amplitude using a different tensorial structure with respect to ref.[137] we have checked, using the relations between the two tensorial structures reported in section A.1, that our result is in agreement with the one presented in ref.[134].

6.3.3 Calculation of the p_T -expanded virtual corrections

The two-loop triangle diagrams can also be interpreted as an expansion in p_T , but this expansion terminates at $\mathcal{O}(p_T^2)$, rather being an infinite series. Hence, in this section we concentrate on the two-loop box diagrams p_T -expansion¹.

Similar to the two-loop triangle diagrams, the box diagrams amplitudes were generated projected through the same pipeline. After the contraction of the epsilon tensors the diagrams were expanded as described in subsection 6.1.1, keeping only $\mathcal{O}(p_T^4)$ terms. They were reduced to MI's using FIRE [154] and LiteRed [155]. The resulting MI's were identical to the one for Higgs pair production [139]. Nearly all of them are expressed in terms of generalised harmonic polylogarithms with the exception of two elliptic integrals [156, 157]. The renormalisation and IR pole subtraction procedure was carried out like prescribed subsection 6.3.1.

As a control, the two-loop box diagrams were also computed in the LME up to $\mathcal{O}(1/m_t^6)$. Since this expansion should be included within the p_T -expansion. We have retained the LME analytic expression by further expanding the p_T -expanded amplitude in small \hat{s}/m_t^2 . Providing an additional cross-check for the validity of the p_T -expansion.

6.4 Results and conclusions

The virtual corrections to the gluon fusion Zh production have been implemented in a FORTRAN code using handyG [158], for the evaluation of generalised harmonic polylogarithms, Chaplin [159] for the harmonic polylogarithms appearing in the triangle two-loop functions while the elliptic integrals are evaluated using the routines of ref.[157]. Since the result is analytic, the code is significantly faster than the numerical evaluation of the two-loop amplitude [138], with evaluation time of ca. 0.5 min per one phase space point on a personal laptop.

In order to facilitate the comparison of our results with the ones presented in the liter-

¹The calculation of the box diagrams has been done mainly by my collaborators, the co-authors of [140]

\hat{s}/m_t^2	\hat{t}/m_t^2	ref.[138]	$\mathcal{O}(p_T^6)$
1.707133657190554	-0.441203767016323	35.429092(6)	35.430479
3.876056604162662	-1.616287256345735	4339.045(1)	4340.754
4.130574250302561	-1.750372271104745	6912.361(3)	6915.797
4.130574250302561	-2.595461551488002	6981.09(2)	6984.20

Table 6.2. Comparison of $\mathcal{V}_{fin}4/(\alpha_s^2\alpha^2)$ with the numerical results of ref.[138]. This plot has been already published in [140].

ature, we define the finite part of the virtual corrections as in ref.[137]²

$$\begin{aligned} \mathcal{V}_{fin} = & \frac{G_F^2 m_Z^2}{16} \left(\frac{\alpha_s}{\pi} \right)^2 \left[\sum_i |\mathcal{A}_i^{(0)}|^2 \frac{C_A}{2} \left(\pi^2 - \log^2 \left(\frac{\mu_R^2}{\hat{s}} \right) \right) \right. \\ & \left. + 2 \sum_i \text{Re} \left[\mathcal{A}_i^{(0)} \left(\mathcal{A}_i^{(1)} \right)^* \right] \right] \end{aligned} \quad (6.36)$$

and in the numerical evaluation of eq.(6.36) we fixed $\mu_R = \sqrt{\hat{s}}$. Triangle and LME box topologies were validated against the results of refs.[134, 137] finding perfect agreement at the form-factor level, i.e. $\mathcal{A}_i^{(1)}$.

The virtual part of the partonic cross-section from the finite part of the virtual corrections in eq.(6.36) is defined by

$$\Delta\hat{\sigma}_{virt} = \int_{\hat{t}^-}^{\hat{t}^+} d\hat{t} \frac{\alpha_s}{16\pi^2} \frac{1}{\hat{s}^2} \mathcal{V}_{fin} \quad (6.37)$$

This function is used to confront p_T -expanded results. Starting with low M_{Zh} we have compared the p_T -expanded with the LME \mathcal{V}_{fin} , finding a good numerical agreement. It is important to note that, at the same order in the expansion, the p_T -expanded terms are more accurate than the LME ones, although computationally more demanding. Additional checks have been done using the numerical evaluation of the NLO amplitude by [138], where they have evaluated the exact two-loop MI's using `pySecDec` [160, 161]. Table 6.2 shows a comparison between our p_T -expanded $\mathcal{V}_{fin}4/(\frac{\alpha_s^0}{4\pi} \alpha^2)$ versus the exact numerical result of [138] for several phase space points. As can be seen from the table the relative difference between the two results is less than half a permille.

In Figure 6.6, the dashed lines show the different orders of the expansion. For all parts of the matrix elements the best results available, i.e. both $\mathcal{A}^{(0)}$ were used and the double-triangle contribution are evaluated exactly, while for $\mathcal{A}^{(1)}$ we use the various orders in the p_T -expansion. For comparison, the results are shown where $\mathcal{A}^{(1)}$ is replaced

²The definition of the matrix elements here differs by a factor of $\frac{1}{s}$ from ref.[137], cf. also section A.1.

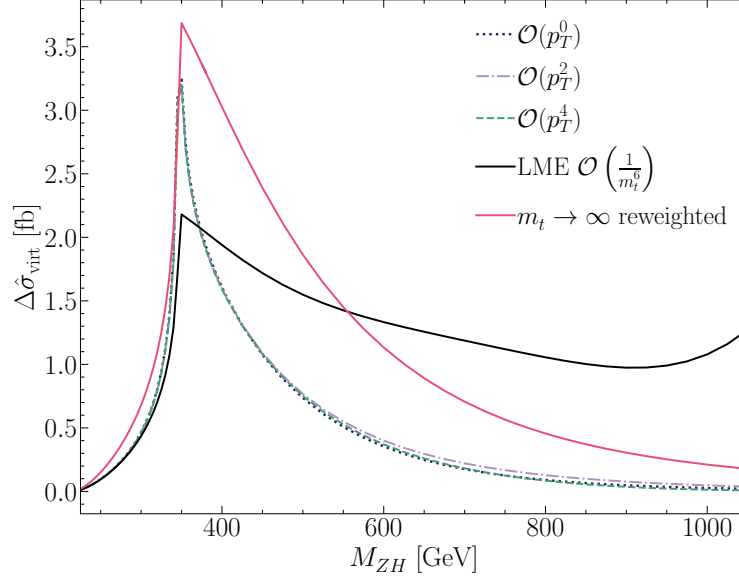


Figure 6.6. $\Delta\hat{\sigma}_{virt}$ defined by eq.(6.37), shown as a function of M_{ZH} . The various orders of the p_T -expansion are plotted as dashed lines, while the black and red continuous lines stand for the LME and reweighted $m_t \rightarrow \infty$ results, respectively. This plot has been already published in [140].

by the one computed in LME up to $\mathcal{O}(1/m_t^6)$ (full black line), which as mentioned before is valid up to $M_{ZhH} < 2m_t$. We observe that within the validity of the LME our results agree well with it. Furthermore, the results in the infinite top mass limit reweighted by the full amplitudes squared can be seen as the full red line in the plot, corresponding to the approach of ref.[132], keeping though the double triangle contribution in full top mass dependence. Differently from the LME line, the $m_t \rightarrow \infty$ reweighted one shows a behaviour, for $M_{Zh} \gtrsim 400$ GeV, similar to the behaviour of the p_T lines. Still, the difference between the reweighted result and the p_T -expanded ones is significant. The p_T -expanded results show very good convergence. The zero order in our expansion agrees extremely well with the higher orders in the expansion, and all the three results are very close up to $M_{Zh} \sim 500$ GeV.

The calculation of the virtual two-loop corrections to the $gg \rightarrow Zh$ is done using exact results for the triangle and double-triangle topologies, and in the p_T -expansion for the box one. The result of the calculation showed that we get the exact same MI's that was found for Higgs pair production [139], mostly these MI's are expressed in terms of generalised harmonic polylogarithms with the exception of two elliptic integrals. Using the LO calculation, we have shown the validity of the p_T -expansion covering the invariant mass interval $M_{Zh} \lesssim 750$ GeV which covers $\sim 98\%$ of the total phase space for 13 – 14

TeV energies.

The p_T -expansion agrees with per mill level with the numerical results found in [138]. However, it allows for fast computation of the amplitude with circa one second per phase space point using a modern laptop with mid-range specifications. Additionally, the integration over the \hat{t} variable in eq.(6.37) converges very well. The flexibility of our analytic results, an application to beyond-the-Standard Model is certainly possible.

Finally, it should be noted that this calculation complements nicely the results obtained in ref.[137] using a high-energy expansion, that according to the authors provides precise results for $p_T \gtrsim 200$ GeV. The merging of the two analyses is going to provide a result that covers the whole phase space, can be easily implemented into a Monte Carlo code using Padé approximants, which is currently a work in progress in [Cite the new paper here-later](#)

Part III

Higgs Pair at Hadron Colliders

7 Overview of Higgs pair production at colliders

The dominant process for Higgs pair production at the LHC (and hadron colliders in general) is the gluon gluon fusion (ggF) via a heavy quark loop Q , mainly the top and beauty quark, with the latter contributing only to about 1%, see figure 7.1. This process

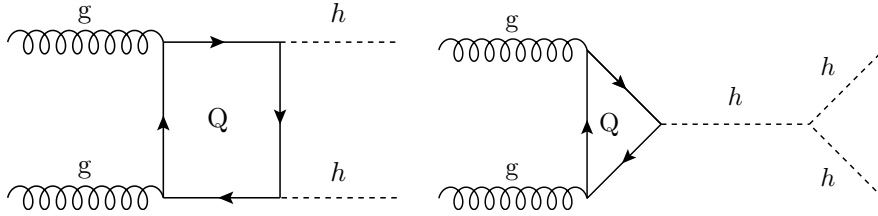


Figure 7.1. Feynman diagrams for the ggF process of Higgs pair production in the SM.

is well-studied at leading order (LO) analytically [162–165]. The next-to-leading QCD order (NLO) was initially computed using infinite top mass limit ($m_t \rightarrow \infty$) using the Higgs effective field theory (HEFT) and implemented in the programme **Hpair** [166]. However, this approximation is not suitable for obtaining distributions, and using numerical methods [167–169] the full NLO results were obtained. In [170], parton shower effects were included in the NLO calculations, allowing the use of the NLO in event generators such as **PYTHIA** and **POWHEG**. Analytical calculations for the NLO corrections using small Higgs transverse momentum $p_{T,h} \rightarrow 0$ yielded a good estimation for the numerical result [139]. The use of Padé approximation obtained also analytical results for the NLO result and a description for the three-loop (NNLO) form factors [171]. The NNLO cross section with top mass effects has been computed numerically in [172].

In this work, we have calculated the $\sqrt{s} = 14$ TeV LO ggF inclusive cross-section and distributions with modified light Yukawa couplings by including the light quark loops and the coupling $hhq\bar{q}$ described in the last diagram in figure 7.2. The calculation was carried out using a FORTRAN code utilising the **VEGAS** integration algorithm, and **NNPDF30** parton distribution functions (PDF's) [173] implemented via **LHAPDF-6** package [174]. For the loop integrals (see Appendix), we have used the **COLLIER** library [175] for regularisation of the IR divergent light quark loops, that were assumed massless. A K -factor, for the NNLO correction were used according to the Higgs cross

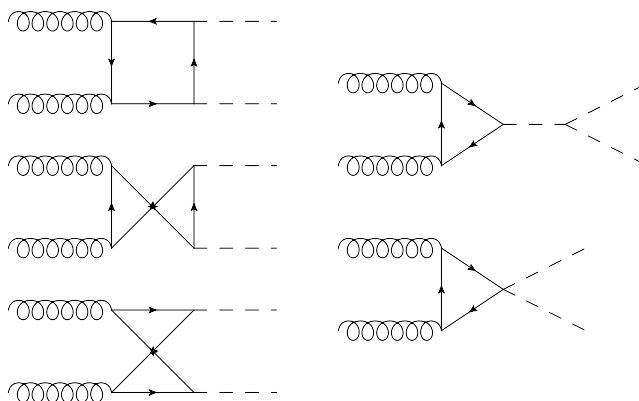


Figure 7.2. The one-loop diagrams calculated in the ggF with modified Yukawa couplings

section working group recommended values [176, 177]:

$$K = \frac{\sigma_{NNLO}}{\sigma_{LO}}, \quad K_{14\text{TeV}} \approx 1.71. \quad (7.1)$$

Since the cross-section is not expected to change a lot by changing the light Yukawa couplings, we use the same NNLO K-factor for all values of the scalings. The renormalisation μ_R and factorisation μ_F scales of the α_s and PDF running are set to $\mu_0 = 0.5 M_{hh}$, and $\alpha_s(M_Z) = 0.118$. In our calculations, we did not consider the quark mass running, as the later will be accounted for in the K-factor.

Theoretical systematic uncertainties

There are three main sources of theoretical *systematic* uncertainties:

1. Scale uncertainty: coming from the arbitrariness of scales choice.
2. PDF uncertainties : coming from the uncertainty in the PDF fitting and model.
3. α_s running uncertainty: originating from the initial value (i.e. $\alpha_s(M_Z)$).

In order to compute these uncertainties, we follow the recommendations of the Higgs cross-section working group for the value and uncertainty of α_s

$$\alpha_s(M_Z) = 0.1180 \pm 0.0015, \quad (7.2)$$

and the methods described in [178, 179]. for PDF and α_s uncertainties. In order to calculate the scale uncertainties, the cross-section was computed with different μ_R and

	σ [fb]	Scale [fb]	PDF+ α_s [fb]	Total [fb]
SM HEFT (LO)	18.10	—	—	—
SM running mass (LO)	16.96	—	—	—
SM (LO)	21.45	+4.29 −3.43	± 1.46	+4.53 −3.73
SM (NLO) [180]	33.89	+6.17 −4.98	+2.37 −2.01	+6.61 −5.37
SM (NNLO) [172]	36.69	+0.77 −1.83	± 1.10 ($g_{hq\bar{q}} = g_{hb\bar{b}}^{SM}$)	+1.66 −6.43 (incl. m_t uncertainty)
($g_{hq\bar{q}} = g_{hb\bar{b}}^{SM}$) (ggF-LO)	21.84	+4.38 −3.51	± 1.49	+4.62 −3.81

Table 7.1. Gluon fusion (ggF) Higgs pair production cross-section with theoretical systematic uncertainties, for infinite top mass limit (SM HEFT), running mass, LO, NLO and NNLO QCD corrections. The NLO and NNLO results are taken from the references cited in the table. We also state the benchmark point ($g_{hq\bar{q}} = g_{hb\bar{b}}^{SM}$) cross section result (all the light Yukawa couplings are scaled to the SM beauty Yukawa)

μ_F values ranging between:

$$\frac{M_{hh}}{4} \leq \mu_R/\mu_F \leq M_{hh} \quad (7.3)$$

The scale uncertainty for the LO total cross-section was found to be +20%, −16%. Moreover, the PDF+ α_s uncertainty was $\pm 6.8\%$.

results

The total cross sections with their uncertainties is shown in table ??.

8 Higgs pair as a probe for light Yukawas

9 Optimised search for Higgs pair via Interpretable machine learning

9.1 Overview of Light Yukawa searches

There are additional measurements of the light-quark Yukawa couplings that might become relevant at HL-LHC or FCC-hh, a careful study of which is beyond the scope of the current work. Yet we attempt to include a discussion here, so as to provide a comparison with our study and to put it into proper context, or to serve as proposal for further studies.

The channel $pp \rightarrow h + j$ has been suggested as a probe for charm Yukawa coupling [181] with charm-tagged jet having a potential bound of $\kappa_c \sim 1$ for the HL-LHC, depending on the charm-tagging scheme. This process could be used for the first and second generations Yukawa couplings by looking at the shapes of kinematic distributions, the most important one being the p_T distribution [182–184]. The expected HL-LHC 95% CL bounds are $\kappa_c \in [-0.6, 3.0]$, $|\kappa_u| \lesssim 170$ and $|\kappa_d| \lesssim 990$. The use of $h + j$ process along with other single Higgs processes have also been suggested as indirect probes for Higgs self coupling [69–73, 75], due to the contribution of the trilinear coupling to NLO electroweak corrections to these processes. In addition, experimental fits have been carried out for the trilinear coupling from single Higgs observables [78, 185].

It seems that for the HL-LHC, an optimal bound for the trilinear coupling can be obtained by combining both the data from single-Higgs process as well as Higgs pair production [77], with 68% CL bound on $\kappa_\lambda \in [0.1, 2.3]$, compared to the expected bound of $\kappa_\lambda \in [0.0, 2.5] \cup [4.9, 7.4]$ coming from using di-Higgs measurements alone. Moreover, single Higgs processes, namely Zh and $W^\pm h$ production, could also be useful in probing charm-Yukawa coupling using a mixture of b - and c -tagging schemes leveraging the mistagging probability of c -jets as b -jets in b -tagging working points, and vice-versa, in order to break the degeneracy in the signal strength [186]. The use of this technique could probe $\kappa_c \sim 1$ in the FCC-hh. Of course, for the charm-Yukawa coupling, the constraints are set to improve significantly, as there has been recent direct observation of $h \rightarrow c\bar{c}$ [187]. Therefore, from here on, we will mainly concentrate on the process with more potential for constraining Yukawa couplings of the first generation quarks.

Rare Higgs decays to mesons, $h \rightarrow M + V$, $M = \Upsilon, J/\Psi, \phi \dots$, were also suggested as a probe for light-quark Yukawa couplings [188–190], and there have been experimental searches for these decays [187, 191] with bounds on the branching ratios,

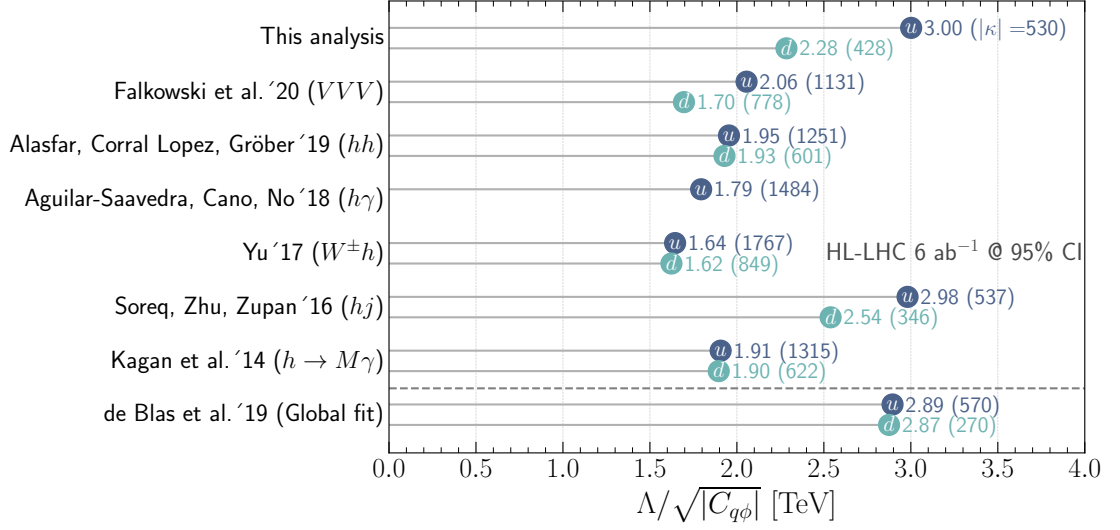


Figure 9.1. Summary of the 95% CI/CL sensitivity bounds on the SMEFT Wilson coefficients $C_{u\phi}$ (blue), and $C_{d\phi}$ (green). The bounds are interpreted in terms of the NP scale Λ that can be reached through the measurements of the Wilson coefficient at the HL-LHC at 6 ab^{-1} , the corresponding κ_q 's are shown inside the parentheses. Single parameter fit 95% CI bounds are used from this analysis for comparison with previous studies.

$\mathcal{B}(h \rightarrow X, \gamma, X = \Upsilon, J/\Psi, \dots) \sim 10^{-4} - 10^{-6}$ at 95% CL. It was shown in Ref. [192], that the charge asymmetry of the process $pp \rightarrow hW^+$ vs $pp \rightarrow hW^-$ can be used as a probe for light-quark Yukawa couplings as well as to break the degeneracy amongst quark flavours. Moreover, the rare process $pp \rightarrow h\gamma$ is also a possible way to distinguish between enhancements of the up- and down-Yukawa couplings [193] where the authors have estimated the bounds on the up-Yukawa coupling of $\kappa_u \sim 2000$ at the HL-LHC. Despite some processes appearing more sensitive than others, one should think of these processes as complementary to each other.

One of the main features of the effective couplings $hhq\bar{q}$ and $hhhq\bar{q}$ emerging from SMEFT operator $\mathcal{O}_{q\phi}$, or the Chiral Lagrangian for that matter, is that these couplings are either free from propagator suppression for $hhq\bar{q}$ or scale with energy for $hhhq\bar{q}$ while being safe from strong unitarity constraints. This feature gives processes with multiple Higgs and/or vector bosons $V = W^\pm, Z$ an advantage in constraining $\mathcal{O}_{q\phi}$. The latter constraints come from the longitudinal degrees of freedom of the gauge bosons which can be understood from the Goldstone boson equivalence theorem. The use of the final state VV as a probe for $\mathcal{O}_{q\phi}$ is difficult due to the large SM background. However, the three-boson final state VVV was shown to give strong projected bounds for light-quark Yukawa couplings for HL-LHC with 95% CL bounds on $\kappa_u \sim 1600$, and $\kappa_d \sim 1100$. A ten fold improvement is expected at FCC-hh [194] with bounds of order $\kappa_d \sim 30$. Higgs

pair production has a smaller SM background compared to VV production, but it has a significantly smaller cross section too, even when compared to VVV , as the latter process has already been observed at the LHC [195, 196].

On the contrary, Higgs pair production is inaccessible with the runs I-III of the LHC, but it is potentially accessible at the HL-LHC [197] having a $\sigma \cdot BR \sim 1\text{fb}^{-1}$. However, Higgs pair production, particularly the channel $h \rightarrow b\bar{b}\gamma\gamma$, is of significant interest as it has unique features. The first being the ability to constrain the trilinear and light-quark Yukawa couplings simultaneously, as we show in this work. Secondly, Higgs pair production could probe non-linear relations between Yukawa interaction and $hhq\bar{q}$ couplings [198, 199]. Lastly, Higgs pair production is expected to be significantly enhanced in certain models involving modification of light-quark Yukawa couplings (cf. [200–202]).

For future colliders, like the FCC-hh at 100 TeV, in addition to Higgs pair production triple Higgs production might be an interesting channel for constraining the operators with Wilson coefficient $C_{u\phi}$ and $C_{d\phi}$ due to the energy increase of a Feynman diagram coupling the quarks to three Higgs bosons. In this case, a similar study to ours should be performed to see whether also in this case it will be important to do a combined fit on the light quark Yukawa couplings together with the trilinear and quartic Higgs self-couplings.¹

Finally, we note that there are also non collider signatures for enhanced light-quark Yukawa couplings, manifesting in frequency shifts in atomic clocks from Higgs forces at the atomic level [204].

¹In [203], it was shown that $\sim \mathcal{O}(1)$ bounds on the quartic Higgs self-coupling can be reached at the FCC-hh.

A Details of Zh calculation

A.1 Orthogonal Projectors in $gg \rightarrow ZH$

In this appendix I present the explicit expressions of the projectors $\mathcal{P}_i^{\mu\nu\rho}$ appearing in eq.(6.2). The projectors are all normalized to 1. They are:

$$\mathcal{P}_1^{\mu\nu\rho} = \frac{m_Z}{\sqrt{2}s'p_T^2} \left[p_1^\nu \epsilon^{\mu\rho p_1 p_2} - p_2^\mu \epsilon^{\nu\rho p_1 p_2} + q_t^\mu \epsilon^{\nu\rho p_2 p_3} \right. \quad (\text{A.1})$$

$$\left. + q_u^\nu \epsilon^{\mu\rho p_1 p_3} + s' \epsilon^{\mu\nu\rho p_2} - s' \epsilon^{\mu\nu\rho p_1} \right], \quad (\text{A.2})$$

$$\mathcal{P}_2^{\mu\nu\rho} = \frac{1}{\sqrt{2}s'p_T} \left[q_u^\nu \epsilon^{\mu\rho p_1 p_3} + q_t^\mu \epsilon^{\nu\rho p_2 p_3} \right], \quad (\text{A.3})$$

$$\begin{aligned} \mathcal{P}_3^{\mu\nu\rho} &= \frac{\sqrt{3}}{2s'p_T} \left[s' \epsilon^{\mu\nu\rho p_1} + s' \epsilon^{\mu\nu\rho p_2} - p_1^\nu \epsilon^{\mu\rho p_1 p_2} - p_2^\mu \epsilon^{\nu\rho p_1 p_2} \right. \\ &+ (q_u^\nu \epsilon^{\mu\rho p_1 p_3} - q_t^\mu \epsilon^{\nu\rho p_2 p_3}) \left(\frac{1}{3} + \frac{m_Z^2}{p_T^2} \right) \\ &\left. + \frac{m_Z^2}{p_T^2} (q_t^\mu \epsilon^{\nu\rho p_2 p_1} - q_u^\nu \epsilon^{\mu\rho p_1 p_2}) \right], \end{aligned} \quad (\text{A.4})$$

$$\mathcal{P}_4^{\mu\nu\rho} = \frac{m_Z}{\sqrt{2}s'p_T^2} \left[q_t^\mu (\epsilon^{\nu\rho p_2 p_1} - \epsilon^{\nu\rho p_2 p_3}) - q_u^\nu (\epsilon^{\mu\rho p_1 p_2} - \epsilon^{\mu\rho p_1 p_3}) \right], \quad (\text{A.5})$$

$$\mathcal{P}_5^{\mu\nu\rho} = \frac{1}{\sqrt{6}s'p_T} \left[q_t^\mu \epsilon^{\nu\rho p_2 p_3} - q_u^\nu \epsilon^{\mu\rho p_1 p_3} \right], \quad (\text{A.6})$$

$$\begin{aligned} \mathcal{P}_6^{\mu\nu\rho} &= \frac{1}{s'p_T} \left[g^{\mu\nu} \epsilon^{\rho p_1 p_2 p_3} + s' \epsilon^{\mu\nu\rho p_3} + p_1^\nu \epsilon^{\mu\rho p_2 p_3} - p_2^\mu \epsilon^{\nu\rho p_1 p_3} - \frac{s'}{2} \epsilon^{\mu\nu\rho p_2} \right. \\ &+ \frac{1}{2} (p_1^\nu \epsilon^{\mu\rho p_1 p_2} + p_2^\mu \epsilon^{\nu\rho p_1 p_2} + q_u^\nu \epsilon^{\mu\rho p_1 p_3} - q_t^\mu \epsilon^{\nu\rho p_2 p_3} - s' \epsilon^{\mu\nu\rho p_1}) \\ &\left. + \frac{m_Z^2}{2p_T^2} (q_t^\mu \epsilon^{\nu\rho p_2 p_1} - q_u^\nu \epsilon^{\mu\rho p_1 p_2} + q_u^\nu \epsilon^{\mu\rho p_1 p_3} - q_t^\mu \epsilon^{\nu\rho p_2 p_3}) \right], \end{aligned} \quad (\text{A.7})$$

where we defined $q_t^\mu = (p_3^\mu - \frac{t'}{s'} p_2^\mu)$ and $q_u^\nu = (p_3^\nu - \frac{u'}{s'} p_1^\nu)$ and we used the shorthand notation $\epsilon^{\mu\nu\rho p_2} \equiv \epsilon^{\mu\nu\rho\sigma} p_2^\sigma$.

Using these projectors we obtained the relations between the form factors \mathcal{A}_i defined

in in eq.(6.2) and those defined in section 2 of ref.[137]:

$$\mathcal{A}_1 = \frac{p_T^2}{2\sqrt{2}m_Z(p_T^2 + m_Z^2)} \left[(t' + u')F_{12}^+ - (t' - u')F_{12}^- \right], \quad (\text{A.8})$$

$$\begin{aligned} \mathcal{A}_2 = & -\frac{p_T}{2\sqrt{2}(p_T^2 + m_Z^2)} \left[(t' + u')F_{12}^+ - (t' - u')F_{12}^- \right. \\ & \left. - \frac{p_T^2 + m_Z^2}{2s'} ((t' + u')F_3^+ - (t' - u')F_3^-) \right], \end{aligned} \quad (\text{A.9})$$

$$\begin{aligned} \mathcal{A}_3 = & \frac{p_T}{2\sqrt{3}(p_T^2 + m_Z^2)} \left[(t' + u')F_{12}^- - (t' - u')F_{12}^+ \right. \\ & \left. + (p_T^2 + m_Z^2)(F_2^- + F_4) \right], \end{aligned} \quad (\text{A.10})$$

$$\begin{aligned} \mathcal{A}_4 = & -\frac{m_Z}{2\sqrt{2}(p_T^2 + m_Z^2)} \left[(t' + u')F_{12}^- - (t' - u')F_{12}^+ \right. \\ & \left. + (p_T^2 + m_Z^2) \left(\left(1 - \frac{p_T^2}{m_Z^2}\right)F_2^- + 2F_4 \right) \right], \end{aligned} \quad (\text{A.11})$$

$$\begin{aligned} \mathcal{A}_5 = & \frac{p_T}{2\sqrt{6}(p_T^2 + m_Z^2)} \left[(t' + u')F_{12}^- - (t' - u')F_{12}^+ \right. \\ & \left. + (p_T^2 + m_Z^2) \left(4(F_2^- + F_4) + \frac{3}{2s'} ((t' + u')F_3^- - (t' - u')F_3^+) \right) \right], \end{aligned} \quad (\text{A.12})$$

$$\mathcal{A}_6 = \frac{p_T}{2} F_4. \quad (\text{A.13})$$

A.2 Two-loop Results

The NLO amplitude can be written in terms of three contributions, namely the two-loop 1PI triangle, the two-loop 1PI box and the reducible double-triangle diagrams,

$$\mathcal{A}_i^{(1)} = \mathcal{A}_i^{(1,\triangle)} + \mathcal{A}_i^{(1,\square)} + \mathcal{A}_i^{(1,\bowtie)}. \quad (\text{A.14})$$

In this section, the exact analytic results for the triangle and double triangle topologies are presented.

The two-loop triangle results are

$$\mathcal{A}_1^{(1,\Delta)} = \frac{p_T^2 (\hat{s} - \Delta_m)}{4\sqrt{2}m_Z} \frac{\mathcal{K}_t^{(2l)}}{(p_T^2 + m_Z^2)}, \quad (\text{A.15})$$

$$\mathcal{A}_2^{(1,\Delta)} = -\frac{p_T (\hat{s} - \Delta_m)}{4\sqrt{2}} \frac{\mathcal{K}_t^{(2l)}}{(p_T^2 + m_Z^2)}, \quad (\text{A.16})$$

$$\mathcal{A}_3^{(1,\Delta)} = \frac{p_T (\hat{t} - \hat{u})}{4\sqrt{3}} \frac{\mathcal{K}_t^{(2l)}}{(p_T^2 + m_Z^2)}, \quad (\text{A.17})$$

$$\mathcal{A}_4^{(1,\Delta)} = -\frac{m_Z (\hat{t} - \hat{u})}{4\sqrt{2}} \frac{\mathcal{K}_t^{(2l)}}{(p_T^2 + m_Z^2)}, \quad (\text{A.18})$$

$$\mathcal{A}_5^{(1,\Delta)} = -\frac{p_T (\hat{t} - \hat{u})}{4\sqrt{6}} \frac{\mathcal{K}_t^{(2l)}}{(p_T^2 + m_Z^2)}, \quad (\text{A.19})$$

$$\mathcal{A}_6^{(1,\Delta)} = 0, \quad (\text{A.20})$$

where the $\mathcal{K}_t^{(2l)}$ function is defined in eq.(4.11) of ref.[146]. While the double-triangle for-factors are found to be.

$$\mathcal{A}_1^{(1,\boxtimes)} = -\frac{m_t^2 p_T^2}{4\sqrt{2} m_Z (m_Z^2 + p_T^2)^2} \left[F_t(\hat{t}) (G_t(\hat{t}, \hat{u}) - G_b(\hat{t}, \hat{u})) + (\hat{t} \leftrightarrow \hat{u}) \right], \quad (\text{A.21})$$

$$\mathcal{A}_2^{(1,\boxtimes)} = \frac{m_t^2 p_T}{4\sqrt{2} (m_Z^2 + p_T^2)^2} \left[F_t(\hat{t}) (G_t(\hat{t}, \hat{u}) - G_b(\hat{t}, \hat{u})) + (\hat{t} \leftrightarrow \hat{u}) \right], \quad (\text{A.22})$$

$$\mathcal{A}_3^{(1,\boxtimes)} = \frac{m_t^2 p_T}{4\sqrt{3} \hat{s} (m_Z^2 + p_T^2)^2} \left[(m_h^2 - \hat{t}) F_t(\hat{t}) (G_t(\hat{t}, \hat{u}) - G_b(\hat{t}, \hat{u})) - (\hat{t} \leftrightarrow \hat{u}) \right], \quad (\text{A.23})$$

$$\begin{aligned} \mathcal{A}_4^{(1,\boxtimes)} &= -\frac{m_t^2}{4\sqrt{2} m_Z \hat{s}^2 (m_Z^2 + p_T^2)^2} \left[(m_Z^2 (m_h^2 - \hat{t})^2 \right. \\ &\quad \left. - \hat{t} (m_Z^2 - \hat{u})^2) F_t(\hat{t}) (G_t(\hat{t}, \hat{u}) - G_b(\hat{t}, \hat{u})) - (\hat{t} \leftrightarrow \hat{u}) \right], \end{aligned} \quad (\text{A.24})$$

$$\begin{aligned} \mathcal{A}_5^{(1,\boxtimes)} &= -\frac{m_t^2 p_T}{4\sqrt{6} \hat{s} (m_Z^2 + p_T^2)^2} \left[(4m_Z^2 - \hat{s} - 4\hat{u}) F_t(\hat{t}) (G_t(\hat{t}, \hat{u}) - G_b(\hat{t}, \hat{u})) \right. \\ &\quad \left. - (\hat{t} \leftrightarrow \hat{u}) \right], \end{aligned} \quad (\text{A.25})$$

$$\mathcal{A}_6^{(1,\boxtimes)} = 0, \quad (\text{A.26})$$

where

$$\begin{aligned}
 F_t(\hat{t}) &= \frac{1}{(m_h^2 - \hat{t})^2} \left[2\hat{t} \left(B_0(\hat{t}, m_t^2, m_t^2) - B_0(m_h^2, m_t^2, m_t^2) \right) \right. \\
 &\quad \left. + (m_h^2 - \hat{t}) \left((m_h^2 - 4m_t^2 - \hat{t}) C_0(0, m_h^2, \hat{t}, m_t^2, m_t^2, m_t^2) - 2 \right) \right],
 \end{aligned} \tag{A.27}$$

$$\begin{aligned}
 G_x(\hat{t}, \hat{u}) &= (m_z^2 - \hat{u}) \left[m_z^2 \left(B_0(\hat{t}, m_x^2, m_x^2) - B_0(m_z^2, m_x^2, m_x^2) \right) \right. \\
 &\quad \left. + (\hat{t} - m_z^2) \left(2m_x^2 C_0(0, \hat{t}, m_z^2, m_x^2, m_x^2, m_x^2) + 1 \right) \right].
 \end{aligned} \tag{A.28}$$

Bibliography

- [1] R. A. Minlos, *Introduction to mathematical statistical physics*. No. 19. American Mathematical Soc., 2000.
- [2] M. Gell-Mann, “The eightfold way: A theory of strong interaction symmetry,” <https://www.osti.gov/biblio/4008239>.
- [3] C. N. Yang and R. L. Mills, “Conservation of isotopic spin and isotopic gauge invariance,” *Phys. Rev.* **96** (Oct, 1954) 191–195.
<https://link.aps.org/doi/10.1103/PhysRev.96.191>.
- [4] **Particle Data Group** Collaboration, P. Zyla *et al.*, “Review of Particle Physics,” *PTEP* **2020** no. 8, (2020) 083C01.
- [5] D. S. Freed, “Lectures on topological quantum field theory,” 1993.
- [6] R. Dijkgraaf and E. Witten, “Topological gauge theories and group cohomology,” *Communications in Mathematical Physics* **129** no. 2, (1990) 393–429.
- [7] A. Salam and J. C. Ward, “On a gauge theory of elementary interactions,” *Il Nuovo Cimento (1955-1965)* **19** no. 1, (1961) 165–170.
<https://doi.org/10.1007/BF02812723>.
- [8] A. Salam and J. C. Ward, “Weak and electromagnetic interactions,” *Il Nuovo Cimento (1955-1965)* **11** no. 4, (1959) 568–577.
<https://doi.org/10.1007/BF02726525>.
- [9] S. Weinberg, “A model of leptons,” *Phys. Rev. Lett.* **19** (Nov, 1967) 1264–1266.
<https://link.aps.org/doi/10.1103/PhysRevLett.19.1264>.
- [10] F. Capozzi, E. Lisi, A. Marrone, D. Montanino, and A. Palazzo, “Neutrino masses and mixings: Status of known and unknown 3ν parameters,” *Nucl. Phys. B* **908** (2016) 218–234, [arXiv:1601.07777](https://arxiv.org/abs/1601.07777) [hep-ph].
- [11] **ALEPH, DELPHI, L3, OPAL, SLD, LEP Electroweak Working Group, SLD Electroweak Group, SLD Heavy Flavour Group** Collaboration, S. Schael *et al.*, “Precision electroweak measurements on the Z resonance,” *Phys. Rept.* **427** (2006) 257–454, [arXiv:hep-ex/0509008](https://arxiv.org/abs/hep-ex/0509008).

- [12] **SLD** Collaboration, K. Abe *et al.*, “First direct measurement of the parity violating coupling of the Z^0 to the s quark,” *Phys. Rev. Lett.* **85** (2000) 5059–5063, [arXiv:hep-ex/0006019](#).
- [13] **CDF, D0** Collaboration, T. E. W. Group, “2012 Update of the Combination of CDF and D0 Results for the Mass of the W Boson,” [arXiv:1204.0042 \[hep-ex\]](#).
- [14] **ALEPH, DELPHI, L3, OPAL, LEP Electroweak** Collaboration, S. Schael *et al.*, “Electroweak Measurements in Electron-Positron Collisions at W -Boson-Pair Energies at LEP,” *Phys. Rept.* **532** (2013) 119–244, [arXiv:1302.3415 \[hep-ex\]](#).
- [15] **DØ** Collaboration, V. M. Abazov *et al.*, “Measurement of $\sin^2 \theta_{\text{eff}}^\ell$ and Z -light quark couplings using the forward-backward charge asymmetry in $p\bar{p} \rightarrow Z/\gamma^* \rightarrow e^+e^-$ events with $\mathcal{L} = 5.0 \text{ fb}^{-1}$ at $\sqrt{s} = 1.96 \text{ TeV}$,” *Phys. Rev. D* **84** (2011) 012007, [arXiv:1104.4590 \[hep-ex\]](#).
- [16] **CMS** Collaboration, V. Khachatryan *et al.*, “Measurement of the t -channel single-top-quark production cross section and of the $|V_{tb}|$ CKM matrix element in pp collisions at $\sqrt{s} = 8 \text{ TeV}$,” *JHEP* **06** (2014) 090, [arXiv:1403.7366 \[hep-ex\]](#).
- [17] **ATLAS** Collaboration, M. Aaboud *et al.*, “Measurement of the W -boson mass in pp collisions at $\sqrt{s} = 7 \text{ TeV}$ with the ATLAS detector,” *Eur. Phys. J. C* **78** no. 2, (2018) 110, [arXiv:1701.07240 \[hep-ex\]](#). [Erratum: *Eur. Phys. J. C* **78**, 898 (2018)].
- [18] Y. Nambu, “Quasi-particles and gauge invariance in the theory of superconductivity,” *Phys. Rev.* **117** (Feb, 1960) 648–663. <https://link.aps.org/doi/10.1103/PhysRev.117.648>.
- [19] J. Goldstone, “Field theories with superconductor solutions,” *Il Nuovo Cimento (1955-1965)* **19** no. 1, (1961) 154–164.
- [20] J. Goldstone, A. Salam, and S. Weinberg, “Broken symmetries,” *Phys. Rev.* **127** (Aug, 1962) 965–970. <https://link.aps.org/doi/10.1103/PhysRev.127.965>.
- [21] P. W. Anderson, “Plasmons, gauge invariance, and mass,” *Phys. Rev.* **130** (Apr, 1963) 439–442. <https://link.aps.org/doi/10.1103/PhysRev.130.439>.
- [22] F. Englert and R. Brout, “Broken symmetry and the mass of gauge vector mesons,” *Phys. Rev. Lett.* **13** (Aug, 1964) 321–323. <https://link.aps.org/doi/10.1103/PhysRevLett.13.321>.

-
- [23] P. W. Higgs, “Broken symmetries and the masses of gauge bosons,” *Phys. Rev. Lett.* **13** (Oct, 1964) 508–509.
<https://link.aps.org/doi/10.1103/PhysRevLett.13.508>.
- [24] G. S. Guralnik, C. R. Hagen, and T. W. B. Kibble, “Global conservation laws and massless particles,” *Phys. Rev. Lett.* **13** (Nov, 1964) 585–587.
<https://link.aps.org/doi/10.1103/PhysRevLett.13.585>.
- [25] G. S. Guralnik, “The History of the Guralnik, Hagen and Kibble development of the Theory of Spontaneous Symmetry Breaking and Gauge Particles,” *Int. J. Mod. Phys. A* **24** (2009) 2601–2627, [arXiv:0907.3466](https://arxiv.org/abs/0907.3466) [physics.hist-ph].
- [26] CMS Collaboration, S. Chatrchyan *et al.*, “Observation of a New Boson at a Mass of 125 GeV with the CMS Experiment at the LHC,” *Phys. Lett. B* **716** (2012) 30–61, [arXiv:1207.7235](https://arxiv.org/abs/1207.7235) [hep-ex].
- [27] ATLAS Collaboration, G. Aad *et al.*, “Observation of a new particle in the search for the Standard Model Higgs boson with the ATLAS detector at the LHC,” *Phys. Lett. B* **716** (2012) 1–29, [arXiv:1207.7214](https://arxiv.org/abs/1207.7214) [hep-ex].
- [28] N. Cabibbo, “Unitary symmetry and leptonic decays,” *Phys. Rev. Lett.* **10** (Jun, 1963) 531–533. <https://link.aps.org/doi/10.1103/PhysRevLett.10.531>.
- [29] M. Kobayashi and T. Maskawa, “CP-Violation in the Renormalizable Theory of Weak Interaction,” *Progress of Theoretical Physics* **49** no. 2, (02, 1973) 652–657, <https://academic.oup.com/ptp/article-pdf/49/2/652/5257692/49-2-652.pdf>.
<https://doi.org/10.1143/PTP.49.652>.
- [30] R. E. Behrends, R. J. Finkelstein, and A. Sirlin, “Radiative corrections to decay processes,” *Phys. Rev.* **101** (Jan, 1956) 866–873.
<https://link.aps.org/doi/10.1103/PhysRev.101.866>.
- [31] T. Kinoshita and A. Sirlin, “Radiative corrections to fermi interactions,” *Phys. Rev.* **113** (Mar, 1959) 1652–1660.
<https://link.aps.org/doi/10.1103/PhysRev.113.1652>.
- [32] I. Mohammad and A. Donnachie, “Radiative Corrections to Radiative Muon Decay,”.
- [33] T. van Ritbergen and R. G. Stuart, “Complete 2-loop quantum electrodynamic contributions to the muon lifetime in the fermi model,” *Phys. Rev. Lett.* **82** (Jan, 1999) 488–491. <https://link.aps.org/doi/10.1103/PhysRevLett.82.488>.
- [34] D. Ross and M. Veltman, “Neutral currents and the higgs mechanism,” *Nuclear Physics B* **95** no. 1, (1975) 135–147.
<https://www.sciencedirect.com/science/article/pii/055032137590485X>.

- [35] A. Djouadi, “The Anatomy of electro-weak symmetry breaking. I: The Higgs boson in the standard model,” *Phys. Rept.* **457** (2008) 1–216, [arXiv:hep-ph/0503172](#).
- [36] M. J. Dugan, H. Georgi, and D. B. Kaplan, “Anatomy of a composite higgs model,” *Nuclear Physics* **254** (1985) 299–326.
- [37] C. T. Hill and E. H. Simmons, “Strong Dynamics and Electroweak Symmetry Breaking,” *Phys. Rept.* **381** (2003) 235–402, [arXiv:hep-ph/0203079](#). [Erratum: *Phys.Rept.* 390, 553–554 (2004)].
- [38] M. Schwartz, *Quantum Field Theory and the Standard Model*. Quantum Field Theory and the Standard Model. Cambridge University Press, 2014. <https://books.google.nl/books?id=HbdEAgAAQBAJ>.
- [39] M. Peskin and D. Schroeder, *An Introduction To Quantum Field Theory*. Frontiers in Physics. Avalon Publishing, 1995. <https://books.google.de/books?id=EVeNNcslvX0C>.
- [40] M. Einhorn, D. Jones, and M. Veltman, “Heavy particles and the rho parameter in the standard model,” *Nuclear Physics B* **191** no. 1, (1981) 146–172. <https://www.sciencedirect.com/science/article/pii/0550321381902923>.
- [41] M. E. Peskin and T. Takeuchi, “New constraint on a strongly interacting higgs sector,” *Phys. Rev. Lett.* **65** (Aug, 1990) 964–967. <https://link.aps.org/doi/10.1103/PhysRevLett.65.964>.
- [42] M. E. Peskin and T. Takeuchi, “Estimation of oblique electroweak corrections,” 1991.
- [43] M. Golden and L. Randall, “Radiative corrections to electroweak parameters in technicolor theories,” *Nuclear Physics B* **361** no. 1, (1991) 3–23. <https://www.sciencedirect.com/science/article/pii/0550321391906144>.
- [44] B. Holdom and J. Terning, “Large corrections to electroweak parameters in technicolor theories,” *Physics Letters B* **247** no. 1, (1990) 88–92. <https://www.sciencedirect.com/science/article/pii/037026939091054F>.
- [45] G. Altarelli, R. Barbieri, and S. Jadach, “Toward a model-independent analysis of electroweak data,” *Nuclear Physics B* **369** no. 1, (1992) 3–32. <https://www.sciencedirect.com/science/article/pii/055032139290376M>.
- [46] R. S. Chivukula, S. B. Selipsky, and E. H. Simmons, “Nonoblique effects in the zbb^- vertex from extended technicolor dynamics,” *Phys. Rev. Lett.* **69** (Jul, 1992) 575–577. <https://link.aps.org/doi/10.1103/PhysRevLett.69.575>.

-
- [47] E. H. Simmons, R. S. Chivukula, and J. Terning, “Testing extended technicolor with $R(b)$,” *Prog. Theor. Phys. Suppl.* **123** (1996) 87–96, [arXiv:hep-ph/9509392](#).
 - [48] M. Cepeda *et al.*, “Report from Working Group 2: Higgs Physics at the HL-LHC and HE-LHC,” *CERN Yellow Rep. Monogr.* **7** (2019) 221–584, [arXiv:1902.00134 \[hep-ph\]](#).
 - [49] **ATLAS** Collaboration, “A combination of measurements of Higgs boson production and decay using up to 139 fb^{-1} of proton–proton collision data at $\sqrt{s} = 13\text{ TeV}$ collected with the ATLAS experiment,” Tech. Rep. ATLAS-CONF-2020-027, 2020.
 - [50] **CMS** Collaboration, A. M. Sirunyan *et al.*, “Measurements of Higgs boson production cross sections and couplings in the diphoton decay channel at $\sqrt{s} = 13\text{ TeV}$,” *JHEP* **07** (2021) 027, [arXiv:2103.06956 \[hep-ex\]](#).
 - [51] **CMS Collaboration** Collaboration, “Sensitivity projections for Higgs boson properties measurements at the HL-LHC,” tech. rep., CERN, Geneva, 2018. <https://cds.cern.ch/record/2647699>.
 - [52] **CMS** Collaboration, “Combined Higgs boson production and decay measurements with up to 137 fb^{-1} of proton-proton collision data at $\sqrt{s} = 13\text{ TeV}$,” Tech. Rep. CMS-PAS-HIG-19-005, 2020.
 - [53] **CMS** Collaboration, “Measurement of Higgs boson production in association with a W or Z boson in the $H \rightarrow WW$ decay channel,” Tech. Rep. CMS-PAS-HIG-19-017, 2021.
 - [54] **ATLAS** Collaboration, G. Aad *et al.*, “Combined measurements of Higgs boson production and decay using up to 80 fb^{-1} of proton-proton collision data at $\sqrt{s} = 13\text{ TeV}$ collected with the ATLAS experiment,” *Phys. Rev. D* **101** no. 1, (2020) 012002, [arXiv:1909.02845 \[hep-ex\]](#).
 - [55] **CMS** Collaboration, A. M. Sirunyan *et al.*, “Combined measurements of Higgs boson couplings in proton–proton collisions at $\sqrt{s} = 13\text{ TeV}$,” *Eur. Phys. J. C* **79** no. 5, (2019) 421, [arXiv:1809.10733 \[hep-ex\]](#).
 - [56] R. Frederix, D. Pagani, and M. Zaro, “Large NLO corrections in $t\bar{t}W^\pm$ and $t\bar{t}t\bar{t}$ hadroproduction from supposedly subleading EW contributions,” *JHEP* **02** (2018) 031, [arXiv:1711.02116 \[hep-ph\]](#).
 - [57] **ATLAS** Collaboration, G. Aad *et al.*, “Evidence for $t\bar{t}t\bar{t}$ production in the multilepton final state in proton–proton collisions at $\sqrt{s} = 13\text{ TeV}$ with the

- ATLAS detector,” *Eur. Phys. J. C* **80** no. 11, (2020) 1085, [arXiv:2007.14858 \[hep-ex\]](#).
- [58] **CMS** Collaboration, A. M. Sirunyan *et al.*, “Search for the production of four top quarks in the single-lepton and opposite-sign dilepton final states in proton-proton collisions at $\sqrt{s} = 13$ TeV,” *JHEP* **11** (2019) 082, [arXiv:1906.02805 \[hep-ex\]](#).
- [59] N. P. Hartland, F. Maltoni, E. R. Nocera, J. Rojo, E. Slade, E. Vryonidou, and C. Zhang, “A Monte Carlo global analysis of the Standard Model Effective Field Theory: the top quark sector,” *JHEP* **04** (2019) 100, [arXiv:1901.05965 \[hep-ph\]](#).
- [60] G. Banelli, E. Salvioni, J. Serra, T. Theil, and A. Weiler, “The Present and Future of Four Top Operators,” *JHEP* **02** (2021) 043, [arXiv:2010.05915 \[hep-ph\]](#).
- [61] **CMS** Collaboration, A. M. Sirunyan *et al.*, “Measurement of the cross section for $t\bar{t}$ production with additional jets and b jets in pp collisions at $\sqrt{s} = 13$ TeV,” *JHEP* **07** (2020) 125, [arXiv:2003.06467 \[hep-ex\]](#).
- [62] **ATLAS** Collaboration, “Measurements of fiducial and differential cross-sections of $t\bar{t}$ production with additional heavy-flavour jets in proton-proton collisions at $\sqrt{s} = 13$ TeV with the ATLAS detector,” Tech. Rep. ATLAS-CONF-2018-029, 2018.
- [63] J. D’Hondt, A. Mariotti, K. Mimasu, S. Moortgat, and C. Zhang, “Learning to pinpoint effective operators at the LHC: a study of the $t\bar{t}b\bar{b}$ signature,” *JHEP* **11** (2018) 131, [arXiv:1807.02130 \[hep-ph\]](#).
- [64] C. Degrande, G. Durieux, F. Maltoni, K. Mimasu, E. Vryonidou, and C. Zhang, “Automated one-loop computations in the standard model effective field theory,” *Phys. Rev. D* **103** no. 9, (2021) 096024, [arXiv:2008.11743 \[hep-ph\]](#).
- [65] J. de Blas, M. Chala, and J. Santiago, “Renormalization Group Constraints on New Top Interactions from Electroweak Precision Data,” *JHEP* **09** (2015) 189, [arXiv:1507.00757 \[hep-ph\]](#).
- [66] E. E. Jenkins, A. V. Manohar, and M. Trott, “Renormalization Group Evolution of the Standard Model Dimension Six Operators I: Formalism and lambda Dependence,” *JHEP* **10** (2013) 087, [arXiv:1308.2627 \[hep-ph\]](#).
- [67] E. E. Jenkins, A. V. Manohar, and M. Trott, “Renormalization Group Evolution of the Standard Model Dimension Six Operators II: Yukawa Dependence,” *JHEP* **01** (2014) 035, [arXiv:1310.4838 \[hep-ph\]](#).

-
- [68] R. Alonso, E. E. Jenkins, A. V. Manohar, and M. Trott, “Renormalization Group Evolution of the Standard Model Dimension Six Operators III: Gauge Coupling Dependence and Phenomenology,” *JHEP* **04** (2014) 159, [arXiv:1312.2014 \[hep-ph\]](#).
- [69] M. McCullough, “An Indirect Model-Dependent Probe of the Higgs Self-Coupling,” *Phys. Rev. D* **90** no. 1, (2014) 015001, [arXiv:1312.3322 \[hep-ph\]](#). [Erratum: *Phys.Rev.D* 92, 039903 (2015)].
- [70] M. Gorbahn and U. Haisch, “Indirect probes of the trilinear Higgs coupling: $gg \rightarrow h$ and $h \rightarrow \gamma\gamma$,” *JHEP* **10** (2016) 094, [arXiv:1607.03773 \[hep-ph\]](#).
- [71] G. Degrandi, P. P. Giardino, F. Maltoni, and D. Pagani, “Probing the Higgs self coupling via single Higgs production at the LHC,” *JHEP* **12** (2016) 080, [arXiv:1607.04251 \[hep-ph\]](#).
- [72] W. Bizon, M. Gorbahn, U. Haisch, and G. Zanderighi, “Constraints on the trilinear Higgs coupling from vector boson fusion and associated Higgs production at the LHC,” *JHEP* **07** (2017) 083, [arXiv:1610.05771 \[hep-ph\]](#).
- [73] F. Maltoni, D. Pagani, A. Shivaji, and X. Zhao, “Trilinear Higgs coupling determination via single-Higgs differential measurements at the LHC,” *Eur. Phys. J. C* **77** no. 12, (2017) 887, [arXiv:1709.08649 \[hep-ph\]](#).
- [74] G. Degrandi and M. Vitti, “The effect of an anomalous Higgs trilinear self-coupling on the $h \rightarrow \gamma Z$ decay,” *Eur. Phys. J. C* **80** no. 4, (2020) 307, [arXiv:1912.06429 \[hep-ph\]](#).
- [75] G. Degrandi, B. Di Micco, P. P. Giardino, and E. Rossi, “Higgs boson self-coupling constraints from single Higgs, double Higgs and Electroweak measurements,” *Phys. Lett. B* **817** (2021) 136307, [arXiv:2102.07651 \[hep-ph\]](#).
- [76] U. Haisch and G. Koole, “Off-shell Higgs production at the LHC as a probe of the trilinear Higgs coupling,” [arXiv:2111.12589 \[hep-ph\]](#).
- [77] S. Di Vita, C. Grojean, G. Panico, M. Riembau, and T. Vantalon, “A global view on the Higgs self-coupling,” *JHEP* **09** (2017) 069, [arXiv:1704.01953 \[hep-ph\]](#).
- [78] **ATLAS** Collaboration, “Constraints on the Higgs boson self-coupling from the combination of single-Higgs and double-Higgs production analyses performed with the ATLAS experiment,” Tech. Rep. ATLAS-CONF-2019-049, 2019.
- [79] B. Grzadkowski, M. Iskrzynski, M. Misiak, and J. Rosiek, “Dimension-Six Terms in the Standard Model Lagrangian,” *JHEP* **10** (2010) 085, [arXiv:1008.4884 \[hep-ph\]](#).

- [80] H. Patel, “Package-X: A Mathematica package for the analytic calculation of one-loop integrals,” *Comput. Phys. Commun.* **197** (2015) 276–290, [arXiv:1503.01469 \[hep-ph\]](#).
- [81] P. Maierhöfer, J. Usovitsch, and P. Uwer, “Kira—A Feynman integral reduction program,” *Comput. Phys. Commun.* **230** (2018) 99–112, [arXiv:1705.05610 \[hep-ph\]](#).
- [82] A. Smirnov, “Algorithm FIRE – Feynman Integral REduction,” *JHEP* **10** (2008) 107, [arXiv:0807.3243 \[hep-ph\]](#).
- [83] A. Alloul, N. D. Christensen, C. Degrande, C. Duhr, and B. Fuks, “FeynRules 2.0 - A complete toolbox for tree-level phenomenology,” *Comput. Phys. Commun.* **185** (2014) 2250–2300, [arXiv:1310.1921 \[hep-ph\]](#).
- [84] T. Hahn, “Generating Feynman diagrams and amplitudes with FeynArts 3,” *Comput. Phys. Commun.* **140** (2001) 418–431, [arXiv:hep-ph/0012260](#).
- [85] A. Dedes, W. Materkowska, M. Paraskevas, J. Rosiek, and K. Suxho, “Feynman rules for the Standard Model Effective Field Theory in R_ξ -gauges,” *JHEP* **06** (2017) 143, [arXiv:1704.03888 \[hep-ph\]](#).
- [86] S. Dawson and P. P. Giardino, “Higgs decays to ZZ and $Z\gamma$ in the standard model effective field theory: An NLO analysis,” *Phys. Rev. D* **97** no. 9, (2018) 093003, [arXiv:1801.01136 \[hep-ph\]](#).
- [87] R. Gauld, B. D. Pecjak, and D. J. Scott, “One-loop corrections to $h \rightarrow b\bar{b}$ and $h \rightarrow \tau\bar{\tau}$ decays in the Standard Model Dimension-6 EFT: four-fermion operators and the large- m_t limit,” *JHEP* **05** (2016) 080, [arXiv:1512.02508 \[hep-ph\]](#).
- [88] J. Alwall, R. Frederix, S. Frixione, V. Hirschi, F. Maltoni, O. Mattelaer, H. S. Shao, T. Stelzer, P. Torrielli, and M. Zaro, “The automated computation of tree-level and next-to-leading order differential cross sections, and their matching to parton shower simulations,” *JHEP* **07** (2014) 079, [arXiv:1405.0301 \[hep-ph\]](#).
- [89] G. Ossola, C. G. Papadopoulos, and R. Pittau, “Reducing full one-loop amplitudes to scalar integrals at the integrand level,” *Nucl. Phys. B* **763** (2007) 147–169, [arXiv:hep-ph/0609007](#).
- [90] G. Ossola, C. G. Papadopoulos, and R. Pittau, “CutTools: A Program implementing the OPP reduction method to compute one-loop amplitudes,” *JHEP* **03** (2008) 042, [arXiv:0711.3596 \[hep-ph\]](#).

-
- [91] G. Ossola, C. G. Papadopoulos, and R. Pittau, “On the Rational Terms of the one-loop amplitudes,” *JHEP* **05** (2008) 004, [arXiv:0802.1876 \[hep-ph\]](#).
- [92] R. D. Ball *et al.*, “Parton distributions with LHC data,” *Nucl. Phys. B* **867** (2013) 244–289, [arXiv:1207.1303 \[hep-ph\]](#).
- [93] J. Salvatier, T. V. Wiecki, and C. Fonnesbeck, “Probabilistic programming in python using PyMC3,” *PeerJ Computer Science* **2** (Apr, 2016) e55. <https://doi.org/10.7717/peerj-cs.55>.
- [94] R. Kumar, C. Carroll, A. Hartikainen, and O. Martin, “Arviz a unified library for exploratory analysis of bayesian models in python,” *Journal of Open Source Software* **4** no. 33, (2019) 1143. <https://doi.org/10.21105/joss.01143>.
- [95] F. James and M. Roos, “Minuit: A System for Function Minimization and Analysis of the Parameter Errors and Correlations,” *Comput. Phys. Commun.* **10** (1975) 343–367.
- [96] H. Dembinski and P. O. et al., “scikit-hep/iminuit,” <https://doi.org/10.5281/zenodo.3949207>.
- [97] D. Foreman-Mackey, “corner.py: Scatterplot matrices in python,” *The Journal of Open Source Software* **1** no. 2, (Jun, 2016) 24. <https://doi.org/10.21105/joss.00024>.
- [98] S. Bocquet and F. W. Carter, “pygtc: beautiful parameter covariance plots (aka. giant triangle confusograms),” *The Journal of Open Source Software* **1** no. 6, (Oct, 2016) . <http://dx.doi.org/10.21105/joss.00046>.
- [99] P. Zivich, “pzivich/Python-for-Epidemiologists: Updates for v0.8.0,” July, 2019. <https://doi.org/10.5281/zenodo.3339870>.
- [100] <https://github.com/alasfar-lina/trilinear4tops>.
- [101] **SMEFT** Collaboration, J. J. Ethier, G. Magni, F. Maltoni, L. Mantani, E. R. Nocera, J. Rojo, E. Slade, E. Vryonidou, and C. Zhang, “Combined SMEFT interpretation of Higgs, diboson, and top quark data from the LHC,” *JHEP* **11** (2021) 089, [arXiv:2105.00006 \[hep-ph\]](#).
- [102] J. Ellis, M. Madigan, K. Mimasu, V. Sanz, and T. You, “Top, Higgs, Diboson and Electroweak Fit to the Standard Model Effective Field Theory,” *JHEP* **04** (2021) 279, [arXiv:2012.02779 \[hep-ph\]](#).
- [103] I. Brivio, S. Bruggisser, F. Maltoni, R. Moutafis, T. Plehn, E. Vryonidou, S. Westhoff, and C. Zhang, “O new physics, where art thou? A global search in the top sector,” *JHEP* **02** (2020) 131, [arXiv:1910.03606 \[hep-ph\]](#).

- [104] C. Zhang, “Constraining $qqtt$ operators from four-top production: a case for enhanced EFT sensitivity,” *Chin. Phys. C* **42** no. 2, (2018) 023104, [arXiv:1708.05928 \[hep-ph\]](#).
- [105] **ATLAS** Collaboration, “Search for Higgs boson pair production in the two bottom quarks plus two photons final state in pp collisions at $\sqrt{s} = 13$ TeV with the ATLAS detector,” Tech. Rep. ATLAS-CONF-2021-016, 2021.
- [106] L. Di Luzio, R. Gröber, and M. Spannowsky, “Maxi-sizing the trilinear Higgs self-coupling: how large could it be?,” *Eur. Phys. J. C* **77** no. 11, (2017) 788, [arXiv:1704.02311 \[hep-ph\]](#).
- [107] L. Alasfar, R. Gröber, C. Grojean, A. Paul, and Z. Qian, “Machine learning augmented probes of light-quark Yukawa and trilinear couplings from Higgs pair production,” *In preparation* (2021) .
- [108] “Guidelines for extrapolation of cms and atlas lhch/hl-lhc couplings projections to he-lhc.” <https://twiki.cern.ch/twiki/bin/view/LHCPhysics/GuidelinesCouplingProjections2018#Details%20of%20the%20CMS%20projections>.
- [109] J. Alison *et al.*, “Higgs boson potential at colliders: Status and perspectives,” *Rev. Phys.* **5** (2020) 100045, [arXiv:1910.00012 \[hep-ph\]](#).
- [110] **CMS** Collaboration, “Prospects for HH measurements at the HL-LHC,” *CMS-PAS-FTR-18-019* (2018) .
- [111] **FCC** Collaboration, A. Abada *et al.*, “FCC Physics Opportunities: Future Circular Collider Conceptual Design Report Volume 1,” *Eur. Phys. J. C* **79** no. 6, (2019) 474.
- [112] **FCC** Collaboration, A. Abada *et al.*, “FCC-ee: The Lepton Collider: Future Circular Collider Conceptual Design Report Volume 2,” *Eur. Phys. J. ST* **228** no. 2, (2019) 261–623.
- [113] P. Bambade *et al.*, “The International Linear Collider: A Global Project,” [arXiv:1903.01629 \[hep-ex\]](#).
- [114] **LCC Physics Working Group** Collaboration, K. Fujii *et al.*, “Tests of the Standard Model at the International Linear Collider,” [arXiv:1908.11299 \[hep-ex\]](#).
- [115] F. An *et al.*, “Precision Higgs physics at the CEPC,” *Chin. Phys. C* **43** no. 4, (2019) 043002, [arXiv:1810.09037 \[hep-ex\]](#).

-
- [116] **CEPC Study Group** Collaboration, M. Dong *et al.*, “CEPC Conceptual Design Report: Volume 2 - Physics & Detector,” [arXiv:1811.10545 \[hep-ex\]](#).
- [117] **CLICdp, CLIC** Collaboration, T. K. Charles *et al.*, “The Compact Linear Collider (CLIC) - 2018 Summary Report,” [arXiv:1812.06018 \[physics.acc-ph\]](#).
- [118] J. de Blas *et al.*, “The CLIC Potential for New Physics,” [arXiv:1812.02093 \[hep-ph\]](#).
- [119] S. Di Vita, G. Durieux, C. Grojean, J. Gu, Z. Liu, G. Panico, M. Riembau, and T. Vantalón, “A global view on the Higgs self-coupling at lepton colliders,” *JHEP* **02** (2018) 178, [arXiv:1711.03978 \[hep-ph\]](#).
- [120] J. de Blas, J. C. Criado, M. Perez-Victoria, and J. Santiago, “Effective description of general extensions of the Standard Model: the complete tree-level dictionary,” *JHEP* **03** (2018) 109, [arXiv:1711.10391 \[hep-ph\]](#).
- [121] Anisha, S. D. Bakshi, S. Banerjee, A. Biekötter, J. Chakraborty, S. K. Patra, and M. Spannowsky, “Effective limits on single scalar extensions in the light of recent LHC data,” [arXiv:2111.05876 \[hep-ph\]](#).
- [122] **ATLAS** Collaboration, M. Aaboud *et al.*, “Observation of $H \rightarrow b\bar{b}$ decays and VH production with the ATLAS detector,” *Phys. Lett. B* **786** (2018) 59–86, [arXiv:1808.08238 \[hep-ex\]](#).
- [123] **CMS** Collaboration, A. M. Sirunyan *et al.*, “Observation of Higgs boson decay to bottom quarks,” *Phys. Rev. Lett.* **121** no. 12, (2018) 121801, [arXiv:1808.08242 \[hep-ex\]](#).
- [124] T. Han and S. Willenbrock, “QCD correction to the $p p \rightarrow W H$ and $Z H$ total cross-sections,” *Phys. Lett. B* **273** (1991) 167–172.
- [125] O. Brein, A. Djouadi, and R. Harlander, “NNLO QCD corrections to the Higgs-strahlung processes at hadron colliders,” *Phys. Lett. B* **579** (2004) 149–156, [arXiv:hep-ph/0307206](#).
- [126] S. Amoroso *et al.*, “Les Houches 2019: Physics at TeV Colliders: Standard Model Working Group Report,” in *11th Les Houches Workshop on Physics at TeV Colliders: PhysTeV Les Houches*. 3, 2020. [arXiv:2003.01700 \[hep-ph\]](#).
- [127] C. Englert, M. McCullough, and M. Spannowsky, “Gluon-initiated associated production boosts Higgs physics,” *Phys. Rev. D* **89** no. 1, (2014) 013013, [arXiv:1310.4828 \[hep-ph\]](#).

- [128] C. Englert, R. Rosenfeld, M. Spannowsky, and A. Tonero, “New physics and signal-background interference in associated $pp \rightarrow HZ$ production,” *EPL* **114** no. 3, (2016) 31001, [arXiv:1603.05304 \[hep-ph\]](#).
- [129] R. V. Harlander, S. Liebler, and T. Zirke, “Higgs Strahlung at the Large Hadron Collider in the 2-Higgs-Doublet Model,” *JHEP* **02** (2014) 023, [arXiv:1307.8122 \[hep-ph\]](#).
- [130] B. A. Kniehl, “Associated Production of Higgs and Z Bosons From Gluon Fusion in Hadron Collisions,” *Phys. Rev. D* **42** (1990) 2253–2258.
- [131] D. A. Dicus and C. Kao, “Higgs Boson - Z^0 Production From Gluon Fusion,” *Phys. Rev. D* **38** (1988) 1008. [Erratum: *Phys.Rev.D* 42, 2412 (1990)].
- [132] L. Altenkamp, S. Dittmaier, R. V. Harlander, H. Rzehak, and T. J. Zirke, “Gluon-induced Higgs-strahlung at next-to-leading order QCD,” *JHEP* **02** (2013) 078, [arXiv:1211.5015 \[hep-ph\]](#).
- [133] R. V. Harlander, A. Kulesza, V. Theeuwes, and T. Zirke, “Soft gluon resummation for gluon-induced Higgs Strahlung,” *JHEP* **11** (2014) 082, [arXiv:1410.0217 \[hep-ph\]](#).
- [134] A. Hasselhuhn, T. Luthe, and M. Steinhauser, “On top quark mass effects to $gg \rightarrow ZH$ at NLO,” *JHEP* **01** (2017) 073, [arXiv:1611.05881 \[hep-ph\]](#).
- [135] R. Harlander, J. Klappert, C. Pandini, and A. Papaefstathiou, “Exploiting the WH/ZH symmetry in the search for New Physics,” *Eur. Phys. J. C* **78** no. 9, (2018) 760, [arXiv:1804.02299 \[hep-ph\]](#).
- [136] B. Hespel, F. Maltoni, and E. Vryonidou, “Higgs and Z boson associated production via gluon fusion in the SM and the 2HDM,” *JHEP* **06** (2015) 065, [arXiv:1503.01656 \[hep-ph\]](#).
- [137] J. Davies, G. Mishima, and M. Steinhauser, “Virtual corrections to $gg \rightarrow ZH$ in the high-energy and large- m_t limits,” [arXiv:2011.12314 \[hep-ph\]](#).
- [138] L. Chen, G. Heinrich, S. P. Jones, M. Kerner, J. Klappert, and J. Schlenk, “ ZH production in gluon fusion: two-loop amplitudes with full top quark mass dependence,” [arXiv:2011.12325 \[hep-ph\]](#).
- [139] R. Bonciani, G. Degrassi, P. P. Giardino, and R. Gröber, “Analytical Method for Next-to-Leading-Order QCD Corrections to Double-Higgs Production,” *Phys. Rev. Lett.* **121** no. 16, (2018) 162003, [arXiv:1806.11564 \[hep-ph\]](#).

-
- [140] L. Alasfar, G. Degrandi, P. P. Giardino, R. Gröber, and M. Vitti, “Virtual corrections to $gg \rightarrow ZH$ via a transverse momentum expansion,” *JHEP* **05** (2021) 168, [arXiv:2103.06225 \[hep-ph\]](#).
- [141] L. D. Landau, “On the angular momentum of a system of two photons,” *Dokl. Akad. Nauk SSSR* **60** no. 2, (1948) 207–209.
- [142] C.-N. Yang, “Selection Rules for the Dematerialization of a Particle Into Two Photons,” *Phys. Rev.* **77** (1950) 242–245.
- [143] G. Passarino and M. J. G. Veltman, “One Loop corrections for e^+e^- annihilation into $\mu^+\mu^-$ in the Weinberg Model,” *Nucl. Phys.* **B160** (1979) 151.
- [144] S. Larin, “The Renormalization of the axial anomaly in dimensional regularization,” *Phys. Lett. B* **303** (1993) 113–118, [arXiv:hep-ph/9302240](#).
- [145] M. Spira, A. Djouadi, D. Graudenz, and P. M. Zerwas, “Higgs boson production at the LHC,” *Nucl. Phys. B* **453** (1995) 17–82, [arXiv:hep-ph/9504378](#).
- [146] U. Aglietti, R. Bonciani, G. Degrandi, and A. Vicini, “Analytic Results for Virtual QCD Corrections to Higgs Production and Decay,” *JHEP* **01** (2007) 021, [arXiv:hep-ph/0611266](#).
- [147] R. Mertig, M. Böhm, and A. Denner, “FEYN CALC: Computer algebraic calculation of Feynman amplitudes,” *Comput. Phys. Commun.* **64** (1991) 345–359.
- [148] V. Shtabovenko, R. Mertig, and F. Orellana, “New Developments in FeynCalc 9.0,” *Comput. Phys. Commun.* **207** (2016) 432–444, [arXiv:1601.01167 \[hep-ph\]](#).
- [149] H. H. Patel, “Package-X 2.0: A Mathematica package for the analytic calculation of one-loop integrals,” *Comput. Phys. Commun.* **218** (2017) 66–70, [arXiv:1612.00009 \[hep-ph\]](#).
- [150] P. Maierhöfer, J. Usovitsch, and P. Uwer, “Kira—A Feynman integral reduction program,” *Comput. Phys. Commun.* **230** (2018) 99–112, [arXiv:1705.05610 \[hep-ph\]](#).
- [151] R. Bonciani, P. Mastrolia, and E. Remiddi, “Master integrals for the two loop QCD virtual corrections to the forward backward asymmetry,” *Nucl. Phys. B* **690** (2004) 138–176, [arXiv:hep-ph/0311145](#).
- [152] S. Borowka and G. Heinrich, “Massive non-planar two-loop four-point integrals with SecDec 2.1,” *Comput. Phys. Commun.* **184** (2013) 2552–2561, [arXiv:1303.1157 \[hep-ph\]](#).

- [153] S. Borowka, G. Heinrich, S. P. Jones, M. Kerner, J. Schlenk, and T. Zirke, “SecDec-3.0: numerical evaluation of multi-scale integrals beyond one loop,” *Comput. Phys. Commun.* **196** (2015) 470–491, [arXiv:1502.06595 \[hep-ph\]](#).
- [154] A. V. Smirnov, “FIRE5: a C++ implementation of Feynman Integral REduction,” *Comput. Phys. Commun.* **189** (2015) 182–191, [arXiv:1408.2372 \[hep-ph\]](#).
- [155] R. N. Lee, “LiteRed 1.4: a powerful tool for reduction of multiloop integrals,” *J. Phys. Conf. Ser.* **523** (2014) 012059, [arXiv:1310.1145 \[hep-ph\]](#).
- [156] A. von Manteuffel and L. Tancredi, “A non-planar two-loop three-point function beyond multiple polylogarithms,” *JHEP* **06** (2017) 127, [arXiv:1701.05905 \[hep-ph\]](#).
- [157] R. Bonciani, G. Degrandi, P. P. Giardino, and R. Gröber, “A Numerical Routine for the Crossed Vertex Diagram with a Massive-Particle Loop,” *Comput. Phys. Commun.* **241** (2019) 122–131, [arXiv:1812.02698 \[hep-ph\]](#).
- [158] L. Naterop, A. Signer, and Y. Ulrich, “handyG —Rapid numerical evaluation of generalised polylogarithms in Fortran,” *Comput. Phys. Commun.* **253** (2020) 107165, [arXiv:1909.01656 \[hep-ph\]](#).
- [159] S. Buehler and C. Duhr, “CHAPLIN - Complex Harmonic Polylogarithms in Fortran,” *Comput. Phys. Commun.* **185** (2014) 2703–2713, [arXiv:1106.5739 \[hep-ph\]](#).
- [160] S. Borowka, G. Heinrich, S. Jahn, S. P. Jones, M. Kerner, J. Schlenk, and T. Zirke, “pySecDec: a toolbox for the numerical evaluation of multi-scale integrals,” *Comput. Phys. Commun.* **222** (2018) 313–326, [arXiv:1703.09692 \[hep-ph\]](#).
- [161] S. Borowka, G. Heinrich, S. Jahn, S. P. Jones, M. Kerner, and J. Schlenk, “A GPU compatible quasi-Monte Carlo integrator interfaced to pySecDec,” *Comput. Phys. Commun.* **240** (2019) 120–137, [arXiv:1811.11720 \[physics.comp-ph\]](#).
- [162] O. Eboli, G. Marques, S. Novaes, and A. Natale, “Twin higgs-boson production,” *Physics Letters B* **197** no. 1, (1987) 269–272.
- [163] E. Glover and J. van der Bij, “Higgs boson pair production via gluon fusion,” *Nuclear Physics B* **309** no. 2, (1988) 282–294.
- [164] D. A. Dicus, C. Kao, and S. S. D. Willenbrock, “Higgs Boson Pair Production From Gluon Fusion,” *Phys. Lett.* **B203** (1988) 457–461.

-
- [165] T. Plehn, M. Spira, and P. M. Zerwas, “Pair production of neutral Higgs particles in gluon-gluon collisions,” *Nucl. Phys.* **B479** (1996) 46–64, [arXiv:hep-ph/9603205 \[hep-ph\]](#). [Erratum: *Nucl. Phys.*B531,655(1998)].
- [166] S. Dawson, S. Dittmaier, and M. Spira, “Neutral Higgs boson pair production at hadron colliders: QCD corrections,” *Phys. Rev.* **D58** (1998) 115012, [arXiv:hep-ph/9805244 \[hep-ph\]](#).
- [167] S. Borowka, N. Greiner, G. Heinrich, S. P. Jones, M. Kerner, J. Schlenk, and T. Zirke, “Full top quark mass dependence in Higgs boson pair production at NLO,” *JHEP* **10** (2016) 107, [arXiv:1608.04798 \[hep-ph\]](#).
- [168] S. Borowka, N. Greiner, G. Heinrich, S. P. Jones, M. Kerner, J. Schlenk, U. Schubert, and T. Zirke, “Higgs Boson Pair Production in Gluon Fusion at Next-to-Leading Order with Full Top-Quark Mass Dependence,” *Phys. Rev. Lett.* **117** no. 1, (2016) 012001, [arXiv:1604.06447 \[hep-ph\]](#). [Erratum: *Phys. Rev. Lett.*117,no.7,079901(2016)].
- [169] J. Baglio, F. Campanario, S. Glaus, M. Mühlleitner, M. Spira, and J. Streicher, “Gluon fusion into Higgs pairs at NLO QCD and the top mass scheme,” *Eur. Phys. J.* **C79** no. 6, (2019) 459, [arXiv:1811.05692 \[hep-ph\]](#).
- [170] G. Heinrich, S. P. Jones, M. Kerner, G. Luisoni, and L. Scyboz, “Probing the trilinear Higgs boson coupling in di-Higgs production at NLO QCD including parton shower effects,” *JHEP* **06** (2019) 066, [arXiv:1903.08137 \[hep-ph\]](#).
- [171] J. Davies, R. Gröber, A. Maier, T. Rauh, and M. Steinhauser, “Top quark mass dependence of the Higgs boson-gluon form factor at three loops,” *Phys. Rev.* **D100** no. 3, (2019) 034017, [arXiv:1906.00982 \[hep-ph\]](#).
- [172] M. Grazzini, G. Heinrich, S. Jones, S. Kallweit, M. Kerner, J. M. Lindert, and J. Mazzitelli, “Higgs boson pair production at NNLO with top quark mass effects,” *JHEP* **05** (2018) 059, [arXiv:1803.02463 \[hep-ph\]](#).
- [173] NNPDF Collaboration, R. D. Ball *et al.*, “Parton distributions from high-precision collider data,” *Eur. Phys. J.* **C77** no. 10, (2017) 663, [arXiv:1706.00428 \[hep-ph\]](#).
- [174] A. Buckley, J. Ferrando, S. Lloyd, K. Nordström, B. Page, M. Rüfenacht, M. Schönherr, and G. Watt, “LHAPDF6: parton density access in the LHC precision era,” *Eur. Phys. J.* **C75** (2015) 132, [arXiv:1412.7420 \[hep-ph\]](#).
- [175] A. Denner, S. Dittmaier, and L. Hofer, “COLLIER - A fortran-library for one-loop integrals,” *PoS* **LL2014** (2014) 071, [arXiv:1407.0087 \[hep-ph\]](#).

- [176] S. Dittmaier *et al.*, “Handbook of LHC Higgs Cross Sections: 2. Differential Distributions,” [arXiv:1201.3084 \[hep-ph\]](#).
- [177] **LHC Higgs Cross Section Working Group** Collaboration, D. de Florian *et al.*, “Handbook of LHC Higgs Cross Sections: 4. Deciphering the Nature of the Higgs Sector,” [arXiv:1610.07922 \[hep-ph\]](#).
- [178] A. D. Martin, W. J. Stirling, R. S. Thorne, and G. Watt, “Uncertainties on $\alpha(S)$ in global PDF analyses and implications for predicted hadronic cross sections,” *Eur. Phys. J. C* **64** (2009) 653–680, [arXiv:0905.3531 \[hep-ph\]](#).
- [179] F. Demartin, S. Forte, E. Mariani, J. Rojo, and A. Vicini, “The impact of PDF and alphas uncertainties on Higgs Production in gluon fusion at hadron colliders,” *Phys. Rev. D* **82** (2010) 014002, [arXiv:1004.0962 \[hep-ph\]](#).
- [180] J. Baglio, A. Djouadi, R. Gröber, M. M. Mühlleitner, J. Quevillon, and M. Spira, “The measurement of the Higgs self-coupling at the LHC: theoretical status,” *JHEP* **04** (2013) 151, [arXiv:1212.5581 \[hep-ph\]](#).
- [181] I. Brivio, F. Goertz, and G. Isidori, “Probing the Charm Quark Yukawa Coupling in Higgs+Charm Production,” *Phys. Rev. Lett.* **115** no. 21, (2015) 211801, [arXiv:1507.02916 \[hep-ph\]](#).
- [182] Y. Soreq, H. X. Zhu, and J. Zupan, “Light quark Yukawa couplings from Higgs kinematics,” *JHEP* **12** (2016) 045, [arXiv:1606.09621 \[hep-ph\]](#).
- [183] F. Bishara, U. Haisch, P. F. Monni, and E. Re, “Constraining Light-Quark Yukawa Couplings from Higgs Distributions,” *Phys. Rev. Lett.* **118** no. 12, (2017) 121801, [arXiv:1606.09253 \[hep-ph\]](#).
- [184] G. Bonner and H. E. Logan, “Constraining the Higgs couplings to up and down quarks using production kinematics at the CERN Large Hadron Collider,” [arXiv:1608.04376 \[hep-ph\]](#).
- [185] **CMS** Collaboration, “Constraints on the Higgs boson self-coupling from $t\bar{t}H+tH$, H to gamma gamma differential measurements at the HL-LHC,” Tech. Rep. CMS-PAS-FTR-18-020, 2018.
- [186] G. Perez, Y. Soreq, E. Stamou, and K. Tobioka, “Prospects for measuring the Higgs boson coupling to light quarks,” *Phys. Rev. D* **93** no. 1, (2016) 013001, [arXiv:1505.06689 \[hep-ph\]](#).
- [187] **ATLAS** Collaboration, “Direct constraint on the Higgs-charm coupling from a search for Higgs boson decays to charm quarks with the ATLAS detector,”

-
- [188] G. T. Bodwin, F. Petriello, S. Stoynev, and M. Velasco, “Higgs boson decays to quarkonia and the $H\bar{c}c$ coupling,” *Phys. Rev.* **D88** no. 5, (2013) 053003, [arXiv:1306.5770 \[hep-ph\]](#).
 - [189] A. L. Kagan, G. Perez, F. Petriello, Y. Soreq, S. Stoynev, and J. Zupan, “Exclusive Window onto Higgs Yukawa Couplings,” *Phys. Rev. Lett.* **114** no. 10, (2015) 101802, [arXiv:1406.1722 \[hep-ph\]](#).
 - [190] M. König and M. Neubert, “Exclusive Radiative Higgs Decays as Probes of Light-Quark Yukawa Couplings,” *JHEP* **08** (2015) 012, [arXiv:1505.03870 \[hep-ph\]](#).
 - [191] **CMS** Collaboration, A. M. Sirunyan *et al.*, “Search for rare decays of Z and Higgs bosons to J/ψ and a photon in proton-proton collisions at $\sqrt{s} = 13$ TeV,” *Eur. Phys. J. C* **79** no. 2, (2019) 94, [arXiv:1810.10056 \[hep-ex\]](#).
 - [192] F. Yu, “Light Quark Yukawa Couplings and the $W^\pm h$ Charge Asymmetry,” *Nucl. Part. Phys. Proc.* **285-286** (2017) 123–125.
 - [193] J. A. Aguilar-Saavedra, J. M. Cano, and J. M. No, “More light on Higgs flavor at the LHC: Higgs boson couplings to light quarks through $h + \gamma$ production,” *Phys. Rev. D* **103** no. 9, (2021) 095023, [arXiv:2008.12538 \[hep-ph\]](#).
 - [194] A. Falkowski, S. Ganguly, P. Gras, J. M. No, K. Tobioka, N. Vignaroli, and T. You, “Light quark Yukawas in triboson final states,” *JHEP* **04** (2021) 023, [arXiv:2011.09551 \[hep-ph\]](#).
 - [195] **ATLAS** Collaboration, A. Sciandra, “Measurement of Triboson Production and aQGCs with the ATLAS detector,”
 - [196] **CMS** Collaboration, “Observation of heavy triboson production in leptonic final states in proton-proton collisions at $\sqrt{s} = 13$ TeV,”
 - [197] T. Binoth, S. Karg, N. Kauer, and R. Ruckl, “Multi-Higgs boson production in the Standard Model and beyond,” *Phys. Rev.* **D74** (2006) 113008, [arXiv:hep-ph/0608057 \[hep-ph\]](#).
 - [198] R. Contino, M. Ghezzi, M. Moretti, G. Panico, F. Piccinini, and A. Wulzer, “Anomalous Couplings in Double Higgs Production,” *JHEP* **08** (2012) 154, [arXiv:1205.5444 \[hep-ph\]](#).
 - [199] L. Alasfar, R. Corral Lopez, and R. Gröber, “Probing Higgs couplings to light quarks via Higgs pair production,” *JHEP* **11** (2019) 088, [arXiv:1909.05279 \[hep-ph\]](#).

- [200] S. Bar-Shalom and A. Soni, “Universally enhanced light-quarks Yukawa couplings paradigm,” *Phys. Rev.* **D98** no. 5, (2018) 055001, [arXiv:1804.02400 \[hep-ph\]](#).
- [201] M. Bauer, M. Carena, and A. Carmona, “Higgs Pair Production as a Signal of Enhanced Yukawa Couplings,” *Phys. Rev. Lett.* **121** no. 2, (2018) 021801, [arXiv:1801.00363 \[hep-ph\]](#).
- [202] D. Egana-Ugrinovic, S. Homiller, and P. Meade, “Multi-Higgs Production Probes Higgs Flavor,” *Phys. Rev. D* **103** (2021) 115005, [arXiv:2101.04119 \[hep-ph\]](#).
- [203] A. Papaefstathiou and K. Sakurai, “Triple Higgs boson production at a 100 TeV proton-proton collider,” *JHEP* **02** (Aug, 2015) 006. 10 p, [arXiv:1508.06524](#). <https://cds.cern.ch/record/2047255>. Corrected version of Figure 6.
- [204] C. Delaunay, R. Ozeri, G. Perez, and Y. Soreq, “Probing Atomic Higgs-like Forces at the Precision Frontier,” *Phys. Rev.* **D96** no. 9, (2017) 093001, [arXiv:1601.05087 \[hep-ph\]](#).

List of publications

1. **L. Alasfar**, G. Degrassi, P. P. Giardino, R. Gröber and M. Vitti
Virtual corrections to $gg \rightarrow ZH$ via a transverse momentum expansion
JHEP **05** (2021), 168
arXiv:2103.06225 [hep-ph].
2. **L. Alasfar**, A. Azatov, J. de Blas, A. Paul and M. Valli
 B anomalies under the lens of electroweak precision
JHEP **12** (2020), 016
arXiv:2007.04400 [hep-ph].
3. **L. Alasfar**, R. Corral Lopez and R. Gröber
Probing Higgs couplings to light quarks via Higgs pair production
JHEP **11** (2019), 088
arXiv:1909.05279 [hep-ph].